CHEMICAL AND MECHANICAL ANALYSIS OF BORON-RICH BORON CARBIDE PROCESSED VIA SPARK PLASMA SINTERING

by

TYLER LEE MUNHOLLON

A dissertation submitted to the

Graduate School-New Brunswick

Rutgers, The State University of New Jersey

In partial fulfillment of the requirements

For the degree of

Doctor of Philosophy

Graduate Program in Materials Science and Engineering

Written under the direction of

Dr. Richard A. Haber

And approved by

_____

_____

_____

_____

_____

New Brunswick, New Jersey

October, 2016

ABSTRACT OF THE DISSERTATION

Chemical and Mechanical Analysis of Boron-Rich Boron Carbide Processed via Spark Plasma Sintering

By TYLER LEE MUNHOLLON

Dissertation Director:

Richard A. Haber

Boron carbide is a material of choice for many industrial and specialty applications due to the exceptional properties it exhibits such as high hardness, chemical inertness, low specific gravity, high neutron cross section and more. The combination of high hardness and low specific gravity makes it especially attractive for high pressure/high strain rate applications. However, boron carbide exhibits anomalous behavior when high pressures are applied. Impact pressures over the Hugoniot elastic limit result in catastrophic failure of the material. This failure has been linked to amorphization in cleavage planes and loss of shear strength. Atomistic modeling has suggested boron-rich boron carbide ($B_{13}C_2$) may be a better performing material than the commonly used B_4C due to the elimination of amorphization and an increase in shear strength. Therefore, a clear experimental understanding of the factors that lead to the degradation of mechanical properties as well as the effects of chemistry changes in boron carbide is needed. For this reason, the goal of

this thesis was to produce high purity boron carbide with varying stoichiometries for chemical and mechanical property characterization.

Utilizing rapid carbothermal reduction and pressure assisted sintering, dense boron carbides with varying stoichiometries were produced. Microstructural characteristics such as impurity inclusions, porosity and grain size were controlled. The chemistry and common static mechanical properties that are of importance to superhard materials including elastic moduli, hardness and fracture toughness of the resulting boron-rich boron carbides were characterized.

A series of six boron carbide samples were processed with varying amounts of amorphous boron (up to 45 wt. % amorphous boron). Samples with greater than 40 wt.% boron additions were shown to exhibit abnormal sintering behavior, making it difficult to characterize these samples. Near theoretical densities were achieved in samples with less than 40 wt. % amorphous boron additions. X-ray diffraction analysis revealed the samples to be phase pure and boron-rich. Carbon content was determined to be at or near expected values with exception of samples with greater than 40 wt. % amorphous boron additions. Raman microspectroscopy further confirmed the changes in chemistry as well as revealed the chemical homogeneity of the samples. Microstructural analysis carried out using both optical and electron imaging showed clean and consistent microstructures.

The changes in the chemistry of the boron carbide samples has been shown to significantly affect the static mechanical properties. Ultrasonic wave speed measurements were used to calculate the elastic moduli which showed a clear decrease in the Young's and shear moduli with a slight increase in bulk modulus. Berkovich nano-indentation revealed a similar trend, as the hardness and fracture toughness of the material decreased

with decreasing carbon content. Amorphization within 1 kg Knoop indents was shown to diminish in intensity and extent as carbon content decreased, signifying a mechanism for amorphization mitigation.

Acknowledgements

Many people have been involved in one way or another throughout my time at Rutgers. One person, in particular, put in a lot of time and effort to help me progress to where I am today, my advisor, Dr. Haber. It seems like just yesterday that I met you on my visit to campus. Your excitement for the research your group was conducting really drew me in. The stories you told at dinner sealed the deal, I wanted to come to Rutgers. Although there has been many ups and downs throughout my time here, I have never once doubted my decision. You have taught me many things whether it be about research or life. I can't thank you enough.

My second thanks goes to my dissertation committee, Prof. Matthewson, Prof. Lehman, Dr. Rafaniello and Dr. Domnich. While I may not have been the best and keeping my committee informed, they were always willing to help when needed. The wealth of knowledge that you all imparted on me has helped me get to the point that I am at today. Your unwavering dedication to helping me throughout this process will not be forgotten.

Thanks to all the professors and MSE staff that have helped me along the way. An especially big thanks to Dr. Klein, your guidance as Graduate Director has helped alleviate a lot of headaches along the way. I think most of the graduate students will agree, it is not always easy navigating the Rutgers system but you have always been there to help and that is much appreciated.

Thank you to the unsung hero of the Haber group, Michelle Sole. I met you on my first visit to Rutgers and you kicked me out of the conference room because it was reserved for something else. Not the best first impression. Little did I know then that you would

becoming such a vital part of my time here. Whether it was ordering supplies, getting reimbursements or just talking about life you have always been there. I am grateful to have been able get to work with you for the last four years. Thanks for everything.

The Haber group. You have always made it interesting, whether for the good or bad, but I wouldn't want it any other way. I have had a great time sharing these last four years with you guys and you will be truly missed. To Vince, you're not that good at fantasy sports we all just really stink. On a serious note though, I owe you a big thanks for the help you have provided through the years. You have always been the go to guy when I had the questions about research or was stuck on a Sporcle quiz. To Anthony, you have a way always making things interesting and often times fun, which was needed. I cherish the friendship that we have formed and I will miss the good ol' times we have had at conferences. To the rest of you thanks for everything and good luck with your future endeavors.

To my friends, thanks for all the love and support you have given throughout this process, it has made things much easier. Many great memories have been made and I hope for many more.

Last, but certainly not least, thanks to my wonderful family for the unwavering support. It was scary moving to New Jersey all by myself and leaving my family nearly a 1000 miles away. You guys have made it easy on me though by keeping me in the loop on what is going on back home and helping me watch Mason, Cooper and Owen grow up. I would have loved to have been there to see it in person but hopefully all this work I have

put in will serve as an example of what they can accomplish in their lives. I love you all, thanks for everything.

Table of Contents

List of Tables

List of Figures

1. Introduction

Boron carbide is a covalently bonded, superhard (37 GPa)[1] ceramic with many attractive properties including low density (2.52g/cm^3)[2], high elastic modulus (480 GPa)[1], high melting point (2450°C)[3], chemical inertness and high neutron absorption cross section (600 barns)[3]. The exceptional properties of boron carbide lead to many uses including but not limited to abrasives, armor ceramics and neutron absorbers for the nuclear industry. However, boron carbide exhibits anomalous behavior when subjected to high pressures.

Boron carbide performs well when undergoing a low-pressure ballistic event but when subjected to high pressure/high strain rate events, boron carbide undergoes a loss of shear strength which results in catastrophic failure. Analyzing boron carbide fragments from the ballistic experiments has shown that boron carbide undergoes amorphization at the cleavage planes.[4] This loss of shear strength and amorphization occurs at pressures greater than the Hugoniot elastic limit of the material (~20 GPa).[5] Amorphization has been suggested as the mechanism that causes catastrophic failure. Understanding and eliminating amorphization and the loss of shear strength has been the focus of much research in recent years.

To engineer a better boron carbide, it is pertinent to understand the mechanisms that control the mechanical properties and failure. The performance of dense boron carbide is highly dependent upon both the stoichiometry and purity of the starting powder. Carbothermal reduction, which is used in industry to synthesize boron carbide, produces powders that contain large amounts of impurities ranging from metallic impurities from post processing to free carbon left from the synthesis reaction. Rafaniello[6] was able to

produce highly pure boron carbide that required no post processing and had little to no detectable free carbon using rapid carbothermal reduction. Toksoy[7], using rapid carbothermal reduction, was able to show that the elimination of impurities within the boron carbide powders lead to higher hardness and better microstructures as compared to commercial boron carbide.

Commercially available boron carbide is synthesized in a way that the carbon concentration is typically greater than 18 at.% C. Due to the limited stoichiometries of commercially available boron carbides, understanding of the stoichiometric effects on the properties of bulk boron carbide is lacking. Some results have been produced using chemical vapor deposition[8] and other laboratory methods.[9, 10, 11, 12] However, the results are limited and bulk boron-rich boron carbide has proven difficult to synthesize.[12] Eliminating factors such as impurities, porosity and grain growth while varying the stoichiometry will allow for a more complete understanding of the effect stoichiometry has on the properties of boron carbide.

The objective of this thesis was to produce bulk, dense boron-rich boron carbide. Utilizing rapid carbothermal reduction and pressure assisted sintering, dense boron carbides with varying stoichiometries were produced. Microstructural characteristics such as impurity inclusions, porosity, and grain size were controlled. The chemistry and common static mechanical properties that are of importance to superhard materials, including elastic moduli, hardness and fracture toughness, of the resulting boron-rich boron carbides were characterized using several techniques and compared to literature.

2. Background

2.1 Structure

The structure of boron carbide consists of a rhombohedral unit cell that contains fifteen atoms with trigonal symmetry ($R\bar{3}m$ space group). Twelve atom icosahedra are located on the corners of the rhombohedral unit cell with the three atom chain along the body diagonal ([111] rhombohedral direction) connecting two icosahedra (Figure 1). The twelve atom icosahedra contain two distinct sites, polar and equatorial. Polar sites correspond to the three atoms at the top and bottom of the icosahedra (six total atoms) that are involved with the linking of icosahedra. Equatorials sites correspond to the six atoms that are involved in the bonding to the three atom chain.[13] Figure 2 shows the twelve atom icosahedra with the polar and equatorial sites indicated. The unit cell can also be described using a hexagonal unit cell where the [0001] direction correlates to the [111] direction in the rhombohedral unit cell. Using the hexagonal unit cell the lattice can be described using two unique parameters, *a* and *c*.[14] While the unit cell of boron carbide is well known, the exact site occupancy of each atomic position is not known. This arises from the similarities between the electronic and nuclear absorption cross sections of boron and carbon.[14] Two phases of boron carbide are discussed throughout literature, B_4C (carbon-rich) and $B_{13}C_2$ (boron-rich). The atomic configuration of B_4C was assumed to be made up of B_{12} icosahedra with a three carbon chain. However, theoretical calculations have shown that there may be multiple different configurations present at once. The possible structural units that are B_{12}, $B_{11}C$, $B_{10}C_2$ and B_9C_3 icosahedra and CCC, CBC, CBB and BBB chains. Out of these structural units, Fanchini[15] showed the most common to be B_{12} and $B_{11}C$ icosahedra and CCC, CBC and CBB chains. Figure 3 shows the most common

configurations. Those being $B_{11}C_p$(CBC), B_{12}(CCC) and $B_{11}C_e$(CBC). Further theoretical modeling and free energy minimization showed that $B_{11}C_p$(CBC) is the preferred B_4C atomic configuration and B_{12}(CBC) is the preferred $B_{13}C_2$ atomic configuration.[13] The mixture of different possible atomic configurations within boron carbide makes an empirical understanding very difficult. However, some experimental work has been able to gain insight into the site occupancy of boron carbide specifically, Raman spectroscopy.

Raman microspectroscopy is a widely used technique for understanding the bonding and atomic structure of materials. Therefore, many reports have been published on the Raman response of boron carbide. Nevertheless, there is still much disagreement about the assignment of Raman bands to structural units. The unique Raman bands for boron carbide range from 200 to 1200 cm^{-1}.[16] Within this range a series of different bands are present and changes in size and location of bands vary with stoichiometry. The peaks that are seen in the range of 600 to 1200 cm^{-1} are typically associated with the 12 atom icosahedra.[16] While the band centered at 1088 cm^{-1} has been assigned to the breathing mode of the icosahedra. On the other hand, the bands below 600 cm^{-1} are highly debated.[17] Tallant and Aselage[16] reported that these bands are associated with the chain structure. They determined that the 480 cm^{-1} and 535 cm^{-1} belong to the CBC chain stretching mode and that the intensity of these bands diminishes with a decrease in carbon content. The decrease in intensity would point to a change from CBC to CBB chains. Vast *et al*.[18] using computational methods attributed the Raman band at 535 cm^{-1} to the icosahedron liberation mode. In the same work, they concluded that the atomic structure of boron carbide is made up of $B_{11}C$ icosahedra with CBC chains which have been previously stated as the accepted structure of stoichiometric boron carbide. The appearance of two bands 270 cm^{-1} and 320

cm^{-1} were also reported by Tallant and Aselage[16]. Similar work done by Werheit[19] attributed these bands to the rotations of the CBC and CBB chains. These results from Raman spectroscopy provide some insight into the structure of boron carbide.

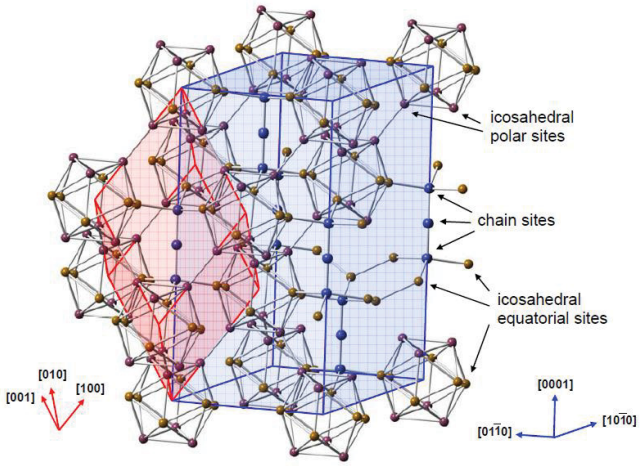

Figure 1. The unit cell of boron carbide. The red cell indicates the rhombohedral configuration. The blue cell indicates the hexagonal unit cell.[14]

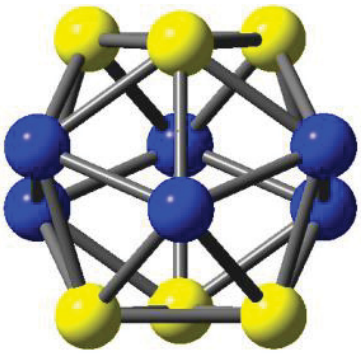

Figure 2. The 12 atom icosahedra. Yellow atoms indicate polar sites. Blue atoms indicate equatorial sites.[15]

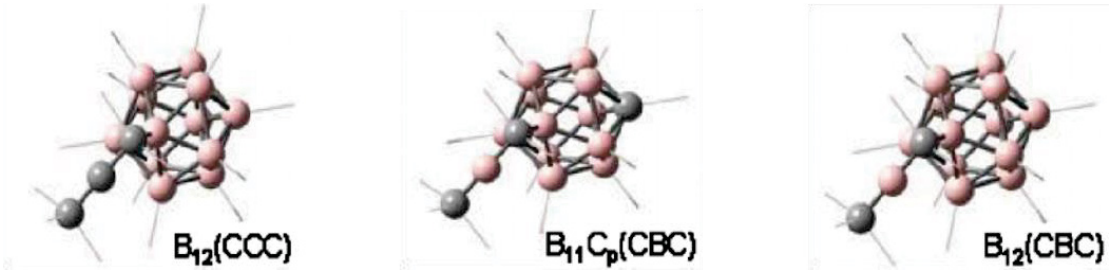

Figure 3. Common boron carbide atomic configurations.[15]

The changes in the atomic configuration that have been discussed above affect the unit cell volume due to the difference in the atomic radii for carbon and boron. The change in the unit cell volume directly correlates to a change in the *a* and *c* hexagonal lattice parameters. Aselage *et al.*[20] have shown that it is possible to use the change in the lattice parameter to determine carbon concentration in boron carbide. Figure 4 shows the plots of reported lattice parameter versus carbon concentration.

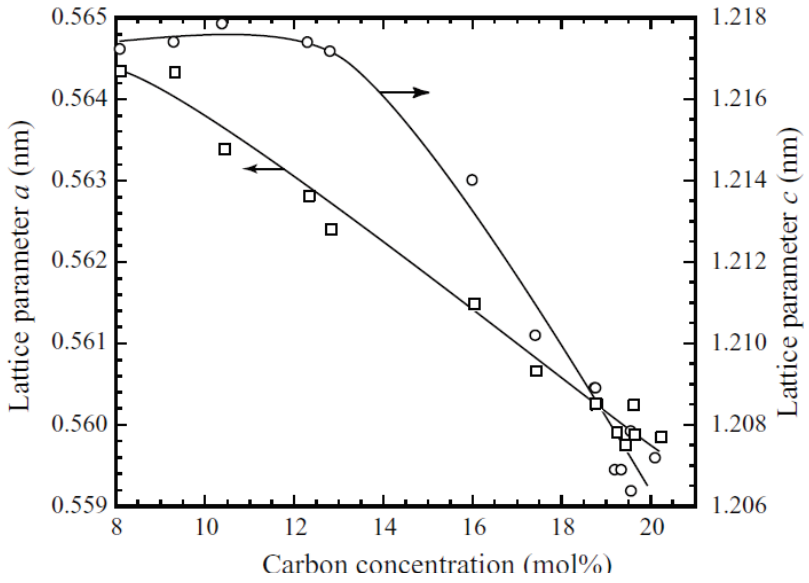

Figure 4. Lattice parameter vs. carbon concentration as determined by Aselage *et al*.[20]

The boron carbide phase diagram is another controversial topic. Many changes have been made since the first boron carbide phase diagram was developed by Ridgway[21]. There is agreement, however, that there is a large solid solubility region where the stable boron carbide phase exists. The exact limits of the solid solubility range have been debated over the years. Most agree, though, that the boron-rich limit is approximately 8 at. %. Values for the carbon-rich limit have been reported as high as 24.3 at. % C by Beauvy and as low 18.8 at. % by Schewtz.[22, 23] Three of the most common phase diagrams used in boron carbide literature are shown in Figure 5. The phase diagram of Ekbom and Amundin[24] has the carbon rich limit at 20at.% C. The phase diagram by Beauvy[22] shows the carbon rich limit to be 24.3 at.%. The third phase diagram by Schwetz[23] shows carbon-rich limit of 19.2 at.%.

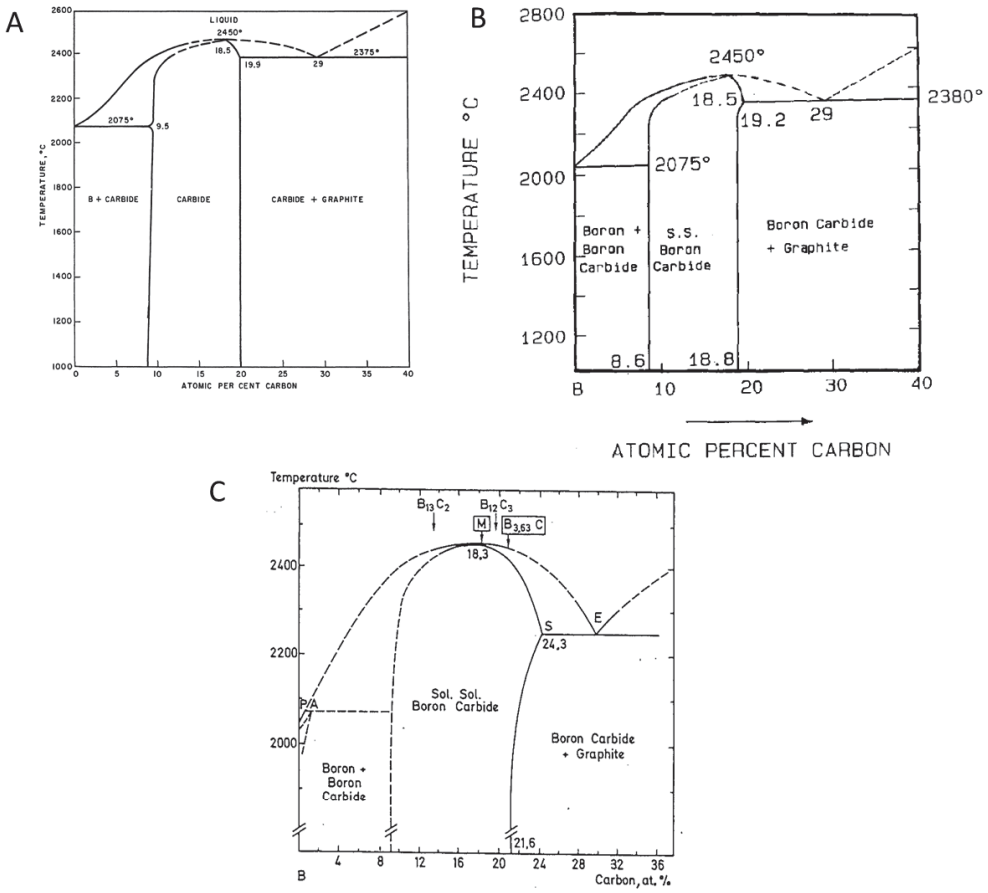

Figure 5. Boron carbide phase diagrams from A) Ekbom and Amundin[24], B) Schwetz[23], C) Beauvy[22].

2.2 Density

The density of boron carbide varies linearly with the carbon content within the solid solubility range of 8 at. % C to 20 at. % carbon. Equation 1 shows the linear relationship between the density and the carbon content:

$$d\left(\frac{g}{cm^3}\right) = 2.422 + 0.0048[C] \quad (1)$$

where [C] is the carbon content in atomic percent.[25] B_4C (20 at. % C) has a density of 2.52 g/cm^3 whereas $B_{13}C_2$ has a density of 2.49 g/cm^3.

With a density of 2.52 g/cm^3 or less, boron carbide is one of the lightest armor ceramics in existence. Table 1 lists some other common armor materials and their corresponding densities. The low density of boron carbide makes it a very desirable armor material.

Table 1. Density of common armor materials.[7]

Material	Density (g/cm^3)
Boron Carbide	2.5
WC-Co 94/6	14.9
Silicon Carbide	3.2
Aluminum Nitride	3.3
Aluminum Oxide	3.9
$MgAl_2O_4$ Spinel	3.6
AlON	3.7
Steel	7.8
Titanium Carbide	4.9

2.3 Synthesis of Boron Carbide

The first known synthesis of boron carbide dates back to the mid-nineteenth century. The synthesized boron carbide was a byproduct of the synthesis of metal borides and contained large amounts of impurities. Increased purity was reported by Ridgeway[26] in 1933. Using carbothermal reduction to synthesize boron carbide powder purity greater than 90% was achieved. Continued work throughout the 1900's and 2000's have resulted in a multitude of synthesis methods with increased purity and improved morphologies.[3] This section briefly discusses a few of the most common methods used in industry and research.

2.3.1 Carbothermal Reduction

Carbothermal reduction is widely used in industry to synthesize boron carbide due to the use of inexpensive raw materials and scalability. Carbothermal reduction uses carbon to reduce a metal oxide to its elemental form. In the case of boron carbide, the metal oxide is boron oxide.

In industry, boric acid and petroleum coke are the raw materials of choice. The carbothermal reduction reaction goes as follows:

$$4H_3BO_3 + 7C \rightarrow B_4C + 6CO + 6H_2O \quad (2)$$

This reaction can be broken down into three intermediary reactions as follows:

$$4H_3BO_3 \rightarrow 2B_2O_3 + 6H_2O \quad (3)$$

$$2B_2O_3 + 6C \rightarrow 4B + 6CO \quad (4)$$

$$4B + C \rightarrow B_4C \quad (5)$$

Reaction equation 2 is the dehydration of the boric acid to form boron oxide which is subsequently reduced in reaction equation 3. After the reduction in reaction equation 3, four moles of boron are left to react with petroleum coke. The overall carbothermal reduction reaction for boron carbide (reaction equation 1) is highly endothermic, needing in excess of 1635 kJ/mol of boron carbide to proceed.[27] Such high energy needs requires temperatures in excess of 1500°C to proceed, with temperatures of 2000°C and higher often being employed. The heating rates, however, are relatively slow (~100°C/s). The slow heating rates favor a nucleation and growth mechanism since the reaction is most likely occurring between the molten B_2O_3 and the solid petroleum coke. The liquid-solid reaction limits nucleation and therefore, growth dominates leading to large boron carbide grains.[28]

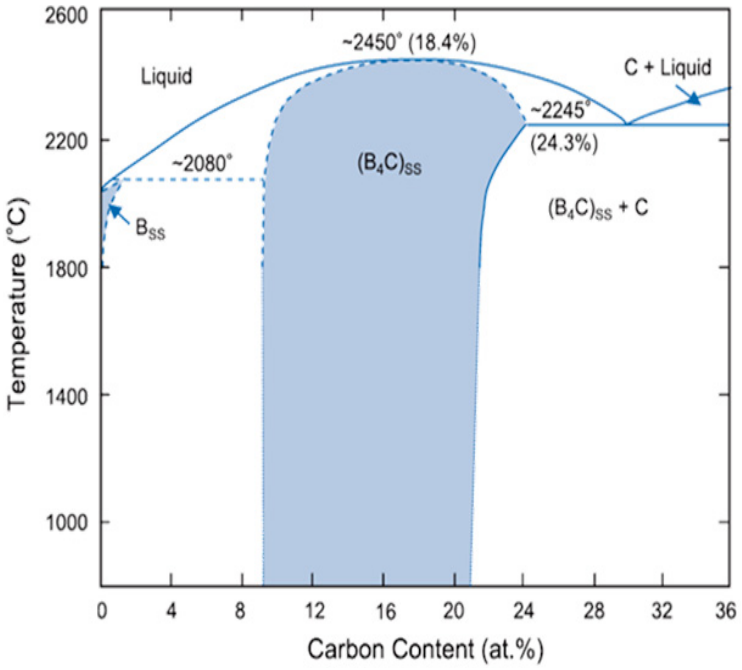

Figure 6. Boron-carbon phase diagram[22].

Many different forms of the boron-carbon phase diagram exist, each with their own solid solubility range and stable phase. For the sake of this work, the phase diagram by Beauvy[22] was used. The thermodynamics suggests that the stoichiometric B_4C is the stable reaction product up to the melting temperature of boron carbide, which is in agreement with the phase diagram by Beauvy.[28] For this reason, most commercial materials are near to 20 at.% carbon. Commercial boron carbides also typically contain small amounts of impurities, the main being free carbon and metallic impurities from post processing. Some amounts of boron oxide are left as well but can be easily washed out.

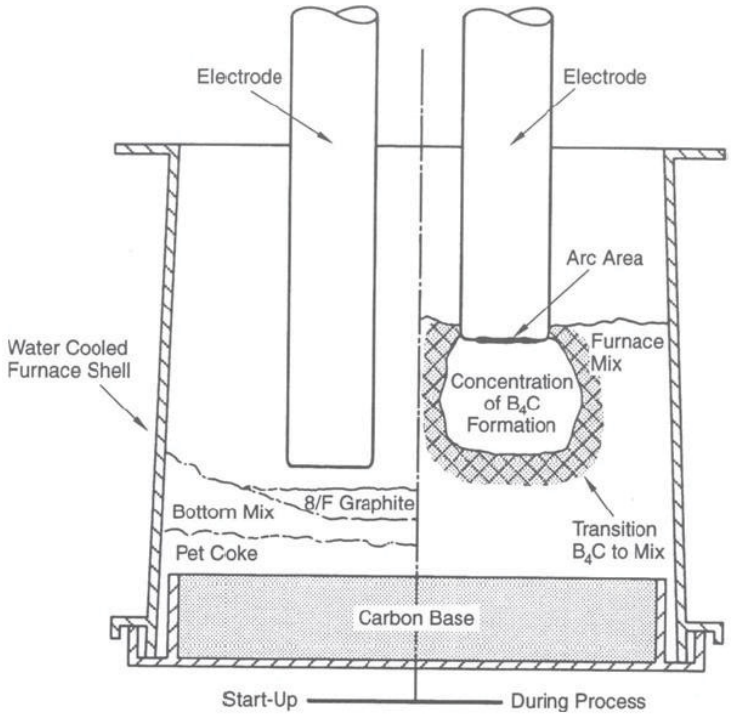

Figure 7. Electric arc furnace set up for synthesizing boron carbide.[29]

Industrial carbothermal reduction reactions are carried out in large electric arc furnaces. The setup of the furnace can be seen in Figure 7. A layer of petroleum coke is placed at the bottom of the furnace with a small layer of the boric acid/petroleum coke mixture on top. Once the mix is in place, the graphite electrodes are put in place and a current is applied. The electrodes are slowly raised while more boric acid/petroleum coke mixture is added. The area directly under the arc reacts to form boron carbide. Due to the nature of the arc furnace, very high temperatures can be achieved. These high temperatures can lead to a large loss of boron oxide as it evaporates to form gaseous boron suboxides. Therefore, some partially reacted material is mixed in with the boric acid/petroleum coke mix to replenish the boron oxide that is lost and help reduce the energy needed for the reaction.[29] A drawback to the electric arc furnace is that while the electric arc creates locally high temperatures a thermal gradient is formed throughout the rest of the material

leading to an incomplete reaction the farther away from the electrode the mix is. The resulting ingot contains reacted and partially reacted boron carbide along with unreacted boron oxide and carbon (Figure 8). An operator has to manually sort the reacted from the unreacted material. The unreacted material is used again in a subsequent run. The large ingots of boron carbide have to be significantly crushed which results in the introduction of metallic impurities (Figure 9). The impurities are often very difficult or impossible to remove resulting in degradation in strength of the resulting dense body.

Figure 8. An ingot of boron carbide synthesized using the electric arc furnace. Circles indicate regions of reacted boron carbide (Courtesy of Washington Mills, Niagara Falls, NY).

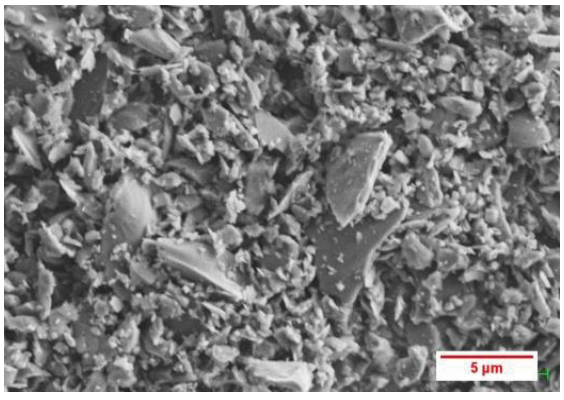

Figure 9. Commercially synthesized powders shown after crushing.[7]

2.3.2 Rapid Carbothermal Reduction

The rapid carbothermal reduction reaction for synthesis of boron carbide was patented in 1989 by Rafaniello *et al*.[6] from Dow Chemical. Unlike the electric arc furnace process which uses very slow heating rates, rapid carbothermal reduction employs heating rates in excess of 10^5 °C/sec. This variation in heating rate has been shown to drastically affect the reaction kinetics. While carbothermal reduction usually takes place at extremely high temperatures (>>B_2O_3 M.P.), the heating rates are sufficiently low such that the reaction takes place by nucleation and growth. By increasing the heating rates and keeping the reaction temperature in excess of the melting point of B_2O_3, the reaction has been suggested to occur by precursor particle rupture and subsequent gas-solid or gas-gas reaction. This allows the reaction to take place in a matter of seconds as opposed to the hours needed for industrial synthesis. The following gas-solid reaction equation has been suggested by Weimer[28]:

$$C(s) + B_2O_3(l) \rightarrow B_2O_2\ (g) + CO\ (g) \tag{6}$$

$$5C(s) + 2B_2O_2(g) \rightarrow B_4C(s) + 4CO(g) \tag{7}$$

Due to the particle rupture and short reaction times, particle nucleation happens readily while grain growth is limited. Therefore, boron carbide that is synthesized using rapid carbothermal reduction is equiaxed and submicron to a micron in size. Another major advantage of rapid carbothermal reduction is that the direct formation of powders, as opposed to ingots, eliminates the need for post-processing which in turn eliminates the introduction of metallic impurities.

The carbon source for rapid carbothermal reduction varies from activated carbons used in printer inks to sugars and cornstarch that are readily available in a supermarket. Boric acid, however, is consistently used as the boron source for rapid carbothermal reduction.

Reactors used for rapid carbothermal reduction of boron carbide vary in design from group to group (an example can be seen in Figure 10) but the overall process is similar. An intimate boron oxide/carbon mixture is used as the precursor material. The precursor is crushed to uniform size and fed through a cooled transport tube that prevents the boron oxide from melting until it reaches the reaction zone. The precursor exits the cooled transport tube and enters that reaction zone which is at a temperature in excess of 1800°C. This abrupt change in temperature causes the high heating rate discussed above. The powder begins to react immediately. Each individual particle can be assumed to be isothermal and is allowed to react with the same amount of time, leading to uniform morphology and chemistry. The powder falls to the bottom of the reaction zone and is either collected into a crucible or continues into a cooled collection chamber. Finished powder often contains some amounts of residual boron oxide, due to the excess used to ensure complete reaction, which can be easily washed from the powder using either methanol or an HCl solution.[30]

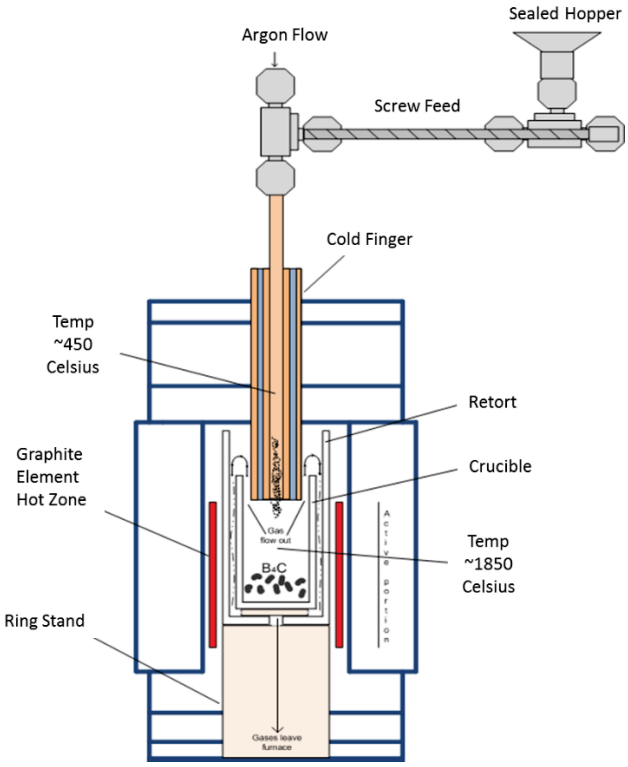

Figure 10. Rapid carbothermal reduction furnace schematic.[31]

Work done by Miller and Toksoy[31], using a rapid carbothermal reduction reactor at Rutgers University, showed that it is possible to synthesize equiaxed, sub-micron boron carbide with no detectable free carbon. Unreacted free carbon left from synthesis is very difficult to remove from the powder, therefore it is highly important to limit the amount and ultimately eliminate the free carbon that is left from the synthesis process. This free carbon that is left in the powder turns to carbon inclusions within the densified boron carbide which adversely affects the mechanical properties.

It was also found that the powder size and morphology is controlled by the choice of carbon raw material. Figure 11 shows two boron carbide powder synthesized using rapid carbothermal reduction. The powder on the left used carbon lampblack as a reactant

whereas the powder on the left used Vulcan XC-72 (Cabot Industries). Both powders were shown to be phase pure with a normal particle size distribution. However, the powder made with carbon lampblack was slightly larger and had a faceted morphology. The powder made with Vulcan XC-72, on the other hand, was very fine with a more spherical morphology. This controlled manipulation of the powder characteristics becomes of great importance when trying to design an improved microstructure.

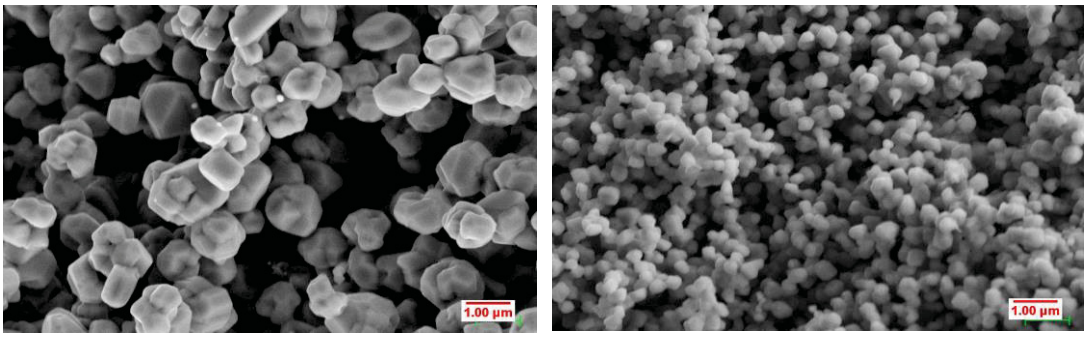

Figure 11. Rapid carbothermally reduced boron carbide powders, A) carbon lamp black carbon source and B) Vulcan XC-72 (Cabot Industries) carbon source.[7]

2.3.3 Other Methods

A variety of other synthesis methods have been reported in the literature. These include magnesiothermic reduction, synthesis from elements, vapor phase synthesis, synthesis from polymers and more. The magnesiothermic reduction is a method that has been used as an alternative to carbothermal reduction due to it being more thermodynamically favorable. Magnesiothermic reduction once again uses boron oxide and carbon, however, magnesium replaces the carbon as the reducing agent. The magnesiothermic reduction reaction goes as follows,

$$2B_2O_3 + 6Mg + C \rightarrow B_4C + 6MgO \quad (8)$$

This reaction takes place in two steps. The first being,

$$2B_2O_3 + 6Mg \rightarrow 4B + 6MgO \quad (9)$$

and the second step,

$$4B + C \rightarrow B_4C \quad (10)$$

The reaction is highly exothermic with ΔH°=-1812 kJ/mol. Due to it being highly exothermic, once the reaction begins it is self-propagating and requires significantly less energy as compared to the carbothermal reduction. The major drawback to the magnesiothermic reduction method is the product contains magnesium oxide and magnesium borides. The magnesium oxide is easily washed away using aqueous solutions however, the magnesium boride remains in the powder. The cost of magnesium also makes this a less desirable route as compared to the carbothermal reduction.[3]

Synthesis of boron carbide from its elements produces a pure, stoichiometry controlled powder. This can be done a variety of different ways including, sintering and crushing, mechanical alloying and shock wave techniques.[32, 33, 34] However, elemental boron is highly expensive, therefore, synthesis from elements is often only used in small scale research settings. Synthesis from elements is often used when enriched B^{10} is desired for nuclear studies.

Vapor phase synthesis is used to make boron carbide thin films and coatings. A typical vapor phase reaction is as follows:

$$4BCl_3 + CCl_4 + 8H_2 \rightarrow B_4C + 16HCl \quad (11)$$

The reactants shown are just some of the many possible reactants that are used for vapor phase synthesis of boron carbide. Synthesizing boron carbide powders from vapor phase is not a common practice in industry due to the cost of raw materials.

Low-temperature synthesis is possible using polymer precursors. Boron carbide has been synthesized at temperatures much less than 1500°C. The resulting powders are typically filled with impurities in the form of free carbon or boron oxide.[3]

2.1.4 Synthesis of Boron-Rich Boron Carbide

Synthesis of boron-rich boron carbide has proven to be very difficult due to the high temperatures requirements needed for synthesis. As discussed previously, industrial synthesis methods produce boron carbide that is at or near the stoichiometric B_4C chemistry. Weimer has shown using free energy minimization that boron-rich boron carbide should be possible at synthesis temperatures as low as 2027°C with adequate amounts of boron oxide (Figure 12).[35] However, the carbothermal reduction processes inherently slow heating rates make this very difficult due to the high loss of boron oxide throughout the reaction process. While the direct synthesis of boron-rich boron carbide powders has proven to be difficult, with only limited success reported by Weimer *et al.*[36], there has been some success in producing dense boron-rich boron carbide. These materials will be discussed in a following section.

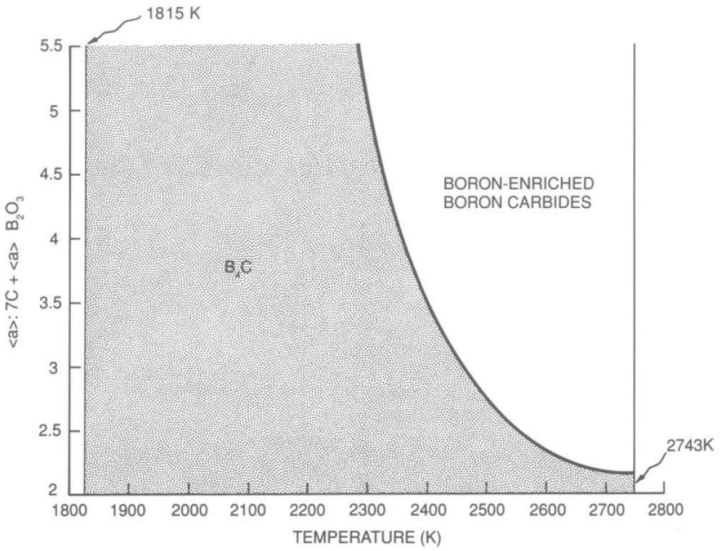

Figure 12. Temperature vs. excess boron oxide plot showing the region of boron enriched boron carbide.[28]

2.4 Processing of Boron Carbide

Processing of boron carbide is very difficult due to its highly covalent structure. Typical methods for processing of boron carbide include both pressureless sintering and pressure assisted sintering. Temperatures in excess of 1500°C are needed and very often temperatures greater than 2000°C are needed to reach full density. Application of pressure improves the densification of boron carbide and novel pressure assisted methods such as spark plasma sintering have been shown to produce fully dense boron carbide at relatively low temperatures.

2.4.1 Pressureless Sintering

Pressureless sintering of ceramics is desirable due to the ability to fabricate complex shapes without costly machining. Pressureless sintering of boron carbide, however, is very difficult and often results in incomplete densification. Along with the ability to make net shapes, pressureless sintering is fairly simple and relatively cheap. The

boron carbide powder is compacted into a green body that can withstand some amount of handling. The green body is then heated in either an inert environment at temperatures in excess of 2000°C. Factors such as particle size and surface area, oxide content, heating rate and sintering temperatures can have large effects on the final density of the boron carbide. Decreasing the particle size (increasing surface area) produces a denser boron carbide.[37] Using higher surface area boron carbide can be difficult though due to its affinity to oxidize. Sintering under vacuum or employing a low-temperature hold can help reduce the surface oxides which in turn promotes sintering.[3] Higher sintering temperatures can help increase the final density but often leads to grain coarsening due to the slow heating rates.[38] Sintering additives such a TiB_2, ZrO_2 and carbon have been used with some success. Carbon has been used successfully as a reducing agent for the surface oxide allowing for densities in excess of 95% theoretical to be achieved. Boride and carbide additives act as grain growth and crack propagation inhibitors. Overall, though, pressureless sintering cannot produce a fully dense boron carbide.

2.4.2 Pressure Assisted Sintering

Due to the long hold times required for pressureless sintered boron carbide, extreme grain growth occurs which leads to a loss of strength. By applying uniaxial loads in excess of 30 MPa, boron carbide can be sintered to 100% theoretical density with limited grain growth. The applied pressure causes particle rearrangement and plastic flow, leading to pore closure and ultimately fully dense materials. Hot pressing and spark plasma sintering are two common pressures assisted sintering techniques.[3, 39]

2.4.2.1 Hot Pressing

Hot pressing is common processing technique used for producing fully dense boron carbide. A typical hot press setup is shown in Figure 13. Boron carbide powder is packed into a graphite die and then placed into the hot press chamber. The chamber can be backfilled with an inert gas or kept at atmosphere. The die is heated by an induction coil and pressed by a uniaxial load applied by a ram above and below the die.

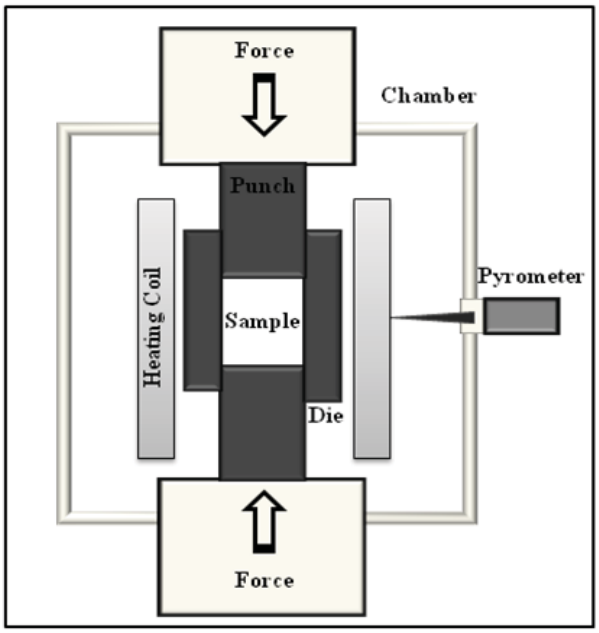

Figure 13. Basic hot press set-up.[7]

Three successive stages of sintering are seen during hot pressing. The first is particle rearrangement and reduction of the total open porosity of the compact. This first step typically occurs between 1800-1950°C. The second step involves plastic flow and the elimination of the open porosity which happens between 1950-2100°C. Finally, volume diffusion occurs at temperatures in excess of 2100°C resulting in the elimination of all remaining porosity. The final density is dependent upon many different parameters including hot press temperature, pressure, heating rates, and particle size.[3] Additive free

boron carbide can be sintered to full density by using temperatures in the range of 2100°C to 2250°C and loads between 20 MPa to 50 MPa.[3] By employing high heating rates, fully dense boron carbide was produced at temperatures as low as 1900°C while under a 40 MPa load.[40]

Much like pressureless sintering, hot press densities can be improved by using different additives. A variety of different borides and carbides have been used to lower the sintering temperature as well as improve properties such as flexural strength. Additives are also used to limit grain growth during the sintering. While the grain growth exhibited during hot pressing is not as severe as that of pressureless sintering, it is still undesirable and can reduce the overall strength of the boron carbide.

One major drawback to hot pressing is that possible shapes are often very limited without the use of extensive machining. With pressureless sintering, materials can be densified in the desired shape which requires little to no machining. Due to the extremely high hardness of boron carbide, diamond machining tools are needed to shape the hot pressed material. The cost of this machining can become prohibitively expensive however, hot pressing is still the most common technique for densifying boron carbide.

2.4.2.2 Spark Plasma Sintering

Spark plasma sintering uses a high DC current along with uniaxial pressure to produce fully dense ceramic materials. The setup of the spark plasma sintering instrument is shown in Figure 14a. It is similar to the hot press with the major difference being that the hot press uses an external heat source and pressure to sinter the material whereas spark plasma sintering employs the use of pressure plus direct current resulting in localized

heating. The die assembly is shown in Figure 14b. The die can vary in size and shape but the typical design is shown. The die is lined with graphite foil to protect from any reaction between the sample and the die. The temperature is measured using an optical pyrometer as can be seen in Figure 14a.

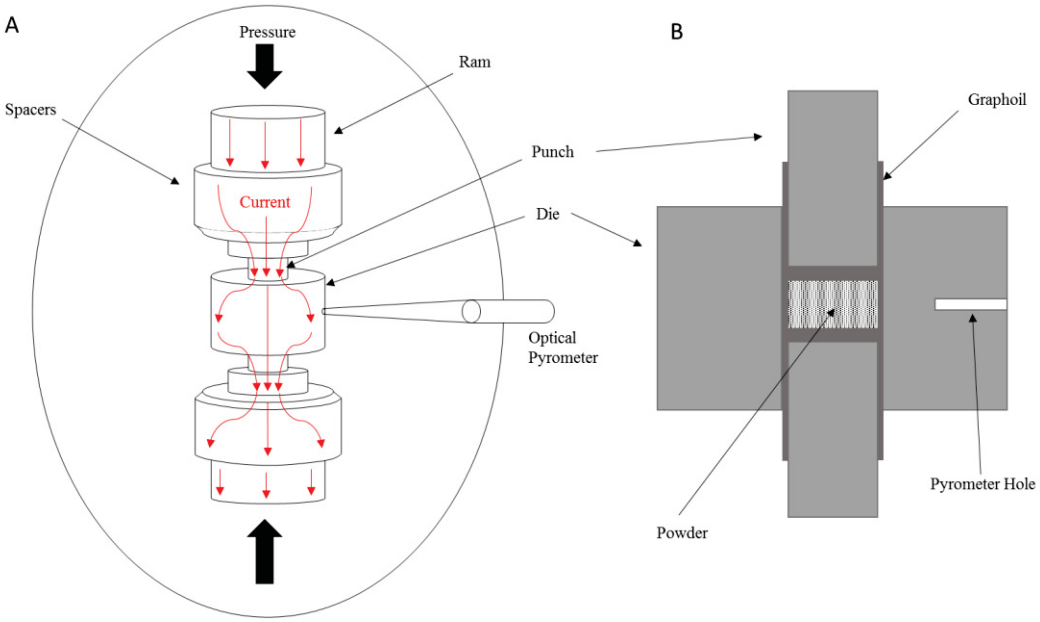

Figure 14. Schematic of a) SPS setup and b) die setup.

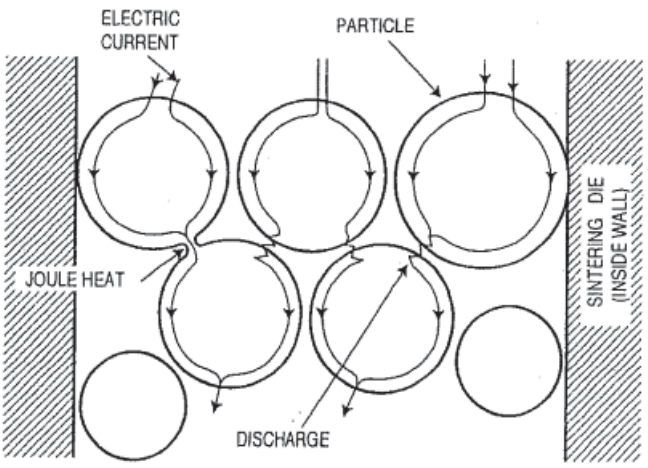

Figure 15. Current path through conductive powder for spark plasma sintering.[41]

The defining characteristic of spark plasma sintering is the use of DC current which allows for sintering to occur much faster than other sintering techniques. The current flows through the graphite die which is subsequently heated due to the resistivity. Due to boron carbide being a semiconductor, current will pass through the powder as well. This current flow causes evaporation of any oxide that may be on the surface of the boron carbide particle. The evaporation of the oxide phase promotes densification.[3] The pressure that is applied causes the boron carbide particles to come into contact with each other and therefore creates a path for the current to flow. The region where the particles are in contact with each other has a much higher resistance than the particles and therefore a locally high temperature (joule heating) is seen at these points which cause neck formation between the particles.[41] Figure 15 give an illustration of this process.

This process makes it possible to sinter boron carbide at significantly lower temperatures and much shorter times. Optimized sintering parameters varying from report to report however temperatures in the range of 1700°C to 1900°C with pressures of 30 MPa

to 75 MPa have been able to produce fully dense boron carbide. Moshtaghioun *et al*. [42] did a systematic study of the temperature and dwell time effect on the density of boron carbide. They were able to achieve 100% theoretical density at 1700°C with a 3-minute hold. As the temperature was increased, the density was not affected however there was considerable grain growth from 688 nm at 1700°C for 3 minutes up to 51 μm at 1800°C for 3 minutes. The temperatures reported in the literature can vary significantly. These variations are due to the method of temperature measurement. Optical pyrometers can be focused on different areas of the graphite die and give greatly differing temperatures thus leading to the variations in recorded temperatures reported in the literature.

Another defining characteristic of spark plasma sintering is the high heating rate that can be achieved (as high as 1000°C/min). High heating rates have been reported to improve the density of boron carbide that has been hot pressed.[40] While the heating rates in spark plasma sintering allow for densification to occur quickly with limited grain growth, higher heating rates are not always beneficial. Li *et al*.[39] has shown that a density of 94.87% theoretical could be achieved by heating to 1500°C with a heating rate of 100°C/min . However, increasing the heating rate to 150°C/min while increasing the temperature to 1550°C only achieved a density of 84.15% theoretical density. Hayun[43] showed similar results to those of Li *et al.*

2.5 Mechanical Properties

Boron carbide exhibits many exceptional mechanical properties including high hardness and high elastic modulus. The hardness of boron carbide ranks behind only that of diamond and cubic boron nitride. Knoop hardness for 100 gram loads typically ranges from about 29 GPa to 31 GPa for stoichiometric boron carbide.[44] Vickers hardness values

in excess of 37 GPa have been reported.[45] Young's modulus, shear modulus, and bulk modulus have been reported as high as 472, 200 and 247 GPa, respectively, at 20 at.% C by Gieske *et al.*[10]. The toughness of boron carbide is highly variable with most reported values between 1 MPa $m^{1/2}$ to 3 MPa $m^{1/2}$.[1, 39, 42, 45, 46] Hayun *et al*. [47] have reported values as high as 4.9 MPa $m^{1/2}$ for near fully dense boron carbide. Poisson's ratio has been reported between 0.14 and 0.18.[48, 49, 50] The mechanical properties, however, are dependent upon a number of different factors, the most important of those being; secondary phases, porosity, grain size, and stoichiometry.

2.5.1 Effect of Secondary Phases

Due to the difficulty in sintering boron carbide, sintering aids have commonly been used. The sintering aids form secondary phases within the dense boron carbide, which may both improve and degrade the mechanical properties of boron carbide depending on the type and amount of secondary phases present. Some of the most common additives are; C, TiB_2, Al_2O_3, ZrO_2 and TiO_2.

Carbon is used extensively as a sintering additive due to its effectiveness in reducing the surface oxide layer on the boron carbide powder.[3] However, some residual carbon may exist in the dense microstructure which can have a detrimental effect on the mechanical properties of the boron carbide Farbaniec *et al*.[51] showed that the carbon inclusions that are formed from the unreacted free carbon act as crack initiation sites which aids in failure (Figure 16). Additives are also used to control grain growth and act as crack propagation inhibitors.[3] Additions of TiB_2 up to approximately 15 vol.% improves the bend and flexural strength of boron carbide.[52] Pressureless sintered boron carbide with 3 wt.% of Al_2O_3 achieves significantly higher density than additive free pressureless

sintered boron carbide.[53] ZrO_2 has been shown to increase flexural strength and density of both pressureless sintered and hot pressed boron carbide. At high ZrO_2 additions, the benefits are lost and a slight decrease in flexural strength and hardness are seen.[54] While these additives have been shown to help in densification and impede crack propagation, great care has to be taken as any large changes in the coefficient of thermal expansion of the two materials can lead to micro-cracking and premature failure of the material.

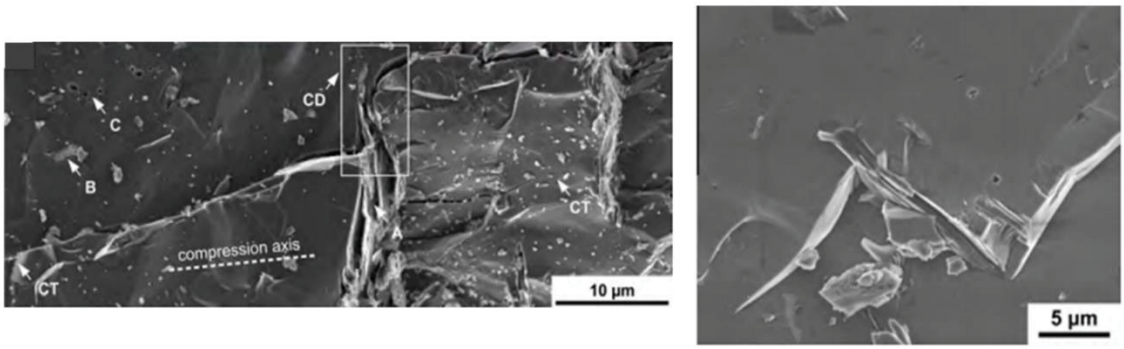

Figure 16. SEM micrograph showing carbon inclusions that have become crack initiation sites. Left) The carbon inclusion is located in the middle of the sample (A) with cracks emanating from it to the crack tip (CT). A crack deflection can be seen as well (CD). B and C are an impurity inclusions and pore respectively. Right) Wing cracks emanating from a carbon inclusion.[51]

2.5.2 Effect of Porosity

Porosity can also have a significant effect on the mechanical properties of boron carbide. Hardness has been shown to have an exponential relationship with porosity. Rice[55] was able to determine this relationship using a minimum solid area model. His resulting equation goes as follows:

$$H \sim H_0 e^{-bP} \tag{12}$$

where b is a parameter determined by the characteristics of the porosity (spheres, cylindrical, etc.) and P is the volume fraction of porosity in the sample. Common values of b for carbides fall between 5 and 8. Experimentally, Vickers hardness has been shown

to have a significant decrease from 2300 kg/mm^2 at 93% theoretical density down to 1850 kg/mm^2 at 90.4% theoretical density. Sairam *et al*.[56] were able to show similar results for hardness.

Young's modulus is also highly affected by an increase in porosity. Hollenberg[57] determined the relationship between porosity and modulus using the following equation,

$$E = 460\left[\frac{1-P}{1+2.999P}\right] GPa \tag{13}$$

Using this equation, the Young's modulus drops from approximately 460 GPa at 0% porosity to approximately 260 GPa at 15% porosity. The fracture toughness follows the opposite trend, as the porosity increases the toughness also increases.[46] This increase is due to the porosity impeding the crack propagation. Figure 17 summarizes the results for the effects of porosity on the three commonly measured static mechanical properties discussed. It should be noted that experimental setups are not the same for all the data plotted in Figure 17, however, the trends are similar regardless of the experimental conditions.

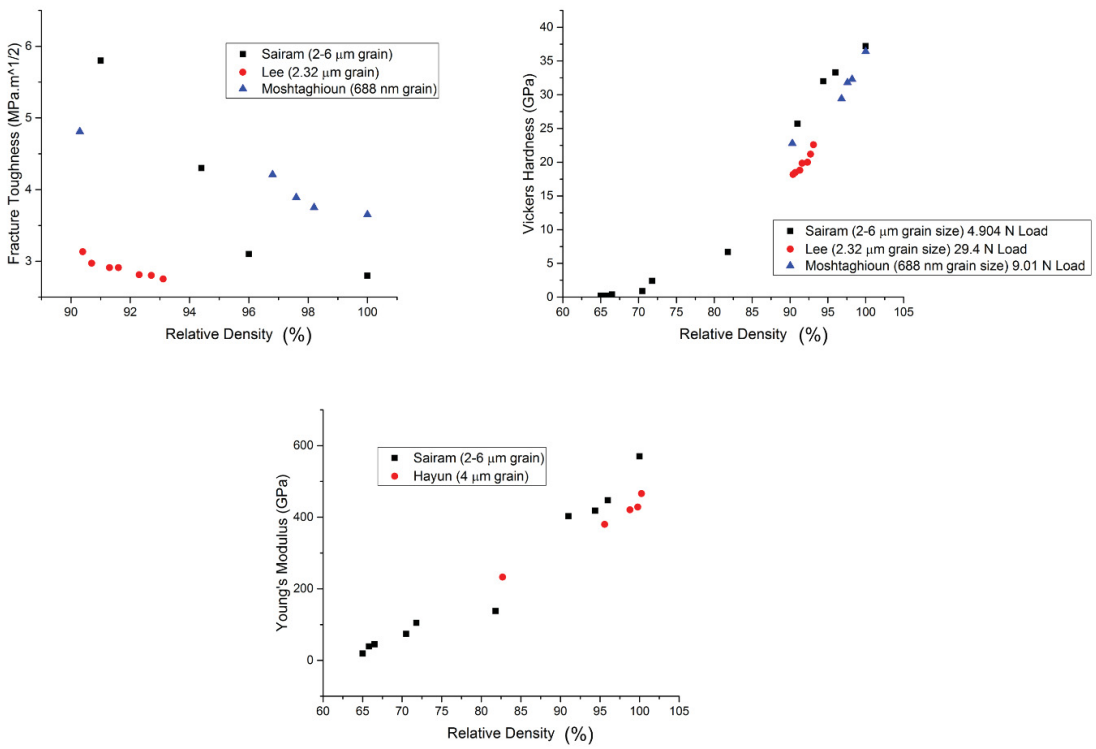

Figure 17. Effect of relative density on the fracture toughness, Vickers hardness and Young's modulus of boron carbide.[46, 47, 56, 58]

2.5.3 Effect of Grain Size

Grain size has a well-known effect on the hardness and strength of polycrystalline ceramics. The Hall-Petch relation is commonly used to describe the grain size effect in ceramics at small grain sizes.[59] The Hall-Petch relationship is as follows:

$$H = H_0 + kD^{-\frac{1}{2}} \tag{14}$$

This effect can be seen in the data of Figure 18. Moshtaghioun's[58] data shows the expected Hall-Petch relation between hardness and grain size except for the smallest grain size of 120 nm. This is explained by a slight decrease in the relative density of that particular sample. The fracture toughness of the same samples shows the same relationship, as the grain size is decreased from micrometers to sub-micrometer the fracture

toughness increases. Lee *et al*.[46] at Georgia Tech reported similar results for their samples for both hardness and fracture toughness. Reddy *et al*.[60] employed instrumented nanoindentation to determine the hardness and indentation fracture toughness of boron carbide with 40-150 nm grains. Their results revealed hardness and modulus values that were comparable to most microcrystalline values reported. However, the fracture toughness for these samples was nearly 1 to 2 MPa.m$^{0.5}$ higher that of reported microcrystalline results.

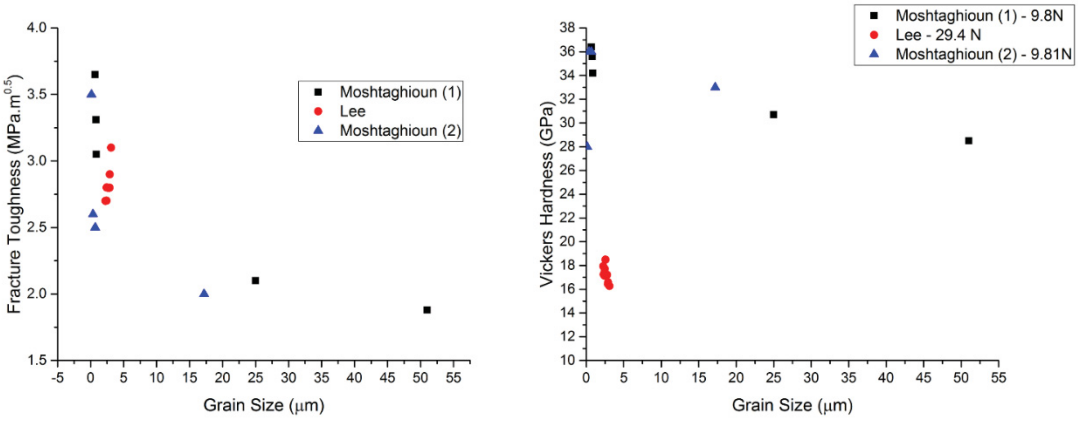

Figure 18. Effect of grain size on the fracture toughness and Vickers hardness of boron carbide.[46, 58, 61]

2.6 The Problem with Boron Carbide

As discussed in the previous section, boron carbide has many attractive properties which make it the material of choice for ceramic armor applications. However, boron carbide often underperforms other common armor ceramic under high-pressure conditions. This unexpected result can be explained by examining boron carbide microstructure and dynamic response.

2.6.1 Commercially Available Boron Carbide Powders

Commercial synthesis of boron carbide is an energy intensive and inefficient process which results in a heterogeneous product. Chemical gradients are commonly exhibited in the boron carbide ingots synthesized by carbothermal reduction which leads to chemical variabilities in the final powders. Areas that are not fully reacted contain large amounts of free carbon which often end up in the final powder and the post processing that is needed to crush the ingots introduces further impurities. Small amounts of carbon additions have been shown to be beneficial to sintering and grain growth prevention. However, the inclusions that are formed in the microstructure due to the excess carbon can become crack initiation sites which ultimately degrade the performance of the material.

Chen *et al*.[61] and Xie *et al*.[62] extensively examined the microstructure of armor grade hot pressed boron carbide ceramics plates. The results of both papers conclusively determined that the armor grade commercial plates contained large amounts of impurities in the form of C, Fe, Al, Si, V, Ti, Cr and Mo[62, 63]. Furthermore, Chen *et al*. determined that even 1 wt. % decrease (98.5 wt. % purity) in the purity level of the material can have a large effect on the properties of the boron carbide. Impurities accumulate at triple junctions where, due to the thermal expansion mismatch, micro-cracking may result. The micro-cracking has the potentially to degrade the mechanical properties depending on the size and number of micro-cracks within the material.

While these impurities have negative effects on the mechanical properties of boron carbide when located at triple junctions, intergranular films (IGF's) can potentially improve the performance of the material by introducing inter-granular fracture. Chen *et*

al. and Xie *et al*. determined that the impurity phases do not form IGF's and therefore the fracture mode did not change.

Uncontrolled additions of secondary phases degrade the properties of boron carbide. Due to the crude nature of the boron carbide synthesis process, there is a very limited control on the ultimate purity of the powders. For this reason, commercially available boron carbide powders are difficult to study and understand due to the wide variety of potential failure mechanisms.

2.6.2 Amorphization and Loss of Shear Strength

At high strain rates boron carbide exhibits anomalous behavior, which leads to catastrophic failure. Understanding of the dynamic behavior of boron carbide becomes extremely important for engineering a better material.

In early 1990's, Grady[5] used planar shock and release wave experiments to look at the dynamic response of boron carbide and silicon carbide. Given that these two materials are strongly covalent solids, a similar response to dynamic stress is expected. Nonetheless, it was found that upon reaching each materials respective Hugoniot elastic limit major differences in the material response is seen. Boron carbide undergoes post yield softening, whereas the silicon carbide exhibited post yield hardening (Figure 19). This post yield softening is an indicator of catastrophic loss of strength in boron carbide upon reaching the Hugoniot elastic limit (18-20 GPa). Similar work done by Dandekar[64] at the Army Research Labs in 2001 showed once again that upon reaching the Hugoniot elastic limit, the boron carbide underwent a catastrophic loss of strength. This loss of strength was observed irrespective of the grade of boron carbide used. However, neither group was able to pinpoint the cause for this loss in shear strength.

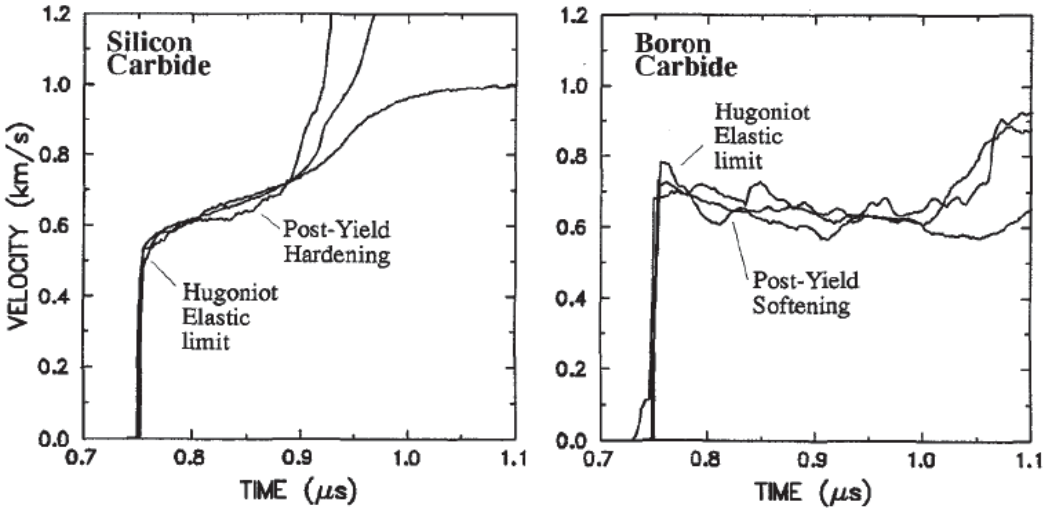

Figure 19. Elastic precursor wave profiles detailing the significantly different response to impact in the two materials. Silicon carbide retains strength after impact, exhibiting a post yield hardening. Boron carbide loses strength after impact, exhibiting post yield softening[5].

Raman microspectroscopy work carried out by Domnich *et al*.[65] was one of the first to report a potential phase change in boron carbide after the application of high pressures. Two single crystal specimens with differing orientations were examined ($(0001)$and $(10\overline{1}1)$) using nanoindentation. A series of nano-indents were made ranging from 10 to 300 mN in load. Raman microspectroscopy was then used to analyze the indents. What was found was a new set of peaks at high wavenumbers (Figure 20). These new peaks were suggested to arise due to disorder or amorphization resulting from the destruction of the boron carbide atomic structure. However, the phase change was not fully identified at the time of the report and a definitive conclusion was not possible.

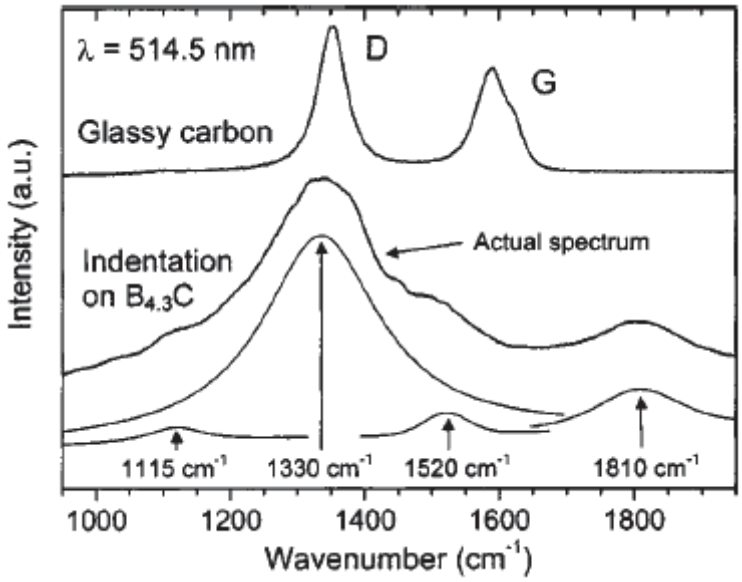

Figure 20. Raman spectra of a 100mN indent showing the formation of Raman peaks at 1330 cm^{-1} and 1810 cm^{-1}. Also shown is the glassy carbon Raman spectra for comparison.[65]

In 2003, a group at Johns Hopkins University[4] used a high-resolution transmission electron microscope to observe fragments of boron carbide that had undergone ballistic impacts. The results of their work showed that above a critical projectile velocity of approximately 860 to 890 m/s, an amorphous region formed within cleavage planes (Figure 21). Below the critical projectile velocity, these amorphous regions were not present. This work suggests that the onset of amorphization at high impact pressures may be the cause of the dramatic reduction in the strength of boron carbide.

Between the lack of high purity boron carbides available commercially and the anomalous behavior that boron carbide exhibits under shock loading, boron carbide underperforms other available ceramic materials. This leads to a need for a better-engineered material that may potentially withstand a shock more like its silicon carbide

counterpart. Boron-rich boron carbide has been suggested to be such a material for reasons that will be discussed in the next section.

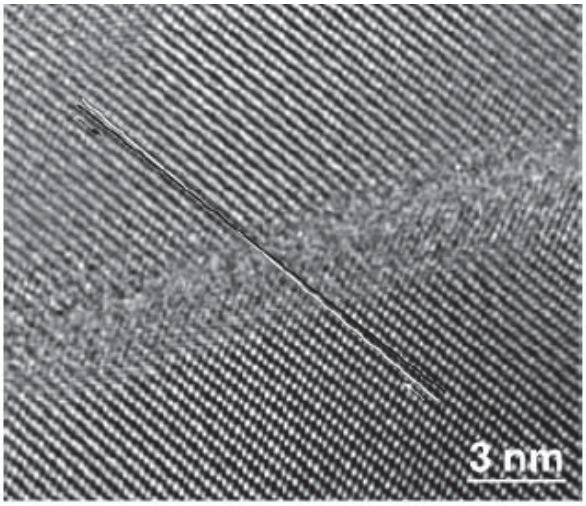

Figure 21. The amorphous band within a cleavage plane in boron carbide. Imaged using HRTEM.[4]

2.7 Why Boron-Rich Boron Carbide?

2.7.1 Thermodynamically Favorable

The structure of boron carbide is a constantly debated topic due to the many atomic configurations possible across the large solid solubility range as highlighted in section 2.1. Determining the exact site occupancies in boron carbide has been challenging. Saal *et al*.[66] , however, was able to use ab initio calculations to determine lattice parameter and enthalpy of formation values for 24 different structures ranging from the carbon-rich (21.43 at.% C) to pure boron. Table 2 shows the results of these calculations. Examining the lattice parameters and comparing them to known experimental results only 3 phases are likely: $B_{11}C$(CBC), B_{12}(CBC) and B_{12}(BVaC). These three structures correspond to 20 at.% C, 13.33 at.% C and 7.14 at.% C respectively. Further examination of the enthalpies of formation from the ab initio calculations show the $B_{11}C$(CBC) and B_{12}(CBC) structures to

be thermodynamically stable while the B_{12}(BVaC) has a positive enthalpy of formation which would be expected as 7.14 at.% C is outside of the solid solubility range reported by many phase diagrams (a two-phase region including boron). The calculated enthalpy of formation for the carbon-rich structure, $B_{11}C$(CBC), agrees well with experimental results. These results reported by Saal show that boron-rich boron carbide is a thermodynamically stable phase that should be easily formed as compared to other structures. This fact is significant since previously reported results suggest that boron carbide is very difficult to synthesize with a boron-rich chemistry.

Table 2. Enthalpies of formation and lattice parameters of various possible boron carbide and boron atomic configurations.[66]

	Structure	at. % C	ΔH_f	a (Å)	c (Å)
1	B_{12} BBB	0.00	20.03	5.808	12.017
2	B_{12} BBVa	0.00	20.76	5.570	12.097
3	B_{12} BVaB	0.00	12.31	5.721	12.261
4	B_{12} BVaVa	0.00	21.14	5.718	12.260
5	B_{12} VaBVa	0.00	42.89	5.226	11.661
6	B_{12} VaVaVa	0.00	0.00	4.902	12.542
7	B_{12} BBC	6.67	1.34	5.654	11.898
8	***B_{12} BVaC***	***7.14***	***6.43***	***5.628***	***12.276***
9	B_{12} CBVa	7.14	6.29	5.493	11.917
10	B_{12} CVaVa	7.69	7.46	5.362	12.371
11	***B_{12} CBC***	***13.33***	***−7.89***	***5.656***	***12.122***
12	B_{12} CVaC	14.29	−3.35	5.555	12.236
13	$B_{11}C$ BBB	6.67	7.19	5.730	11.558
14	$B_{11}C$ BBVa	7.14	11.53	5.714	11.911
15	$B_{11}C$ BVaB	7.14	11.53	5.714	11.909
16	$B_{11}C$ BVaVa	7.69	20.41	5.515	11.971
17	$B_{11}C$ VaBVa	7.69	20.41	5.516	11.969
18	$B_{11}C$ VaVaVa	8.33	12.30	4.972	12.281
19	$B_{11}C$ BBC	13.33	4.34	5.665	11.857
20	$B_{11}C$ BVaC	14.29	6.01	5.618	11.911
21	$B_{11}C$ CBVa	14.29	4.65	5.503	11.648
22	$B_{11}C$ CVaVa	15.38	13.91	5.318	12.076
23	***$B_{11}C$ CBC***	***20.00***	***−10.78***	***5.597***	***12.057***
24	$B_{11}C$ CVaC	21.43	−1.03	5.534	11.853

2.7.2 Quasi Plasticity and Increased Shear Strength

Considerable modeling and experimentation have been done on interface defeat (projectile penetrates the surface of the material being impacted) and penetration of ceramics subjected to ballistic impact. Horri and Nemat-Nassar[67] were the first groups to model the brittle-ductile transition in materials. Within their brittle-ductile transition model, they introduced a ductility parameter, Δ, which is a function of several material properties. The ductility parameter, along with the confining stress, σ_2/σ_1, was found to have a great impact on the qualitative and quantitative performance of the model. By plotting the ductility parameter, Δ, with the confining stress, σ_2/σ_1, it was determined that there are three distinct regions that determine how a particular material will fail: a brittle region, a transitional region, and a ductile region (Figure 22). These findings showed that boron carbide is significantly influenced by a set of materials parameters that include, τ_y (shear strength), Δ, μ (coefficient of friction of the crack surfaces), ν (Poisson's ratio) and l_t/c (ratio of tensile crack length to flaw length).

In 2000, Lundberg *et al*.[68] showed that the transition velocity (velocity at which a projectile transitions from surface dwell to penetration) was a function of the material yield strength. An upper and lower bound was estimated for the transition impact velocity vs yield strength, shown in Figure 23. The lower bound describes "incipient plastic yield" whereas the upper bound describes "large scale plastic yield". The lower bound describes a material that is very brittle and fractures easily (boron carbide) as compared to the upper bound which describes a more ductile material (silicon carbide).

Using the brittle-ductile transition model developed by Horii and Nemat-Nasser, along with the transition velocity model developed by Lundberg, LaSalvia[69] was able to

show that the lower bound of the Lundberg model is not static and is actually a function of the materials properties introduced by Horii and Nemat-Nassar. By altering any of the material properties discussed previously, the lower bound of the Lundberg curves can be moved to the upper bounds, which in theory should cause the material to act in a more ductile manner. Figure 24 shows how the material properties alters the lower bound.

More recently, Taylor *et al*.[70] at the Army Research Labs modeled the effect of the atomic structure on the shear strength of boron carbide. Three different atomic configurations were used; B_{12}(CCC), $B_{11}C_p$(CCB) and B_{12}(CBC). The first two configurations contain twelve boron atoms and three carbon atoms, whereas the third is the boron-rich configuration containing thirteen boron atoms and two carbon atoms. Stress-strain curves were developed for each configuration (Figure 25). Each configuration has the uniaxial compression stress-strain curve as well as four stress-strain curves where a third stress was applied along the three atom chain, creating shear. The results show that the boron-rich atomic configuration has an increase in shear strength of approximately 10 GPa over the other two configurations. This increase in shear strength coupled with the work done by Horii and Nemat-Nassar, Lundberg and LaSalvia would suggest that boron-rich boron carbide could potentially perform better under shock loading.

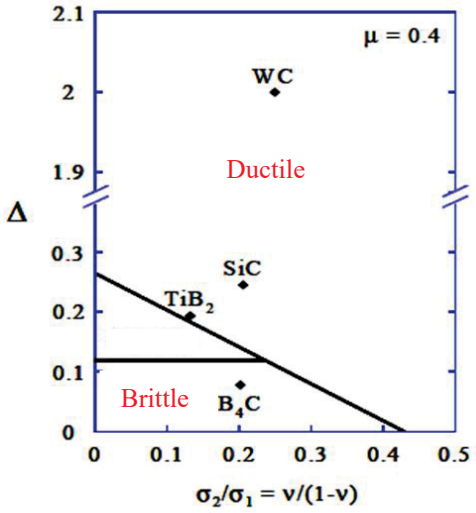

Figure 22. Ductility parameter vs. relative confining stress of ceramic materials (coefficient of friction on crack face μ=0.4).[69]

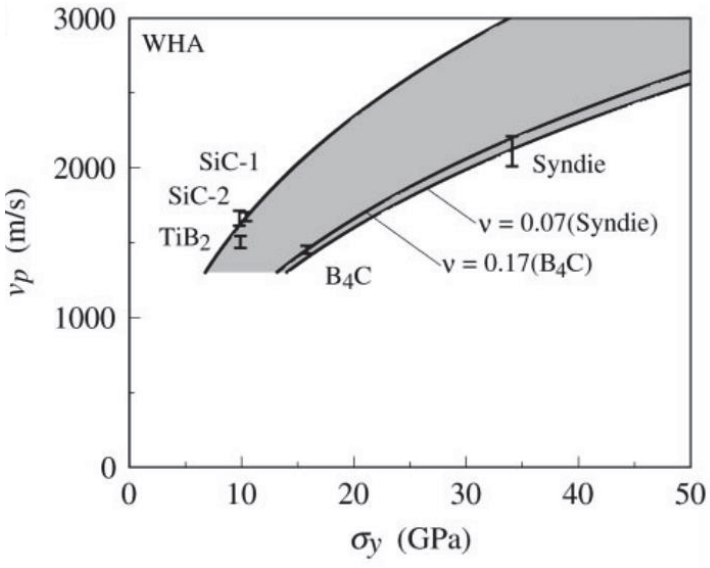

Figure 23. Impact transition velocity vs target yield strength of various materials.[68]

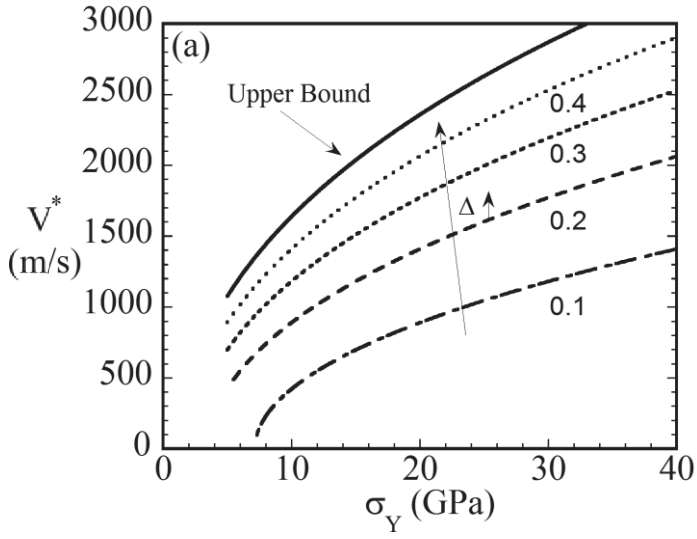

Figure 24. As ductility parameter increases the lower bound of Lundberg's plot increases towards the more ductile upper bound.[69]

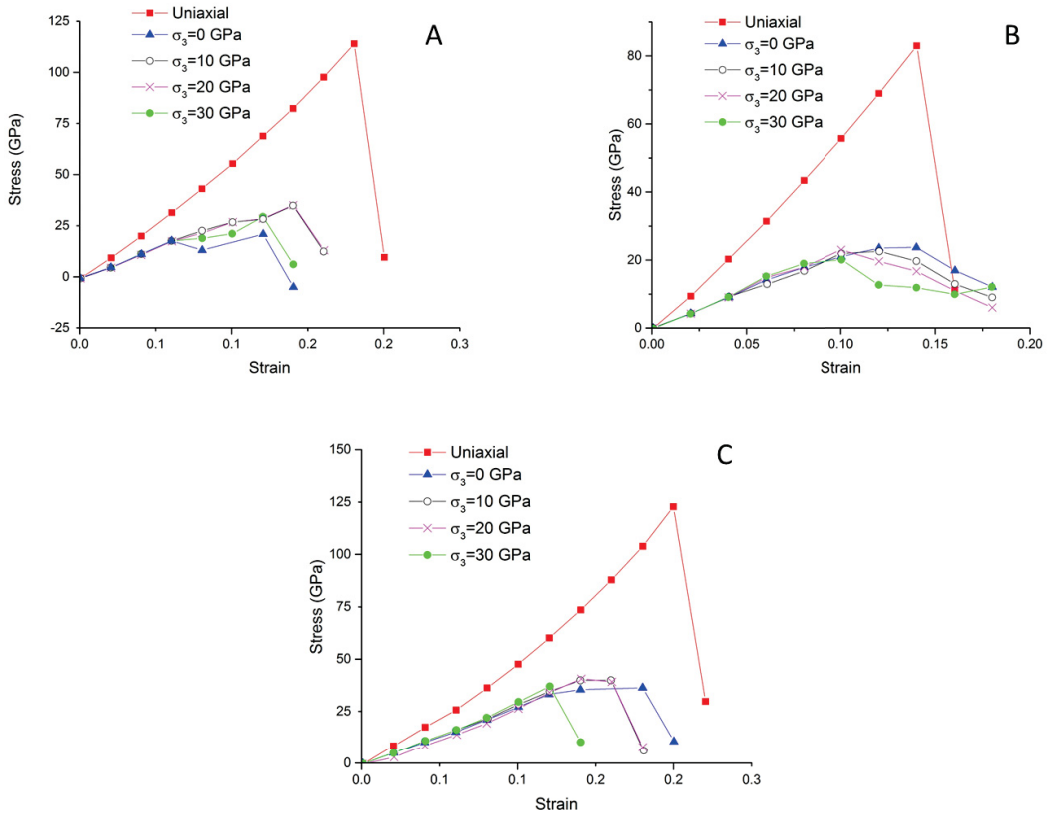

Figure 25. Stress-strain curves for three atomic configurations of boron carbide A) B_{12}(CCC), B) $B_{11}C$(CBC), C)B_{12}(CBC)[70].

Furthermore, DFT modeling of the amorphization process in boron carbide has also shown that the elimination of the B-C inter-icosahedron bond may decrease or even eliminate the amorphization problem seen in boron carbide. An *et al*.[71] reported that the slip system $(01\bar{1}\bar{1})/\langle\bar{1}101\rangle$ has the lowest shear strength of all theoretical slip systems in boron carbide. Further, the B-C inter-icosahedron bond on the slip plane breaks and ultimately leads to the collapse of the icosahedron (Figure 26). With the elimination of this bond (changing the atomic configuration) their models showed no amorphization. This suggests that by moving to the boron-rich configuration of $B_{12}(CBC)$ may help mitigate amorphization.

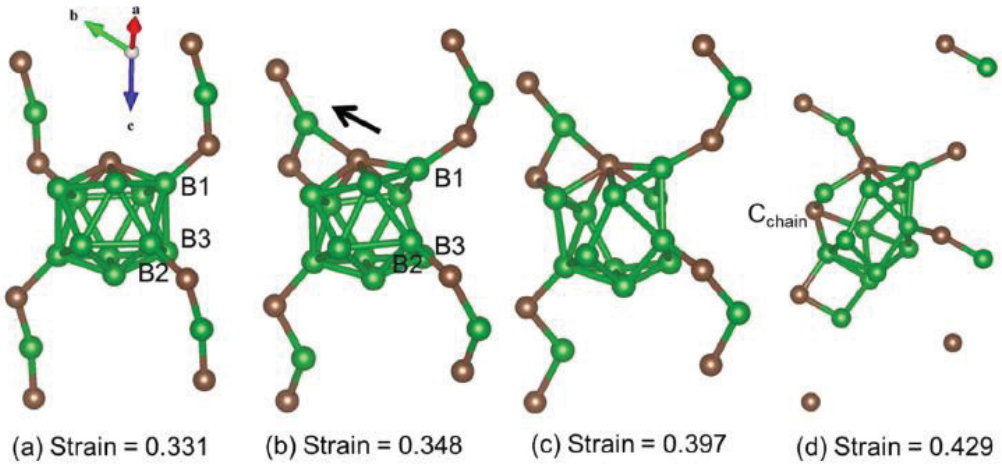

Figure 26. DFT model of the collapse of 12 atom icosahedra under varying amounts of shear strain. The collapse of the 12 atom icosahedra leads to amorphization.[71]

2.8 Previous Work in Boron-Rich Processing

While the boron carbide phase diagram contains a large solid solubility range in which boron carbide can be synthesized, commercial synthesis results in materials with stoichiometries near B_4C. Due to the difficulty in synthesizing boron-rich boron carbide

powders, boron-rich boron carbide research has focused on processing boron carbide with certain additions of boron as well as other less common techniques like CVD and elemental processing. Ekbom was one of the first researchers to attempt to understand the effects of the boron to carbon ratio on the properties of boron carbide. Using commercially available powders mixed with boron Ekbom[24] was able to produce a boron carbide with a composition near $B_{13}C_2$. He further showed the strength of the boron-rich boron carbide sample (590 MN/m^2) was nearly twice as high as the boron carbide sample with no additions (320 MN/m^2). This was the first work showing the potential benefits of producing boron-rich boron carbide.

Further research was done in following years by Champagne and Angers[9], Bouchacourt and Thevenot[72] and Niihara[8]. Champagne and Anger's research focused on mechanical properties, specifically the elastic modulus and flexural strength of boron carbide with up to 15 wt. % amorphous boron additions. Their results, however, showed no significant trends. Bouchacourt and Thevenot examined the correlation between the thermoelectric properties and the stoichiometry across the whole solid solubility range of boron carbide. By using boron additions during hot pressing, it was possible to produce boron carbide with controlled chemistries across the solid solubility range. Niihara's work was the first to show a significant and reproducible trend. Boron carbide was produced with varying stoichiometries by chemical vapor deposition and the Vickers hardness and fracture toughness were then measured. The results revealed B_4C (20 at. % C) to have both the highest hardness and highest fracture toughness of all the compositions measured. Niihara's results were the first to show a clear trend in the mechanical properties across the

entirety of the solid solubility range. After Niihara's work, little research was done in boron-rich boron carbide until the early 2000's.

Three additional groups examined boron-rich boron carbide in varying capacities in the 2000's starting with Larsson and Hogmark[11]. Larsson and Hogmark focused on the erosion resistance of boron-rich boron carbide along with the Vicker's hardness and fracture toughness. While they were able to achieve better erosion resistance with an increase in boron additions, they were not able to show any significant trends in the Vicker's hardness or fracture toughness of their materials. Chheda[12] followed with a report examining many properties of boron-rich boron carbide both static and dynamic. Once again, no clear change was seen in the Knoop hardness values or the Young's modulus. While an increase in the fracture toughness was reported, the scatter in the data leaves some uncertainty to the actual significance of this trend. Furthermore, Chheda reported that the ballistic performance of a single composition of boron-rich boron carbide was much worse than that of a comparable carbon-rich boron carbide. This was most likely due to residual stresses in the hot pressed plates but no further results were reported. Most recently, Roszeitis[73] published work examining the thermoelectric properties of boron-rich boron carbide with no characterization of the mechanical properties.

While there has been significant work done in the field of boron-rich boron carbide, results have often been inconclusive and contradicting. The major issue with the bulk of the reported results is the effect of the impurities of the starting powders and the defects introduced during processing mask the true effects the chemistry change has on the boron carbide. Therefore, elimination of these impurities and defects are imperative to gaining a true understanding of the effect of the boron carbide stoichiometry. This can be seen in a

limited manner when examining the results reported by Niihara. The CVD method results in very high purity, fully dense materials that would show a potential effect of stoichiometry on the Vicker's hardness and fracture toughness. Unsurprisingly, Niihara's data was the only reported data showing a trend. However, for more traditional materials, a more systematic study of high purity boron-rich boron carbide is required.

3. Method of Attack

3.1 Objective 1: Synthesis of Phase Pure, Equiaxed Boron Carbide Powders for Use in Boron-Rich Boron Carbide Processing

Objective one of this thesis was to synthesize high purity boron carbide powders using rapid carbothermal reduction. Synthesized powders were fully characterized using a variety of techniques as outlined in the following sections. By employing rapid carbothermal reduction and using a vertical graphite resistance furnace it was possible to synthesize boron carbide powders with little to no free carbon impurities that require no post processing, in turn, eliminating any possible metallic impurities.

3.1.1 Precursor

Boron carbide precursor is an intimate mixture of H_3BO_3 and a carbon source. For this study carbon, lampblack was used. In one beaker, H_3BO_3 was dispersed in water at ~90°C and stirred until proper dispersion was achieved. Carbon was mixed with water with a small amount of dispersant (Triton X-100) and heated slightly and stirred until properly dispersed. Once the boric acid and carbon had been dispersed, they were mixed together and heated to ~300°C to evaporate off all of the excess water in the mix. The mixture eventually turns to a thick slurry at which time the mixture was placed into a dryer at 110°C and allowed to dry overnight. The dried mixture was placed into crucibles and calcined for 2 hours at 600°C. The calcined material was hard and requires crushing to achieve the required size for feedstock. Crushing was done in an alumina mortar and pestle and was carried out in steps to help prevent over crushing of the material. Between steps, the crushed material was placed into a set of sieves (800 μm, 425 μm, and 150 μm) and the

powder was separated into coarse (>800 μm) and fine powder (<150 μm) along with the desirable size of 150 to 425 μm. The crushed precursor was kept in a humidity controlled dry box to prevent the conversion of B_2O_3 back to H_3BO_3.

Boron oxide is the key reactant in the synthesis of boron carbide. At ~1200°C $B_2O_3(s)$ begins to convert to $B_2O_2(g)$ causing the boron source to become depleted. While the RCR reaction is a gas-solid reaction, the reaction does not occur until temperatures are in excess of 1540°C. To ensure that carbon was the limiting reactant in the reaction, excess B_2O_3 was added. It has been reported that ~50 % excess B_2O_3 is needed to synthesize stoichiometric boron carbide at 1850°C.[31] All boron carbide precursor for this work was produced using 50% excess B_2O_3.

3.1.2 Reaction in High-Temperature Inert Furnace

Synthesis of high purity, submicron boron carbide requires very high temperatures (>1800°C) and extremely fast heating rates (~10^5 K/sec). To achieve both of these, rapid carbothermal reduction synthesis route was employed. The reaction of the precursor outlined in the previous section was carried out in a Thermal Technologies graphite resistance furnace. The boron carbide/boron oxide mixtures were fed into the furnace by a screw feed system.

The graphite resistance furnace used in this work (Figure 10) has a maximum operating temperature of ~2000°C however, due to limitations on the high-temperature thermocouples, the max operating temperature was kept at 1900°C. The furnace operates in an argon environment and is water-cooled to prevent overheating. The temperature was measured by a type K high-temperature thermocouple inserted into the hot zone. A controlled rate screw feed system was used to feed the precursor through a water-cooled

copper cold finger into the furnace. The cold finger ensures that the boron oxide does not melt in the transport tube and subsequently block the flow of precursor. Once the precursor has fallen through the cold finger, it enters the hot zone. The hot zone is comprised of the graphite elements with a sacrificial graphite retort that protects that element from attack during the reaction. A graphite crucible sits on an insulated hearth at the bottom of the hot zone to collect the reacted boron carbide powder. Both the argon flow and the gaseous by-products of the reaction flow out through the hearth into a filter. Upon completion of the reaction, the furnace was powered down and allowed to cool naturally. Once cooled, the powder was removed from the graphite crucible and washed to remove any excess boron oxide left over from the reaction.

3.1.3 Powder Washing

Synthesized powders often contains some residual boron oxide due to the large amounts of excess that was used to ensure a complete reaction. However, boron oxide was easily washed out using one of two possible methods. The first method uses aqueous HCl with a pH of approximately 3.5 to remove the boron oxide. The powder was dispersed into the aqueous HCl using an ultrasonic bath and then heated slightly for 30 minutes. The mixture was then set aside to allow the powder to settle to the bottom. Once the powder had settled, the solution was decanted and DI water was used to rinse the remaining powder, the mixture was once again sonicated and set aside to allow for the powder to settle followed by another decanting. This step was repeated as needed to ensure that all acid was removed. The final step was to mix the boron carbide with ethanol to remove all residual water and then it was placed in a dryer at 110 °C to evaporate the ethanol. The second method used methanol instead of the HCl solution. Methanol can easily dissolve

the boron oxide and typically only one wash was needed but was repeated as necessary. This method was used only after the synthesized powder has been washed using the HCl solution.

3.1.4 Characterization of Boron-Rich Boron Carbide Powders

A suite of characterization tools were used to determine chemistry and analyze uniformity of synthesized boron carbide powders.

3.1.3.1 X-ray Diffraction

X-ray diffraction was used to determine the powder purity. A Panalytical X'Pert x-ray diffractometer with a Cu Kα x-ray source at 45 kV and 40 mA was used for phase analysis. A continuous scan over a range of 10° to 90° 2θ was determined to be the optimal range for complete phase analysis. Powders were dispersed onto a single crystal silicon zero background holder and placed on a rotating stage. Using Jade software, the background of the powder pattern was determined and the diffraction peaks were fit to their respective phases. Phases other than boron carbide that were present in the diffraction patterns were labeled as impurities and were highly undesirable in a final product. Common impurity phases that were examined are carbon, boron nitride and iron-containing phases. Free carbon is the most prevalent and likely the only impurity to be present in this work. Two forms of free carbon can be present, graphitic and amorphous. The main peak for free carbon is at 26° 2θ.

3.1.3.2 Chemical Analysis

Three chemical analysis tools were used for determining the boron carbide powder chemistry.

3.1.3.2.1 LECO Carbon Analysis

A LECO CS230 C/S analyzer was used to determine the total weight percent carbon present in the boron carbide powder. The CS230 uses a combustion method in which the boron carbide sample was combusted in a flow of ultra high purity oxygen. The carbon that was released during the combustion was oxidized to form CO_2. This CO_2 gas that was formed flowed through an infrared detector within the LECO CS230. CO_2 absorbs infrared energy at specific wavelengths, energy differences in the infrared energy of the cell can be measured and the total amount of CO_2 could be determined. A minimum of three analyses for each sample was performed to ensure statistical significance. A series of three blank and three standard material analyses were done to calibrate the instrument on a daily basis. Samples were then carefully weighed out to 0.10g and placed in a pressed alumina crucible with iron accelerators which helped aid in combustion. The crucibles were heated inside a small induction coil within the CS230 and the combustion and subsequent measurement occurred. Sample and crucible were removed and allowed to cool before disposal.

3.1.3.2.2 LECO Oxygen Analysis

A LECO TC600 O/N analyzer was used to determine the total wt.% oxygen present in the washed boron carbide powders. The TC600 once again combusts the sample and releases CO_2, however, the oxygen from the sample reacts with the carbon from the graphite crucible to form the CO_2. The oxygen content was measured in the same way as the carbon, infrared energy absorption, as discussed previously. Much like the CS230 operating procedure, three blanks, and three standard material analyses were performed to calibrate the instrument followed by a minimum of three sample analyses. The TC600 sample crucibles are two pieces, a graphite crucible in which graphite and nickel flux are

placed and a nickel capsule in which the sample material was placed. Once again these crucibles were placed inside of a furnace and heated to initiate the combustion and measurement. Both the graphite crucible and melted nickel capsule were removed and allowed to cool before disposal.

3.1.3.2.3 Boron Titration

Boron titration was used to determine the total boron present in the boron carbide powders. ASTM standard C791-04 was followed for all analyses. The RCR boron carbide powder was mixed with sodium carbonate and subsequently fused to break down the boron carbide. Carbon dioxide was removed using a series of filtering and heating steps which leaves only boric acid. The boric acid was then titrated using a sodium hydroxide solution and the mannitoboric acid procedure.

3.1.3.3 Particle Size Analysis

Particle size analysis was done using a Malvern Mastersizer 2000 light scattering particle sizer. This system in combination with the Hydro 2000S wet sample accessory utilizes dynamic light scattering to determine the particle size distribution. The Mastersizer 2000 measures the angular variations in the intensity of light scattered off of the particles that have been dispersed in water. The angular variations are used to calculate the size distribution of the dispersed material. The system can measure particle sizes in the range of 500 nm to 2000 μm. For this work, a dispersion of water and boron carbide was made with approximately 1.0 vol. % of solids. An ultrasonic horn was used to ensure proper dispersion and deagglomeration.

3.1.3.4 Scanning Electron Microscopy

Particle size was also analyzed using a Zeiss Sigma Field Emission Scanning Electron microscope. Due to the possibility of particle agglomeration during synthesis, the DLS method described previously may not accurately assess primary particle size. To ensure that the primary particle size was known, SEM analysis was required. Powders were placed on an aluminum SEM stub covered in carbon tape. Excess powder was blown off with compressed air and the sample was left to adequately dry. Images were taken at 3 kV with an approximate working distance of 6.5 mm (working distance was adjusted for best imaging conditions).

3.2 Objective 2: Processing of High Purity, Fully Dense Boron-Rich Boron Carbide for Chemical and Microstructural Characterization

Objective 2 focused on the processing of dense boron-rich boron carbide by adding varying amounts of amorphous boron to stoichiometric rapid carbothermally reduced boron carbide. Adding excess boron to boron carbide has been studied in the past as stated in section 2.8. Typically, the boron is added to commercial powders and then hot pressed. The starting boron carbide often contains a large amount of free carbon and the morphology is often very heterogeneous and results in a material that is difficult to sinter. Depending on the powder used and the batch used, chemistry can vary making a systematic study of the effect stoichiometry on boron carbide properties very difficult.

Each sample produced for Objective 2 underwent a suite of characterization techniques to determine chemistry and examine the microstructure. These techniques include Archimedes density, x-ray diffraction, carbon determination using combustion analysis, Raman microspectroscopy, electron and optical microscopy.

3.2.1 Spark Plasma Sintering

As explained in section 2.4.2, spark plasma sintering is a pressure assisted sintering technique that has become a common method to sinter boron carbide to near theoretical densities using relatively low temperatures (<2000°C) and dwell times (~5 min). For this work, spark plasma sintering was used to densify all amorphous boron/boron carbide mixtures.

Due to the large amount of variation in particle size, morphology and chemical makeup of commercial boron carbide, preparing multiple samples without microstructural and chemical variations is extremely difficult. By using boron carbide powder synthesized using rapid carbothermal reduction, chemically and microstructurally uniform samples could be prepared. RCR powders contain very low free carbon, have a homogeneous morphology and the process can be repeated with consistent results.

A systematic study looking at the structure and mechanical properties of boron-rich boron carbide made using spark plasma sintering was done. Samples in the range of approximately 12 to 20 at.% C were analyzed for this work.

3.2.1.1 Powder Mixing

To determine the weight percent amorphous boron needed to alter the boron carbide chemistry to achieve each specific carbon concentration two equations were used. Using the boron to carbon ratio (wt.%), the following equation was,

$$[Boron\ to\ carbon\ ratio\ *\ total\ carbon\ in\ boron\ carbide(wt.\%)] - total\ boron\ in\ boron\ carbide\ (wt.\%) = total\ boron\ needed\ per\ 100\ g\ of\ boron\ carbide \quad (15)$$

The total carbon and boron were determined by chemical analysis of the starting powder. Dividing the total boron needed by 100 and multiplying by the amount of boron carbide being used, the amount of amorphous boron needed to make the desired stoichiometry was determined. This calculation assumes that the amorphous boron preferentially reacts with any free carbon in the sample to form B_4C. Therefore, if any free carbon was present the following term must be added to the total boron needed,

$$\begin{gathered} total\ free\ carbon\ (wt.\%) * 3.6 \\ = \\ total\ boron\ needed\ to\ eliminate\ free\ carbon\ per\ 100\ g\ of\ boron\ carbide \end{gathered} \quad (16)$$

Each boron carbide/amorphous boron mixture was made in four-gram batche to ensure that all powder fits in SPS dies. Mixtures were mixed in a zirconia jar using a high energy ball mill (SPEX 8000M) for 1 min. Mixtures were inserted into a graphite SPS die which was lined with graphite foil to protect from reactions between the die and the powders.

3.2.1.2 SPS Cycle

The optimal SPS cycle for full densification of boron carbide was determined by Toksoy.[7] The following cycle was used to densify all mixtures discussed in the previous section:

1. Die was loaded into specimen chamber and a pre-pressure of 5 MPa was applied
2. Chamber was evacuated to high vacuum
3. Sintering program was started, 10 MPa pressure was applied and temperature was ramped to 600°C
4. 1-minute hold at 600°C to allow system to equilibrate
5. Pressure was ramped to 50 MPa at 10 MPa/sec, temperature was ramped to 1900°C at 300°C/sec
6. 5-minute hold at 1900°C
7. Cool down

Each complete cycle took approximately 1 hour. The four-gram mixture yields a dense sample with a dimension of approximately 20 mm in diameter and 4-5 mm thick. The outer surfaces of the sample were covered in graphite foil which must be removed.

3.2.1.3 Post Processing of Dense Samples

Certain characterization techniques call for varying amounts of processing of the dense samples. Each sample required sandblasting upon removal from the SPS die due to a layer of graphite foil that remains from the sintering process. Along with the graphite foil contamination on the surfaces, a small carbon-rich layer may be present due to

reactions with the graphite foil and graphite dies. To remove this carbon-rich layer, both faces of the sample were surface ground down approximately 100 μm. Both the graphite foil and the carbon-rich surfaces can be detrimental to chemical analysis results therefore proper removal was vital. Surface grinding also ensures that the surfaces are both smooth and flat which was required for high-quality x-ray diffraction. The last step in the post-processing was cutting, mounting and polishing. Samples were cut using a LECO Vari/Cut 50 diamond saw. Depending on the sample preparation requirements for characterization, varying amounts of cuts were made. The cut samples were mounted using a Buehler SimpliMet 1000 mounting press with Buehler ProbeMet thermosetting resin that is safe for polishing and electron microscopy. Mounted samples were then polished using a Buehler AutoMet 250 polisher with a variety of embedded diamond polishing mats and diamond suspensions down to 0.05 μm. If further polishing was required, a Buehler VibroMet 2000 can be used with 0.02 μm colloidal silica.

3.2.4 Characterization

Each dense sample underwent the following suite of characterization techniques to determine chemistry and analyze the microstructure.

3.2.4.1 Archimedes Density

ASTM standard B962-08 was followed for all density measurement of dense boron-rich carbide samples. The density apparatus used is shown in Figure 27. Each clean sample was weighed ten times dry and ten times suspended in the water bath. The equation used to determine that density is,

$$\rho = \frac{dry\ weight}{dry\ weight - suspended\ weight} \tag{17}$$

The average of all the weights was used in the above equation. These values were compared to theoretical densities from Equation 1 in Section 2.2. The percent theoretical density was calculated using the following equation,

$$100 * \frac{\rho}{\rho_t} = \%\ theoretical \tag{18}$$

where ρ is the measured density and ρ_t is the calculated theoretical density.

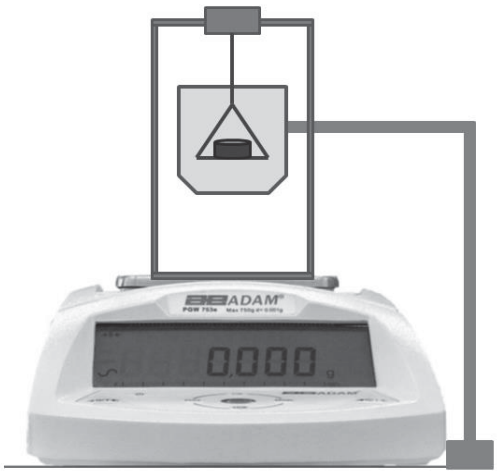

Figure 27. Archimedes density set-up.

3.2.4.3 X-ray Diffraction

The method for x-ray diffraction has been discussed previously in section 3.1.3.1 and was not changed for analyzing dense samples. Similar phase analysis and Rietveld refinement were carried out. Dense samples were cut in five pieces and each cross-sectional face was analyzed. For dense samples, the peak shifts present in the (104) and (021) peaks of the diffraction pattern were important. As the boron content increases, these peaks shifted to lower 2θ indicating an increase in the *a* and *c* lattice parameters. Using Rietveld refinement to determine these lattice parameters, an estimate of the stoichiometry

could be obtained from data reported by Aselage (Figure 4). While the accuracy of the Rietveld refinement is very high, the fitting had a high degree of inherent error. Therefore, further chemical analysis was needed to determine exact chemistry.

3.2.4.4 Chemical Analysis (LECO C/S and O/N)

The method for chemical analysis using LECO C/S has been described in section 3.1.3.2. To ensure the samples sizes are of proper weights, the dense samples are crushed using a diamond coated steel mortar and pestle. After crushing, the crushed material was washed and analyzed.

3.2.4.5 Raman Microspectroscopy

Raman microspectroscopy was used to determine the existence of boron-rich phases as well as the homogeneity of the chemistry across the dense samples. This work was done on a Renishaw InVia Raman microspectrometer equipped with a 633 nm laser and 5x, 20x, 50x and 100x objective lenses. The 480 cm^{-1} and 530 cm^{-1} boron carbide Raman bands are sensitive to the carbon content of the boron carbide. By taking point measurements of the pristine surfaces and line scans of the etched samples, it was possible to gain a qualitative insight into the chemistry changes and homogeneity of each sample. Further, the peaks at 1080 cm^{-1} and 370 cm^{-1} were examined for shifts as this gives an indication as to where the atomic substitution are taking place. For each point scan measurement 5, 10 sec acquisitions were made to ensure proper signal to noise ratio. Line scans were done in three random locations on the sample. Total lengths on the line scan vary, however, step sizes were 1 μm for samples 100BC through 65BC-35B and 2μm for samples 60BC-40B and 55BC-45B. Curve fitting was carried out using the Renishaw WiRE 4.2 software which employs the Levenberg-Marquadt algorithm.

3.2.4.6 Digital Optical Microscopy

A Keyence VHX-5000 Digital Microscope equipped with a Z500 500-5000x variable zoom lens was used to analyze the microstructure of the boron carbide samples. Porosity was the main area of interest examined using this method. Image thresholding was utilized to determine the total pores, average pore size and total percent porosity. To ensure statistically significant results, 5 high dynamic range (HDR) images at 1000x magnification were taken resulting in ~412,000 μm^2 of analyzed area. HDR images were used to allow for manipulations in texture and contrast leading to better thresholding results. Figure 28 shows the steps taken to obtain values for total pores, average pore size, and total percent porosity.

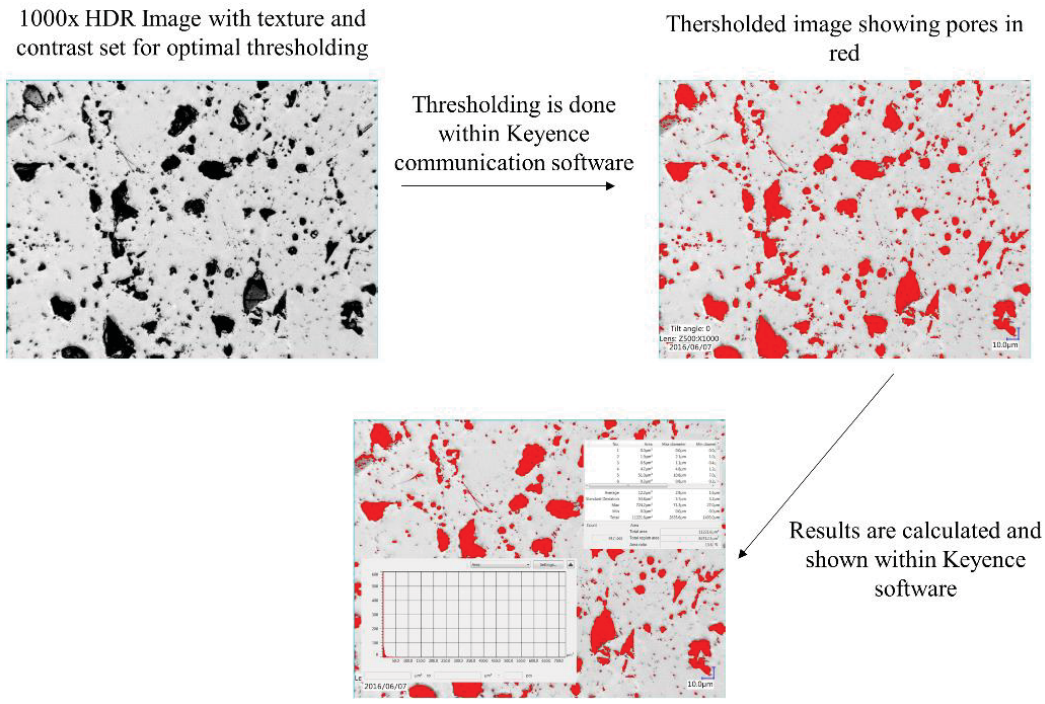

Figure 28. The method for porosity measurements using Keyence VHX-5000.

3.2.4.7 Scanning Electron Microscopy

SEM was used to examine the dense microstructures. Imaging was done using accelerating voltages of 3 kV or below. Areas of interests included grain size, morphology, porosity, and impurity inclusions. Grain size was determined using Lince software (linear intercepts method).

3.2.4.8 Transmission Electron Microscopy

A Phillips CM420 transmission electron microscope was used for grain structure and impurity analysis. TEM samples were thinned to electron transparency using an ion mill. Samples were examined in detail focusing on grain and twin structure and the presence of impurities in grain boundaries and triple junctions.

3.3 Objective 3: Characterization of Static Mechanical Properties of High Purity, Fully Dense Boron-Rich Boron Carbide

3.3.1 Knoop Micro-Hardness

The micro-hardness of each dense boron-rich sample was determined using a LECO M-400-G3 microhardness tester equipped with a Knoop indenter. Knoop indentation is used commonly in advanced ceramics to eliminate the effects of cracking at indent tips. Eliminating cracking allows for more indents to be counted, increasing the accuracy of the measured hardness. Along with the boron-rich samples, Knoop microhardness was done on pure RCR boron carbide samples as well. The values of the Knoop microhardness, as well as the indentation size effect, were evaluated and compared for all boron carbide samples.

The LECO M-400-G3 hardness tester is equipped with two lenses, 10x and a 60x, which were used for alignment of indents on the polished boron carbide surfaces. Loads of 100, 200, 500 and 1000 g were applied and the resulting indent length was measured using ConfiDent software. A series of 12 indents were made to ensure that there was a statistically significant amount of indents to calculate accurate hardness value. The Knoop hardness value was calculated using the following equation,

$$HK\ (GPa) = 0.014229\left(\frac{P}{d^2}\right) \tag{19}$$

where *P* is the load applied, and *d* is the length of the indent. Figure 29 shows the diagonal, d, that were measured for Knoop indentation. Any indents that exhibited excessive cracking or spall as well as indents that were in contact with large pores were eliminated from analysis. Figure 30 shows A) an indent that would be considered an acceptable indent for measuring and B) an indent that would be excluded from measurements. All values reported in the results section are the mean value of all measured indents. For further information on the Knoop hardness measurement refer to ASTM standard C 1326-13.

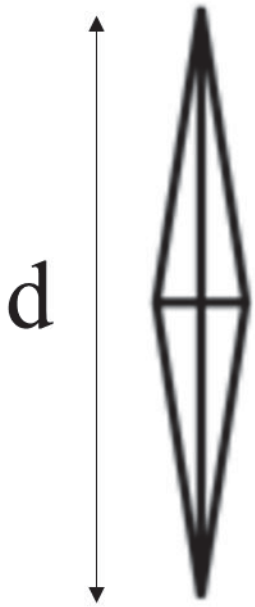

Figure 29. Diagram of Knoop indent showing the diagonal, d, which is measured.

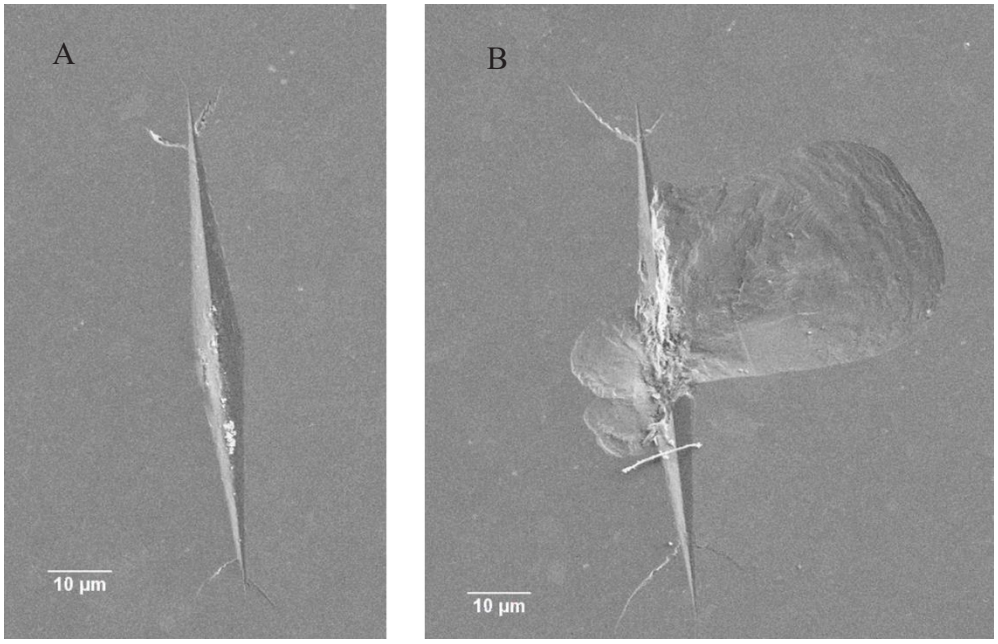

Figure 30. A) An example of a Knoop indent that was used for measurement of hardness. B) An example of a Knoop indent that shows spallation which was excluded from the measurement of hardness.

3.3.2 Berkovich Nano-Hardness

Instrumented nanoindentation was carried out using a MicoMaterials NanoTest Vantage system using a Berkovich indenter. Instrumented indentation allows for the tracking of the load applied to the material as well as the displacement of the indenter in real time. Using this resulting load versus displacement curve, it was possible to determine material properties such as hardness and elastic modulus.

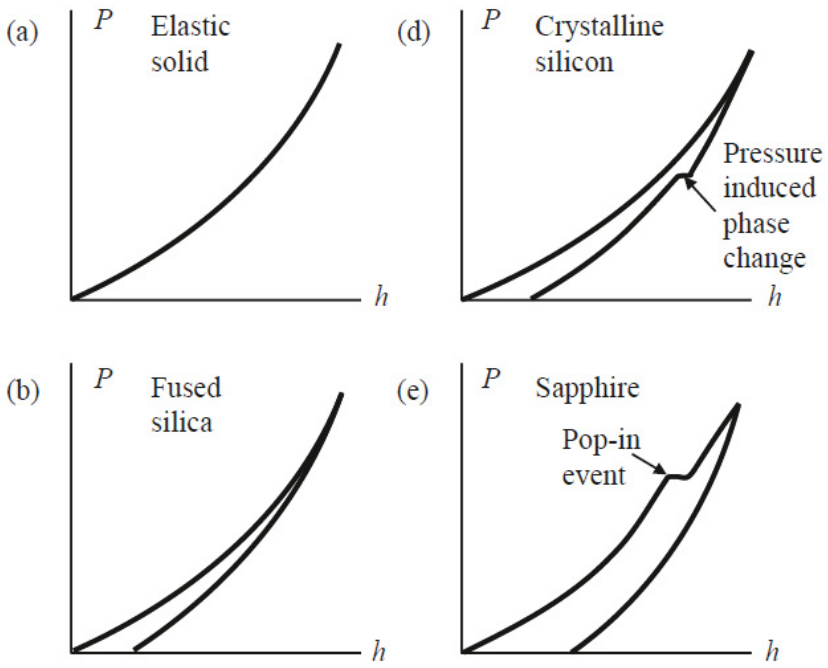

Figure 31. Load-depth curves showing different possible curve characteristics.[74]

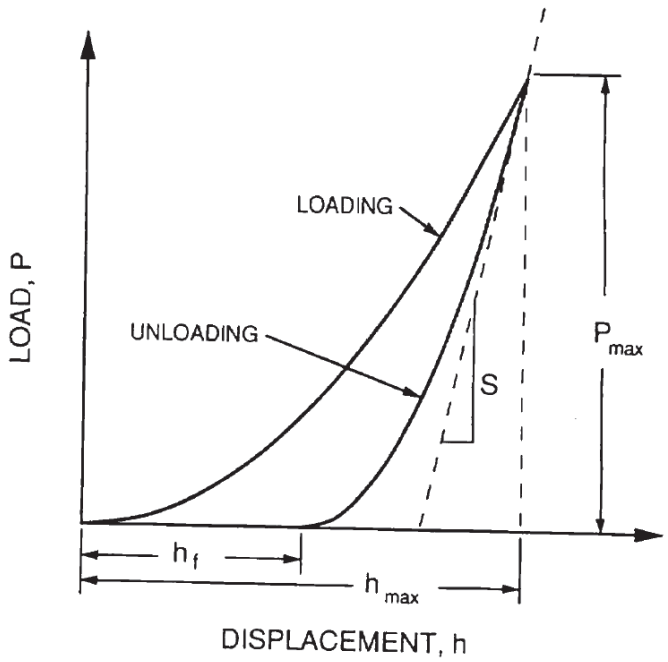

Figure 32. Idealized load v. displacement curves showing critical values that are obtained from the curves.[75]

The loading curve obtained from instrumented indentation contains information such as pop-in events that are typically caused by interactions with defects or due to pressure-induced phase transformations under the indenter (Figure 31). However, the majority of the information obtained from instrumented indentation comes from the unloading curve. Once again pop in events can occur which are evidence of pressure-induced phase transformations. Other information such as the elastic response of the material can be obtained. More importantly, though, values for the contact depth, h_c, and the stiffness, S, can be determined (Figure 32). The stiffness was determined from a simple linear fit of the unloading curve at max load. The contact depth was determined from the following equation,

$$h_c = h_{max} - \epsilon\left(\frac{P_{max}}{S}\right) \tag{20}$$

Where ε is a geometric constant determined by the type of indenter that was being used. For Berkovich indenters, ε = 0.75. With these two values, it was possible to determine the diamond area function (DAF) of the specific indenter that was being used. The DAF was used to find the area of each individual indent as a function of the contact depth. The area was directly used in the calculations of the hardness and the elastic modulus, meaning an accurate DAF was critical for obtaining accurate results. The DAF changes with continued use of the indenter, as the tip of the indenter becomes blunt the shape of low load indents changes. Therefore, the DAF may need to be recalculated multiple times throughout the life of an indenter.

To obtain an accurate DAF, indents in the load range of interest (loads that will make indents of similar size as those made in the material of interest) are made in fused silica. Fused silica was used due to the fact that it is an isotropic, amorphous material with well-known reduced modulus and Poisson's ratio (E_r = 72 GPa and υ = 0.170). Using the built-in software from MicroMaterials, the contact depth and stiffness were calculated for each indent. The area of the indents in the fused silica was determined from the contact depth and the reduced modulus using the following equation,

$$A = \frac{\pi}{4}\left(\frac{1}{E_r^2}\right)S^2 \tag{21}$$

Once the area has been determined for each indent made the data were plotted A vs. h_c and fit using the following equation,

$$A = C_0 h_c^2 + \sum_{n=1}^{8} C_n h_c^{\frac{1}{2^{n-1}}} \tag{22}$$

The fit that was obtained is the DAF and was used to determine the area of all indents made with the particular indenter. MicroMaterials software has this functionality built-in, however, manual validation was carried out.

Once the DAF was obtained, the reduced modulus (and further the Young's modulus) and hardness could be calculated. The reduced modulus was calculated using the following equation,

$$E_r = \frac{\sqrt{\pi}}{2}\left(\frac{S}{\sqrt{A}}\right) \tag{23}$$

And the hardness,

$$H = \frac{P_{max}}{A} \tag{24}$$

Further, the Young's modulus can be determined using the following conversion,

$$\frac{1}{E_r} = \frac{(1-\nu^2)}{E} + \frac{(1-\nu_i^2)}{E_i} \tag{25}$$

Where E_i and ν_i are the modulus and Poisson's ratio for the diamond indenter (E_i = 1141 GPa and ν_i = 0.07) and E and ν are the Young's modulus and Poisson's ratio of the material of interest. Values for the Young's modulus and Poisson's ratio of the diamond indenter were obtained from MicroMaterials.

Two different indentation experiments were carried out for this work. The first was done on the pristine polished surface of the boron carbide samples. For this experiment, an array of indents was made ranging from 100 mN up to 500 mN (100, 200, 300, 400, 500 mN) with 20 indents made at each load totaling 100 indents per sample. The load vs. displacement curves were analyzed for irregularities in the loading curve that may have been due to an interaction with a surface or subsurface pore. Indents that showed irregularities were not included in the final analysis. Using the MicroMaterials software,

the hardness and reduced modulus was obtained for each indent and the mean of the values is reported in the results section. The results were also calculated manually to ensure that the DAF, stiffness, and contact depths were calculated correctly. Further, the 500 mN indents were imaged using SEM and measured using ImageJ software. The area of the indent was determined by measuring the area of a triangle with the exact vertices of the indent. The values for measured hardness were compared to those calculated using the DAF. Fracture toughness was also measured from the 500 mN indents. The fracture toughness of each indent was determined using the following equation,[60]

$$K_c = x_v \frac{\left(\frac{a}{l}\right)^{\frac{1}{2}} \left(\frac{E}{H}\right)^{\frac{2}{3}} P}{c^{\frac{3}{2}}} \tag{26}$$

Where a is the distance from the crack tip to the vertex of the triangle, l is the distance from the vertex of the triangle to the center of the triangle, c is the total crack length, E and H are the Young's modulus and hardness and P is the max load. The value for x_v was determined to be 0.016 by Ouchterlony.[76]

The second set of indentation experiments were done on etched samples. Etching the samples helped in determining whether the indent was fully in a grain or if it intersected grain boundaries or pores. It is important for this thesis to determine the effects chemistry has on the mechanical properties so the elimination of as many possible influences is vital. Therefore, 50, 100 mN indents were made in a grid with 30 μm spacing. The indentation grid was then imaged using SEM and indents that fell fully in individual grains were analyzed. The values obtained from this experiment are compared to the values obtained from the 100 mN indents on the pristine surface.

3.3.4 Ultrasound Non-Destructive Analysis of Elastic Properties

Non-destructive ultrasound was used to measure ultrasonic velocities which allows for the calculation of the elastic properties of the dense boron carbide. For this analysis, a pulse echo, immersion based system was used. This system uses one transducer which both emits and receives the ultrasound energy. Both the transducer and the sample are submerged in water where point measurements were made. An Olympus v316 20 MHz central frequency transducer was used for all measurements.

The transducer measured the velocities of two different ultrasound waves, the longitudinal and transverse waves. Once these velocities were measured, Poisson's ratio, Young's modulus, bulk modulus and shear modulus can be calculated using the following equations,

Poisson's Ratio:

$$\nu = \frac{\left[1 - 2\left(\frac{v_s}{v_l}\right)^2\right]}{2}\left[1 - \left(\frac{v_s}{v_l}\right)^2\right] \tag{27}$$

Young's Modulus:

$$E = \frac{[\rho v_l^2(1-2\nu)(1+\nu)]}{\left[\frac{1-\nu}{1000000}\right]} \tag{28}$$

Bulk Modulus:

$$K = \frac{E}{[3(1-2\nu)]} \tag{29}$$

Shear Modulus:

$$G = \frac{E}{[2(1+\nu)]} \tag{30}$$

3.3.5 Raman Analysis of Knoop Indents

Raman spectroscopy has been discussed in detail in section 3.2. For this work, Raman spectroscopy was used to analyze the amorphization that occurs under the indenter tip. Amorphization has been shown to occur in micro and nano-indents as has been discussed previously. The same Raman setup was used for this work as was discussed in section 3.2. Amorphous peaks appear at higher wavenumbers as compared to the prominent boron carbide peaks. These amorphous peaks are seen at 1330 cm^{-1} and 1810 cm^{-1}, with the more prominent of the two being the low wave number peak. Point scans and maps were employed for this study with an analysis window ranging from 1000 cm^{-1} to 2000 cm^{-1}. Maps were taken using 1 μm step sizes. Once again, 5, 10-second accumulations were used to ensure proper signal to noise. Analysis and curve fitting were done using Renishaw WiRE 4.2 software.

4. Results and Discussion

4.1 Objective 1 Results

Due to the size and temperature limitations of the RCR reactor, boron carbide was synthesized in small sub-batches that were combined to make two master batches. Each sub-batch was analyzed to ensure homogeneity before mixing. The following results are those of the master batches only, as it was found that the sub-batches were homogenous. Refer to section 3.1.2 for details on synthesis parameters.

4.1.1 Boron Carbide Precursor

Multiple batches of boron carbide precursor were made for this work. For boron carbide master batch 1 the following raw materials were used for the precursor:

Total Boric Acid	350 g in 900 ml of H_2O
Total Carbon Lamp Black	79 g in 600 ml H_2O with 2 ml of Triton X-100
% Excess Boron Oxide	50%
Total Precursor After Calcination	276 g (64% of starting material)
Possible Boron Carbide from Precursor	52 g

For boron carbide master batch 2:

Total Boric Acid	800 g in 4200 ml H_2O
Total Carbon Lamp Black	181 g in 1300 ml H_2O with 8 ml of Triton X-100
% Excess Boron Oxide	50 %
Total Precursor after Calcination	632 g (64 % of starting material)
Possible Boron Carbide from Precursor	119 g

It should be noted that during the crushing process there was often a large loss of precursor due to over crushing (fines). Therefore, the possible boron carbide from a single batch of precursor is much lower than calculated. Calcined precursor batches were split into smaller batches (50 – 90 g) and ran through the rapid carbothermal reactor described in section 3.1.

4.1.2 Rapid Carbothermal Reduction

Boron carbide precursor was reacted in RCR reactor in a total of six runs. While the total batch size varied from run to run, furnace parameters were kept constant. The precursor was fed into the system at approximately 2 g/min entrained in an argon flow. Run times varied depending upon the size of the batches and are reported below. Boron carbide master batch 1 was made in two separate furnace runs,

Table 3. Master batch 1 reaction parameters.

	Run 1	Run 2	Total
Amount of Precursor (g)	50	50	100
Reaction Temp (°C)	1850	1850	1850
Reaction Time (min)	---	---	---
Expected Boron Carbide (g)	9.4	9.4	18.8
Actual Yield (g)	8.0	9.0	17.0
Efficiency (%)	85.1	95.7	90.4

The four other runs make up boron carbide master batch 2,

Table 4. Master batch 2 reaction parameters.

	Run 1	Run 2	Run 3	Run 4	Total
Amount of Precursor (g)	59	80	90	61	290
Reaction Temp (°C)	1850	1850	1850	1850	1850
Reaction Time (min)	23	40	49	30	---
Expected Boron Carbide (g)	11.0	15.0	16.9	11.5	54.4
Actual Yield (g)	9.2	10.4	13.8	10	43.4
Efficiency (%)	83.7	69.3	81.7	87.0	79.8

Each of these individual runs was mixed together as it was determined that they were similar in chemistry and powder morphology. The following results describe characterization done on the master batches. It should be noted that the expected yields versus the actual yields for each master batch vary from 90.4 % and 79.8 % respectively. This deviation from the expected can be explained by the loss of precursor due to clogging which caused some precursor to never enter the reactor, as well as powder lost due to it missing the crucible as it fell.

4.1.3 X-Ray Diffraction

Primary and secondary phase identification of synthesized boron carbide powders were done using x-ray diffraction. Boron carbide has many identifiable diffraction peaks with the two highest intensity peaks, (104) and (021), located at 35 and 37.8° 2θ respectively. Figures 33 and 34 show the powder diffraction pattern of the two master batches with the boron carbide peaks indicated. Analysis of these patterns shows two unidentified peaks at 26.5° 2θ and 28.4° 2θ. The peak located at 26.5° 2θ is attributed to the small amount of free carbon that is present in the powder. Free carbon is commonly found in boron carbide, however, it is often found in much larger quantities than is present in the two master batches. The carbon peaks present in the boron carbide master batch patterns correspond to approximately 0.2 wt.% free carbon. The second peak present is an artifact of the silicon zero background holder used for the analysis. Metallic phases were not present since no post-processing size reduction was attempted. The elimination of secondary phases in the boron carbide powder is vital since secondary phase inclusions can cause micro-cracking and act as crack initiation sites (Section 2.5.1). These can potentially affect the accuracy of the various measurements that are reported in the following sections. Free carbon has also been reported to act as crack initiation sites however, the free carbon reacts with the added amorphous boron during preparation of boron-rich samples (Section 4.2.6). Therefore, no effect on the measured properties was expected.

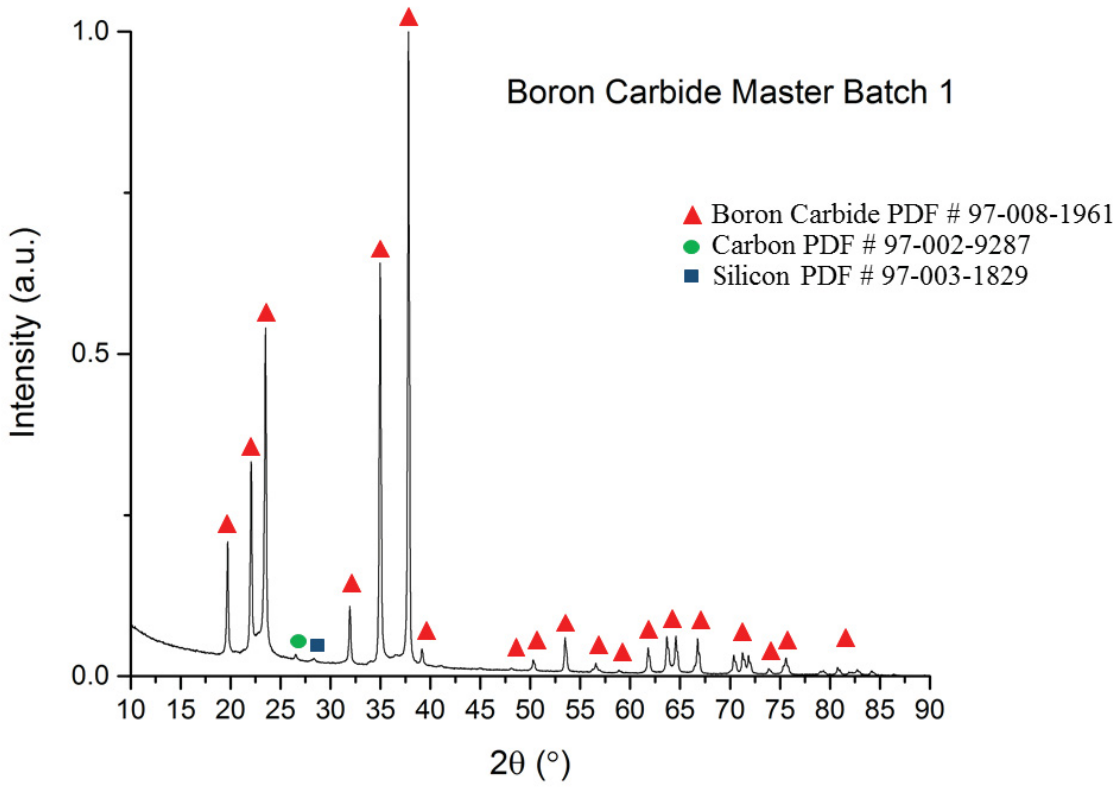

Figure 33. XRD powder diffraction pattern for boron carbide master batch 1. Red triangles indicate boron carbide phase, green circles indicate free carbon phase and blue squares indicate silicon phase (due to single crystal silicon zero background holder).

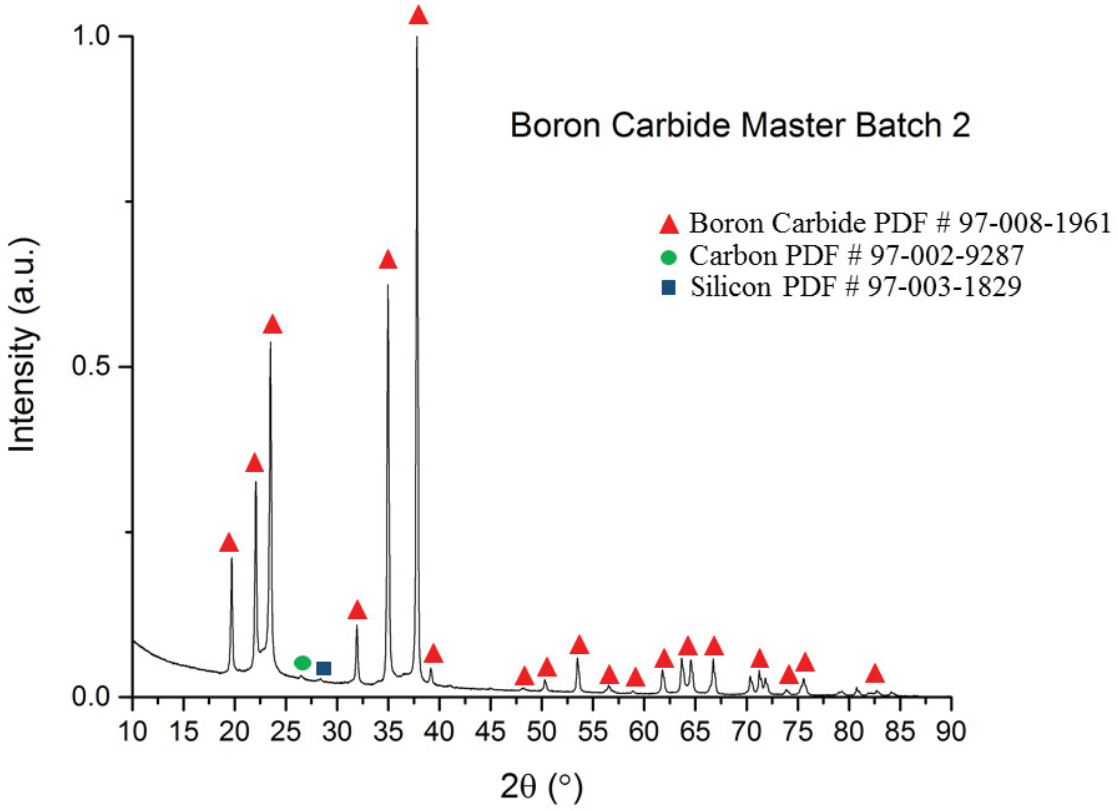

Figure 34. XRD powder diffraction pattern for boron carbide master batch 2. Red triangles indicate boron carbide phase, green circles indicate free carbon phase and blue squares indicate silicon phase (due to single crystal silicon zero background holder).

4.1.4 Chemical Analysis

Chemical analysis was carried out using a suite of different analytical instruments as outlined in section 3.1.4. Total carbon, boron, oxygen and nitrogen contents were measured and the powder stoichiometry was then determined (Table 5).

The chemistry of boron carbide is highly dependent upon the reaction temperature and the amount of excess boron oxide used in the precursor. Reaction temperatures below 2000 °C resulted in powders near the carbon-rich limit of 20 at.% regardless of the amount of excess boron oxide used.[28] The results reported in Table 5 confirmed this, as the reaction temperature used in this study was 1850°C. Oxygen levels were relatively low after an initial wash in a 3.5 pH HCl solution and remained low over time (increase to ~ 0.6 wt.% after two weeks), showing stability in air. The stoichiometry was in line with the expected value of B_4C.

Table 5. Boron carbide master batch 1 and 2 chemistries.

	Master Batch 1	**Master Batch 2**
Boron (at.%)	79.97 ± 3.14	80.11 ± 2.03
Carbon (at.%)	19.57 ± 0.10	19.45 ± 0.44
Oxygen (at.%)	0.28 ± 0.01	0.290 ± 0.001
Nitrogen (at.%)	0.189 ± 0.001	0.150 ± 0.003
Stoichiometry	$B_{4.09}C$	$B_{4.12}C$

4.1.5 Particle Size Analysis

Particle size analysis was carried out using two different methods; dynamic light scattering and scanning electron microscopy. These two methods were used in tandem due to the fact that some particle necking and agglomeration may occur during the synthesis of the boron carbide powders. Dynamic light scattering cannot differentiate between a single primary particle and a large agglomerate, whereas, analysis of SEM micrographs provided

insight into the primary particle size. Table 6 reports the d_{10}, d_{50} and d_{90} for both of the master batches while Figure 35 displays the volume distribution of particle sizes. Analyzing these results, it is apparent a high degree of agglomeration had occurred during synthesis leading to a d_{90} much higher than the expected particle size (<5 μm). In an attempt to eliminate the large agglomerates, a second analysis was done after the dispersion was allowed to settle for 2 hours. According to the sedimentation theory, the two hours would allow for only the larger agglomerates to settle to the bottom while the smaller primary particles would not have sufficient time to settle.[77] The results of this second analysis are once again shown in Table 6 and Figure 35. The nature of agglomeration changed in master batch 1 as the d_{90} value dropped by nearly 5 μm. The nature of agglomeration was largely unchanged for master batch 2 indicating the powder was likely more agglomerated. SEM examination revealed that the agglomerates were made up of primary particles approximately 1 μm in size (Figure 36). The d_{90} was also observed to be more significant in master batch 2, confirming the DLS results. The agglomerates seen in the SEM micrographs are typically between 10 and 20 μm which is also in agreement with the DLS measurements and more specifically the d_{90} measurements. The powder morphology was very homogenous and faceted which is a characteristic of the carbon lampblack that was used as the carbon source for the precursor.[31]

Table 6. Dynamic light scattering particle size of master batch 1 and 2.

	DLS Particle Size (μm)					
	No Settle Time			**2 hr Settle Time**		
	d_{10}	**d_{50}**	**d_{90}**	**d_{10}**	**d_{50}**	**d_{90}**
Master Batch 1	1.54	3.68	8.38	0.72	1.58	3.64
Master Batch 2	1.59	3.99	10.02	1.00	3.17	8.93

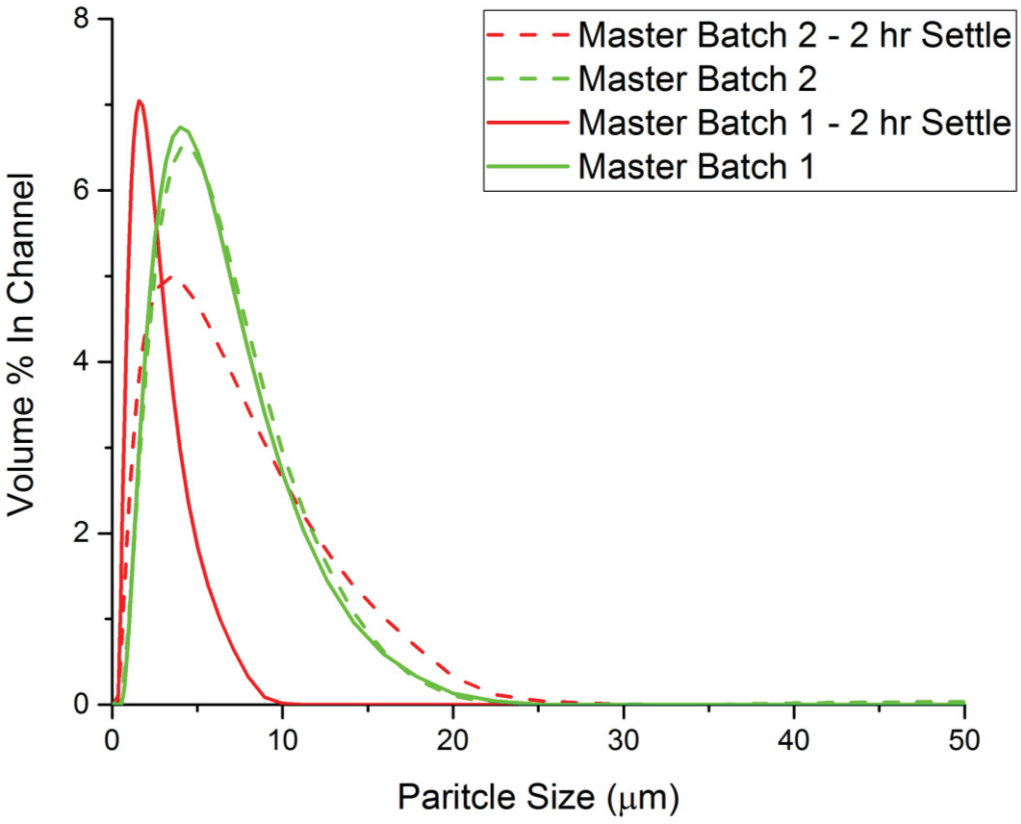

Figure 35. DLS particle size distribution for boron carbide master batch 1 and 2.

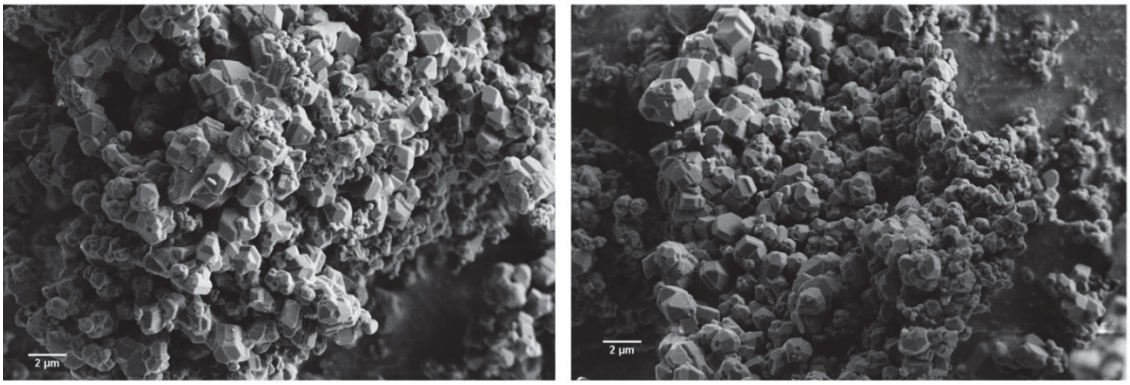

Figure 36. SEM micrographs showing primary particles (~1 µm) agglomerated into larger agglomerates (~10 µm).

4.2 Objective 2 Results

4.2.1 Powder Mixing

Six boron-rich boron carbide samples were processed along with one baseline sample with no amorphous boron additions. The mixing process was outlined in Section 3.2.1. The mixture ratios and expected chemistry are reported in Table 7. Calculations using Equations 15 and 16 took into account the small amount (< 1 wt.%) of free carbon that was present in the starting powder. Each sample was spark plasma sintered at 1900°C for 5 min under uniaxial load of 50 MPa in flowing argon.

Table 7. Sample Inventory with expected boron to carbon ratio calculated using powder chemistry.

Sample	Grams of Boron Carbide (g)	Grams of Amorphous Boron (g)	Expected Boron:Carbon Ratio
55BC-45B	2.21	1.80	8.3
60BC-40B	2.41	1.62	7.5
65BC-35B	2.60	1.40	6.8
75BC-25B	3.00	1.00	5.7
85BC-15B	3.41	0.60	4.9
95BC-5B	3.81	0.20	4.3
100BC	4.00	0.00	4.1

4.2.2 Density

The density of the sintered samples was measured using the Archimedes method. Each sample was weighed ten times dry and ten times wet. The theoretical density of boron carbide was determined using Equation 1. The experimental and theoretical densities are shown in Table 8. Examining the density data suggests that the added amorphous boron aids in sintering up to a limit 35 wt.% B. This is due to the amorphous boron additions reacting with the lower density graphite phase, eliminating any inclusions that may have potentially formed. Upon further boron additions, the percent theoretical density dropped. The reason for the observed drop in density will be discussed later.

Table 8. Archimedes density and % theoretical density based off of Equation 1.

Sample	Density (g/cm^3)	Theoretical Density (g/cm^3)	% Theoretical Density
55BC-45B	2.42	2.47	97.9
60BC-40B	2.44	2.48	98.4
65BC-35B	2.48	2.48	100.0
75BC-25B	2.50	2.50	100.0
85BC-15B	2.50	2.51	99.6
95BC-5B	2.51	2.51	100.0
100BC	2.48	2.52	98.4

4.2.3 Porosity

As has been previously discussed, porosity is an undesirable microstructural feature. Therefore, knowledge of the amount of porosity and characteristics of the porosity is important. This knowledge is especially important when porosity dependent properties are being measured. For this reason, a means of measuring the porosity within the samples is required.

To examine the amount of porosity in each sample, samples cross-sectional face was analyzed using a Keyence VHX-5000 Digital Microscope with a Z500 500-5000x variable lens as described in section 3.2.4.6. Thresholding of the HDR images was carried out using the communication software provided with the microscope. Figures 37 through 43 show the resulting thresholded images taken at 1000x magnification. Each image corresponds to an 82,412 μm^2 of sample area, resulting in ~412,000 μm^2 of total sample area being analyzed for each sample. As was discussed earlier, the highly covalent nature of boron carbide makes achieving 100% theoretically dense samples very difficult. This difficulty is exhibited in sample 100BC. Figure 43 reveals a relatively high amount (2.81%) of porosity dispersed throughout the microstructure. As boron additions are made, the percent porosity begins to decrease, with sample 85BC-15B exhibiting the lowest total porosity of 1.0 %. However, as boron additions are increased above 35 wt. % the total porosity begins to rapidly increase (Figures 37 and 38). Table 9 contains the relevant porosity data that was gathered using the Keyence software. It is seen that the average pore size is typically 2 μm or less but once again rapidly increases to 10+ μm in the highly boron-rich samples. The Archimedes density measurements are accurate for the samples with less than 35 wt. % boron additions but with further additions, density measurements become inaccurate. This is due to one of two things. First, the wet weight of the sample was not measured so any open porosity was not accounted for. Samples 60BC-40B and 55BC-45B have some open porosity so the lack of a wet measurement could throw off the results. The second issue is material pullout during sample prep. Mechanical polishing can cause excess material to be removed. If there was an area that was poorly sintered, a piece of boron carbide could have potentially been removed and, therefore, causing a pore

to form. This would affect the results from the optical imaging but not the Archimedes density once again causing variations in the results.

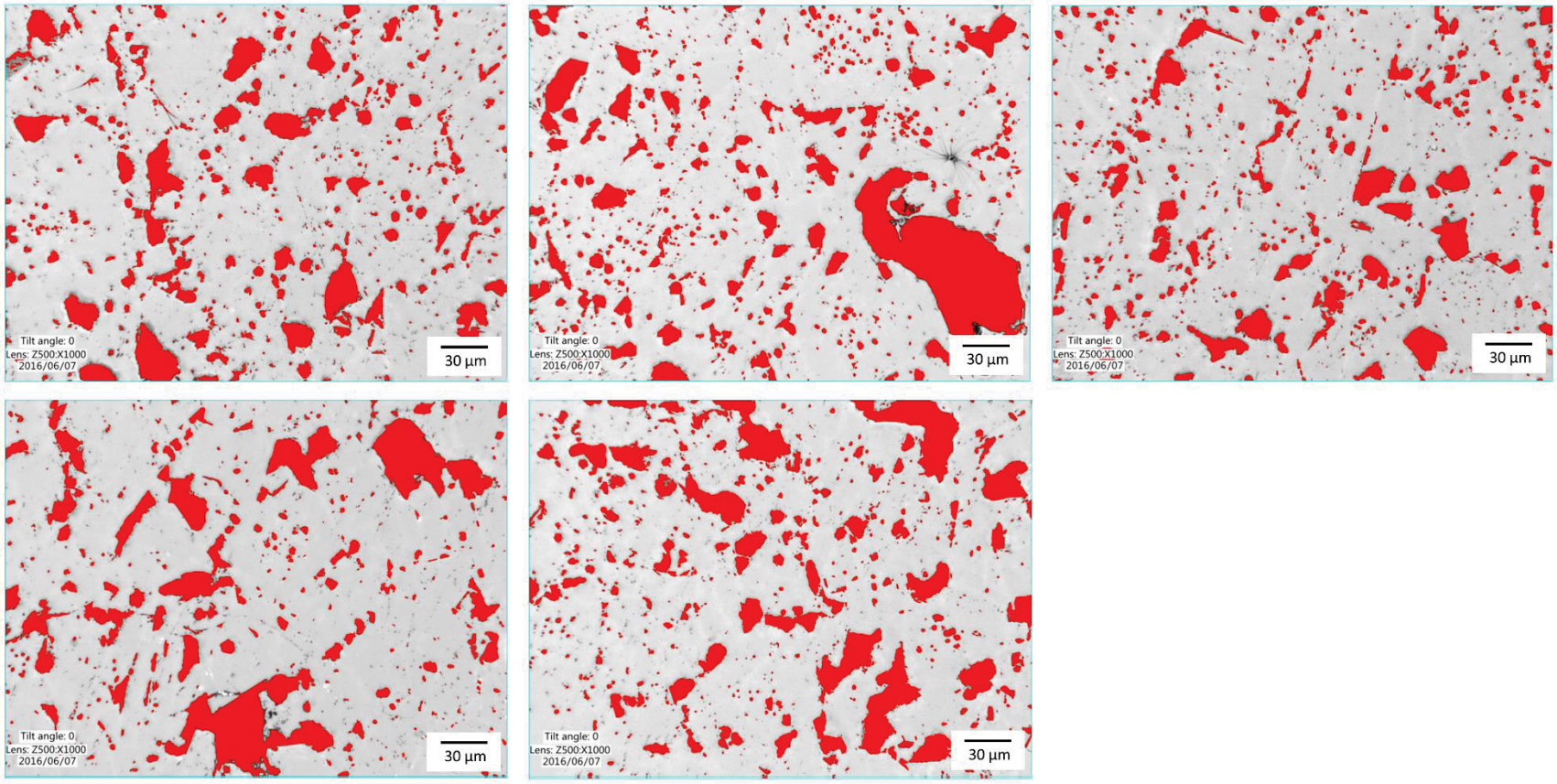

Figure 37. Thresholded optical image of sample 55BC-45B (porosity shown in red).

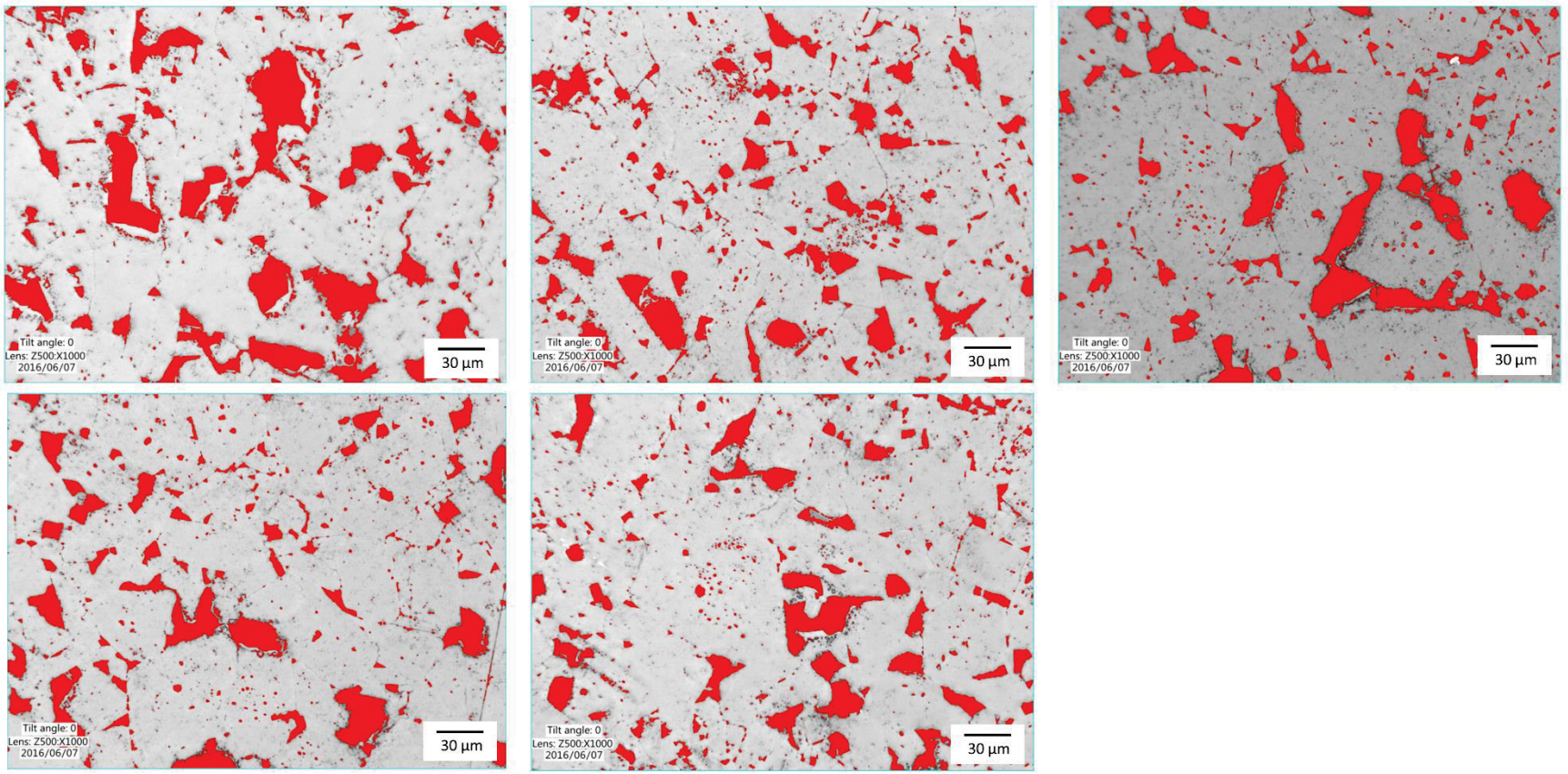

Figure 38. Thresholded optical image of sample 60BC-40B (porosity shown in red).

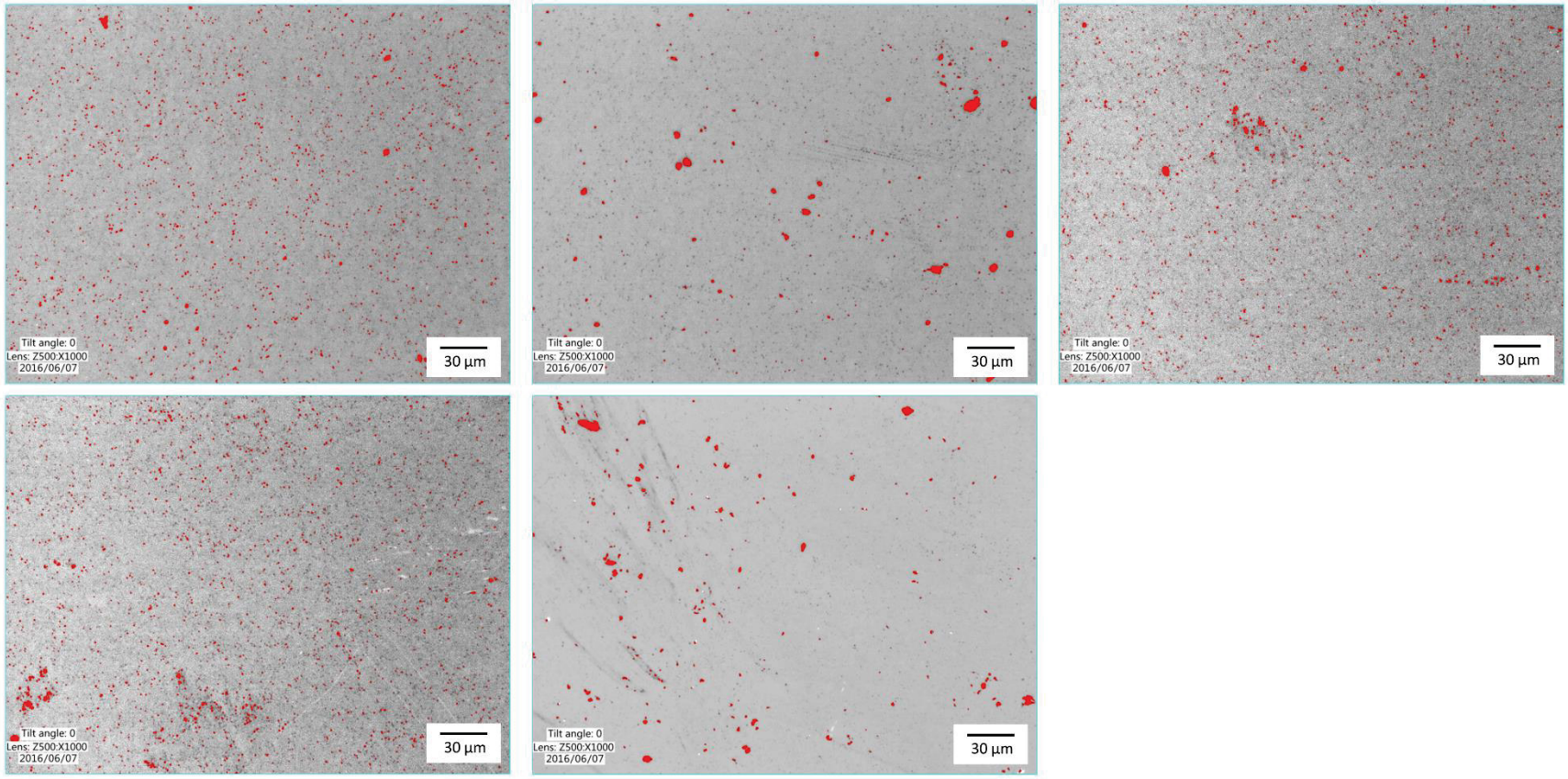

Figure 39. Thresholded optical image of sample 5BC-35B (porosity shown in red).

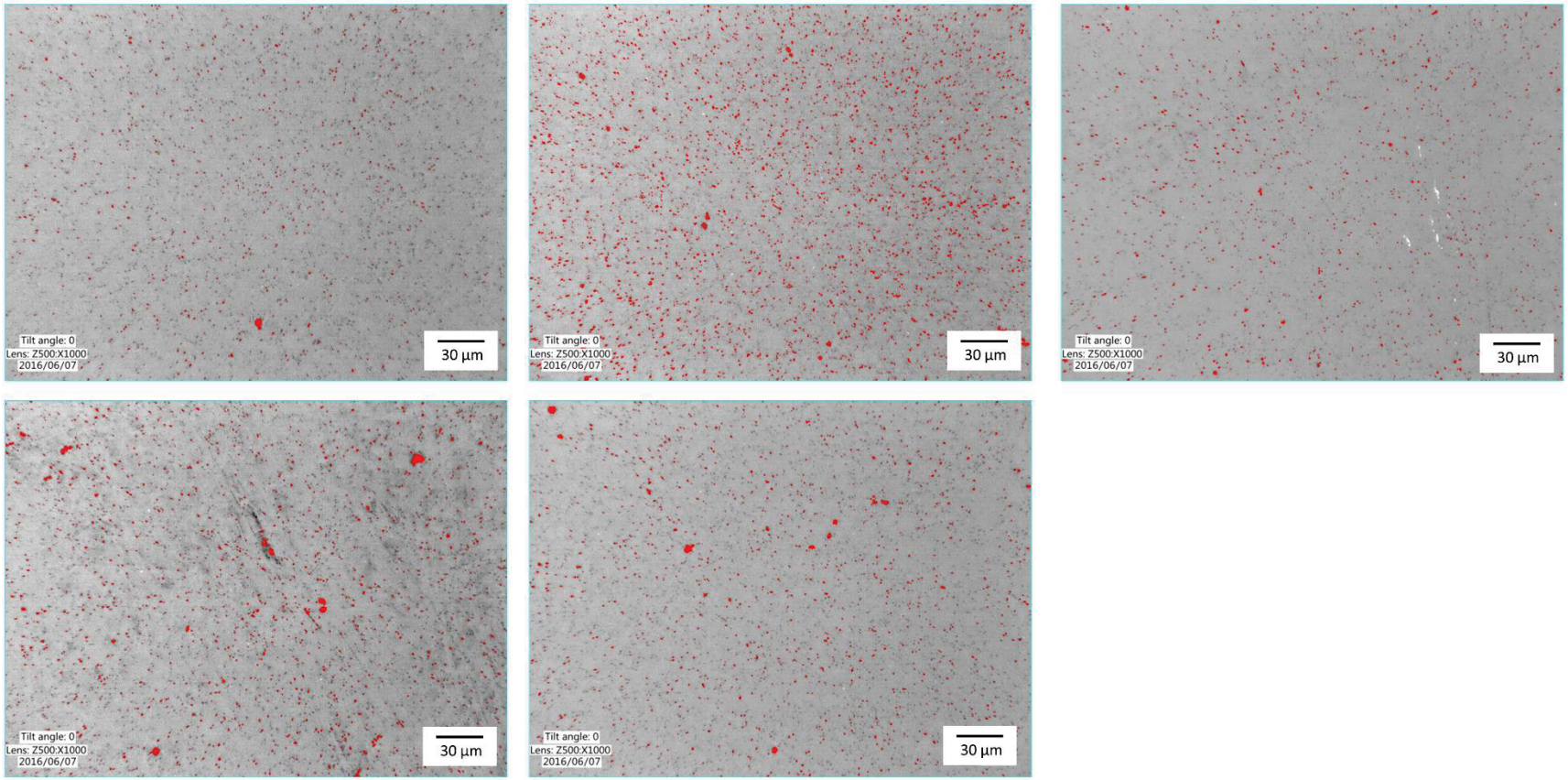

Figure 40. Thresholded optical image of sample 75BC-25B (porosity shown in red).

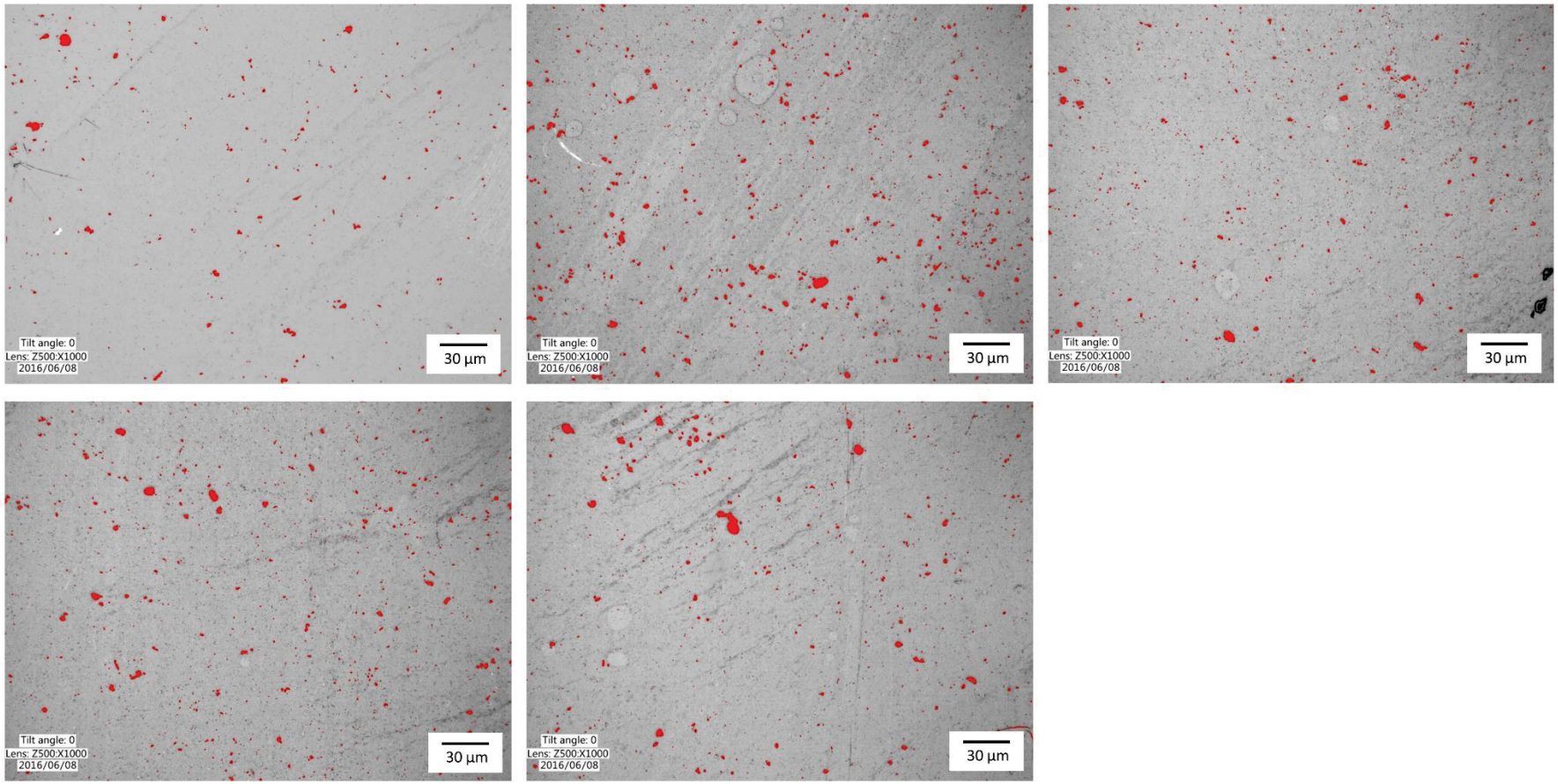

Figure 41. Thresholded optical image of sample 85BC-15B (porosity shown in red).

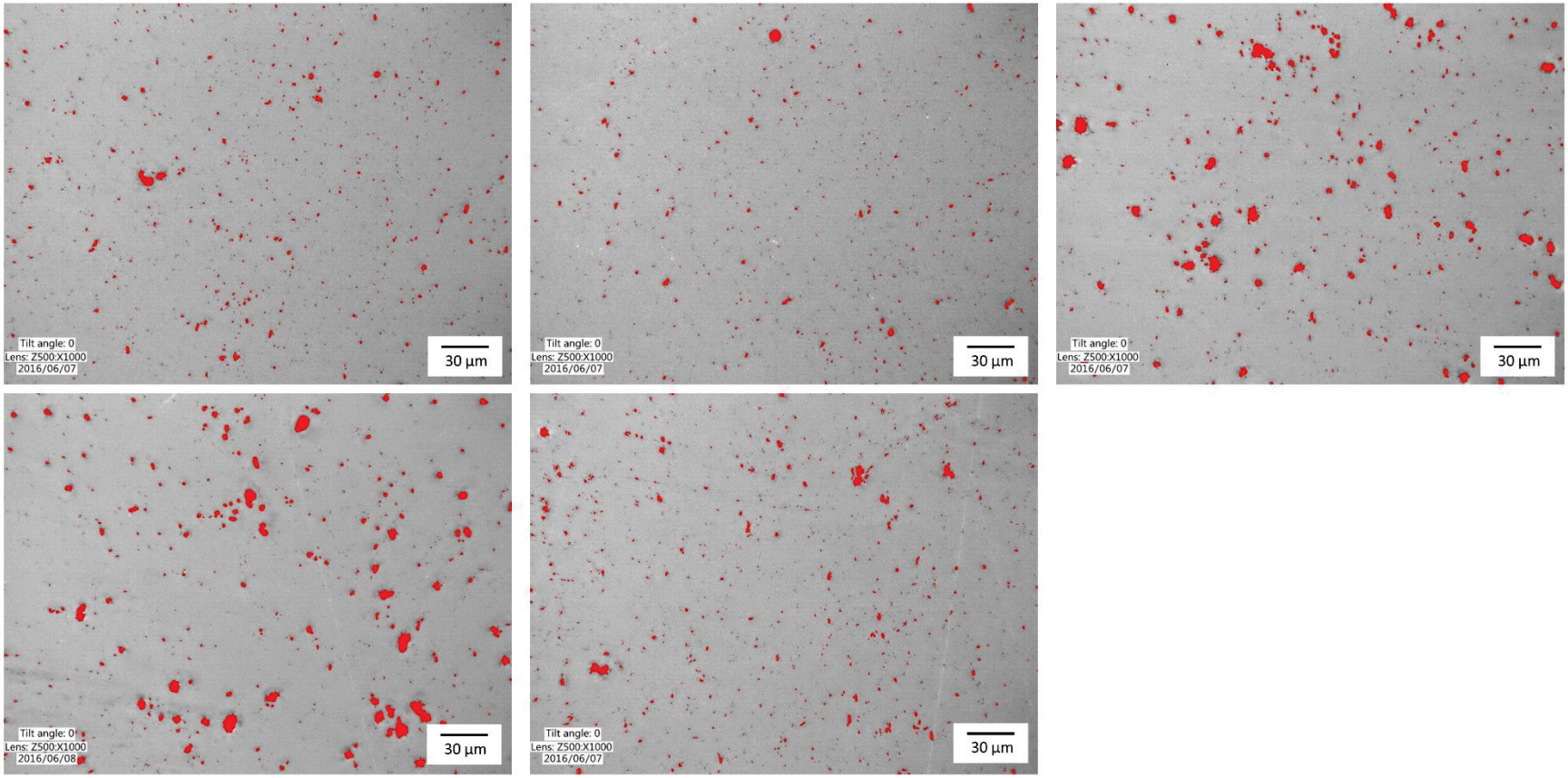

Figure 42. Thresholded optical image of sample 95BC-5B (porosity shown in red).

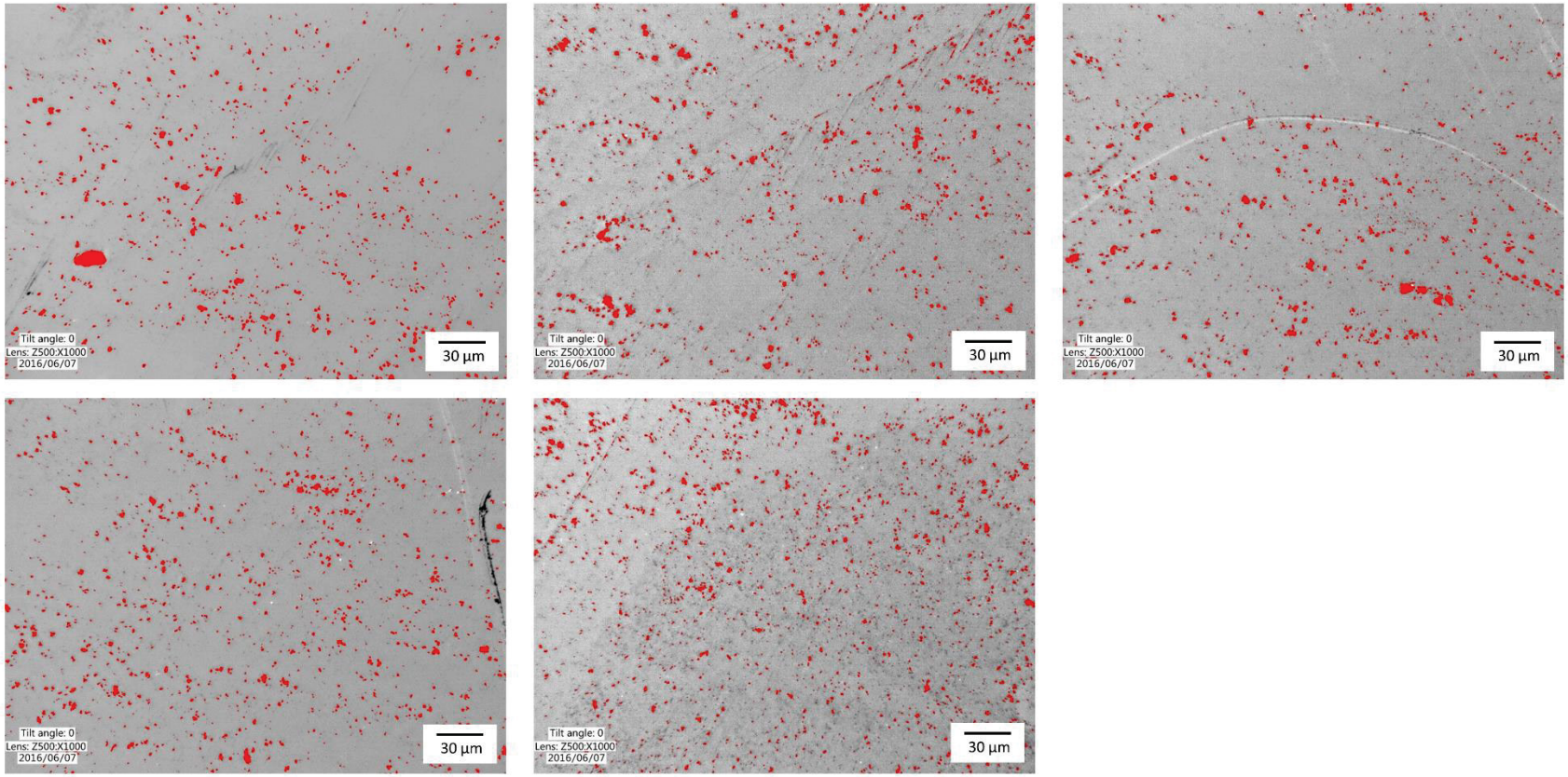

Figure 43. Thresholded optical image of sample 100BC (porosity shown in red).

Table 9. Porosity measurement results.

	55BC-45B	60BC-40B	65BC-35B	75BC-25B	85BC-15B	95BC-5B	100BC
Total Area (µm²)	64291	55129	5040	6028	4082	5644	11595
Total Region Area (µm²)	412061	412061	412061	412061	412061	412061	412061
% Porosity	15.6	13.4	1.2	1.5	1.0	1.4	2.8
Total Pores	4482	5090	16405	21329	4583	3694	12866
Avg. Pore Area (µm²)	14.3	10.8	0.3	0.3	0.9	1.5	0.9

4.2.4 SEM Microstructural Analysis

Grain size analysis was performed on etched boron-rich samples using scanning electron microscopy. Figure 44 shows the etched microstructures of the boron-rich samples. Samples with relatively low boron additions (≤ 35 wt.%) show limited grain growth with a bimodal grain size. Upon increasing the boron additions (> 35 wt.%) the samples exhibit exaggerated grain growth with a more normal grain size distribution. The grain size of each sample is reported in Table 10. This appearance of exaggerated grain growth is an indicator that a liquid phase boron was likely present during the reaction. When examining the kinetics of boron carbide formation, it is well known that growth, as opposed to nucleation, is the dominate factor when there is a liquid-solid reaction.[27] It

would logically follow that the grain growth that is exhibited in the samples is due to a liquid-solid reaction during the sintering process. The results in Table 10 also indicate that the powder agglomeration that was reported in section 4.1.5 does not have much effect on the microstructure of the dense boron carbide. The grain size is significantly smaller than the d_{90} reported from DLS and more in line with the observations of the primary particles seen in the SEM micrographs. This is an important observation due to the fact that mechanical properties begin to diminish as the grain size increases. Hence, keeping the grain size small was a goal of this work. Equally important was keeping the grain size similar for all samples to avoid a significant grain size effect when comparing their mechanical properties. Table 10 once again shows that the differences in grain size was not significant and should not have a large impact on the measured properties (with the exception of sample 55BC-45B and 60BC-40B).

The microstructures were also examined for any inclusions that may have formed due to impurities. The results revealed a homogenous and clean microstructure void of any impurity inclusion including free carbon.

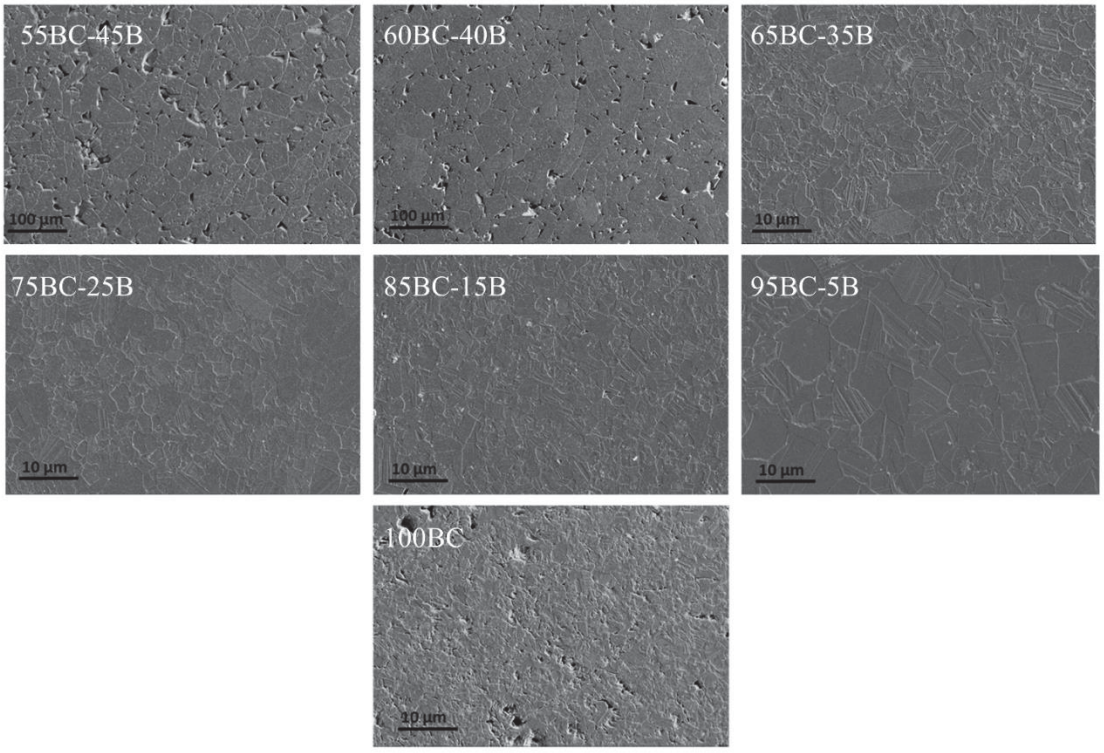

Figure 44. SEM micrographs of etched sample surfaces. Increased porosity and grain size are evident in samples 55BC-45B and 60BC-40B (Increased scale bar to show many grains). Sample 100BC has slightly higher porosity.

Table 10. Grain size results from linear intercepts measurement method.

Sample	Grain Size (µm)
55BC-45B	39.6 ± 7.9
60BC-40B	40.9 ± 3.2
65BC-35B	4.4 ± 0.9
75BC-25B	4.2 ± 1.2
85BC-15B	4.4 ± 0.9
95BC-5B	8.6 ± 1.5
100BC	3.2 ± 0.1

4.2.5 Transmission Electron Microscopy

Transmission electron microscopy (TEM) was used to examine grain structure and the presence of small scale inclusions that may not be seen by other characterization techniques. Samples 60BC-40B and 55BC-45B were not analyzed due to the poor quality

of the samples. Figure 45 displays the typical microstructures that were seen throughout each sample. Conclusions made from the SEM work were further confirmed with the TEM analysis. Samples exhibited a bimodal grain size distribution with a relatively small average grain size (< 5 μm). The microstructures were highly dense with only some very small porosity seen at grain boundaries and triple junctions.

Figure 46 shows high-resolution TEM (HRTEM) images of the grain boundaries of three samples (only three samples were examined due to the difficulty in obtaining quality HRTEM images). These images show that the grain boundaries are free of any secondary phases or intergranular films. These microstructures can be described as "clean". Also, triple junctions in Figure 45 show no visible signs of impurity inclusions. These results suggest that the samples were high purity (>99%). These results confirm the effectiveness of sample preparation techniques from synthesis of the starting powder to the mixing and sintering in avoiding any possible contamination.

One observation that is not clearly seen in the SEM micrographs is the high degree of twinning present in these samples. This is most likely an artifact of the RCR powder as the powders have been shown to contain a high density of nano-twins. However, the characterization work done by Chen[62] and Xie[63] show the near stoichiometric boron carbide contains some degree of inherent twinning. More recent work by Xie has shown that boron-rich boron carbide chemistries also exhibit twinned grains. Therefore, the twinning that is present in the boron-rich boron carbide samples may be an artifact of the reaction during sintering as the materials characterized by Chen and Xie were made from commercial powders with very low twin densities.

Three samples were further examined using high-resolution TEM (HRTEM). Twin density and orientation were of interest. Figure 47 shows that the twin densities are actually changing with the change in chemistry (higher density of twins in 65BC-35B than 85BC-15B and 100BC). This further suggests that the twinning is an artifact of the reaction between the boron and boron carbide during the sintering process. The orientation of twins in boron carbide is well known to occur on the {001} twin plane. It should be expected that the orientation of the twins in the boron-rich samples would occur on this same slip plane. Sample 65BC-35B was chosen for orientation analysis as this is the sample that would most likely exhibit a differing orientation due to the change in the atomic configuration (Figure 48). The results, however, show that the orientation is not affected by the chemistry changes.

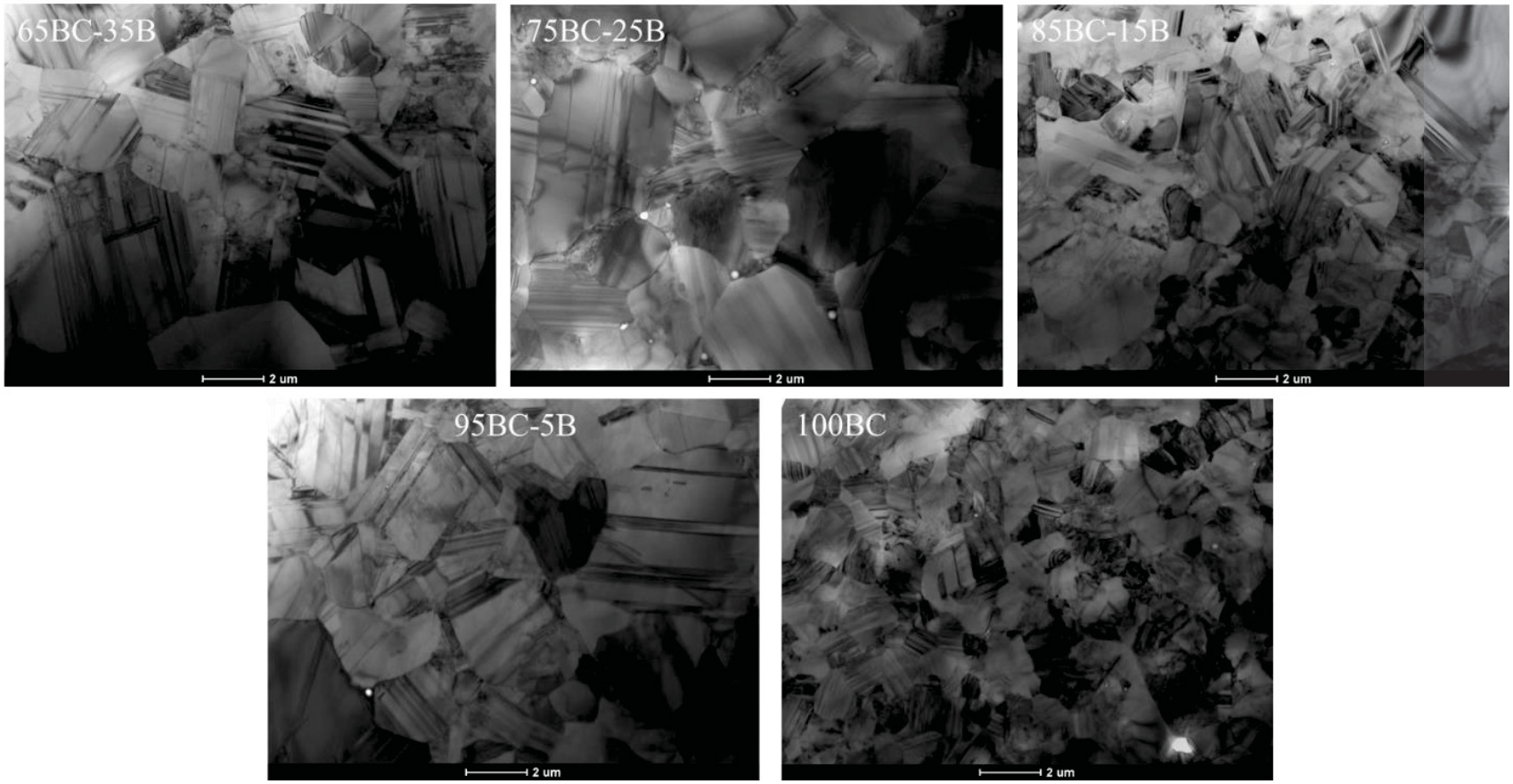

Figure 45. TEM images of the microstructure of samples 65BC-35B through 100BC. Little to no porosity or impurity phases are seen.

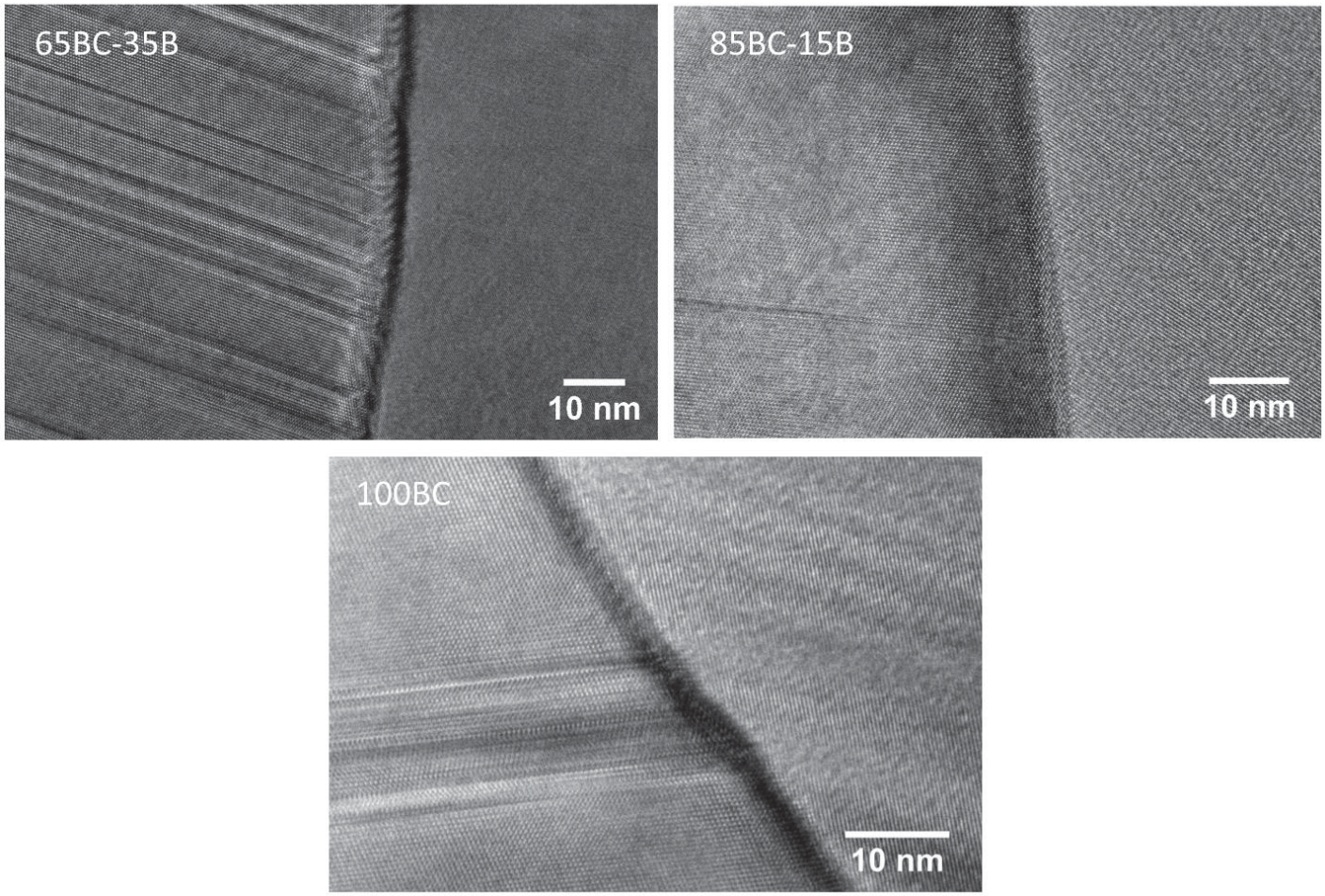

Figure 46. High resolution TEM of grain boundaries of sample 65BC-35B, 85BC-15 and 100BC. No intergranular phases/films are present.

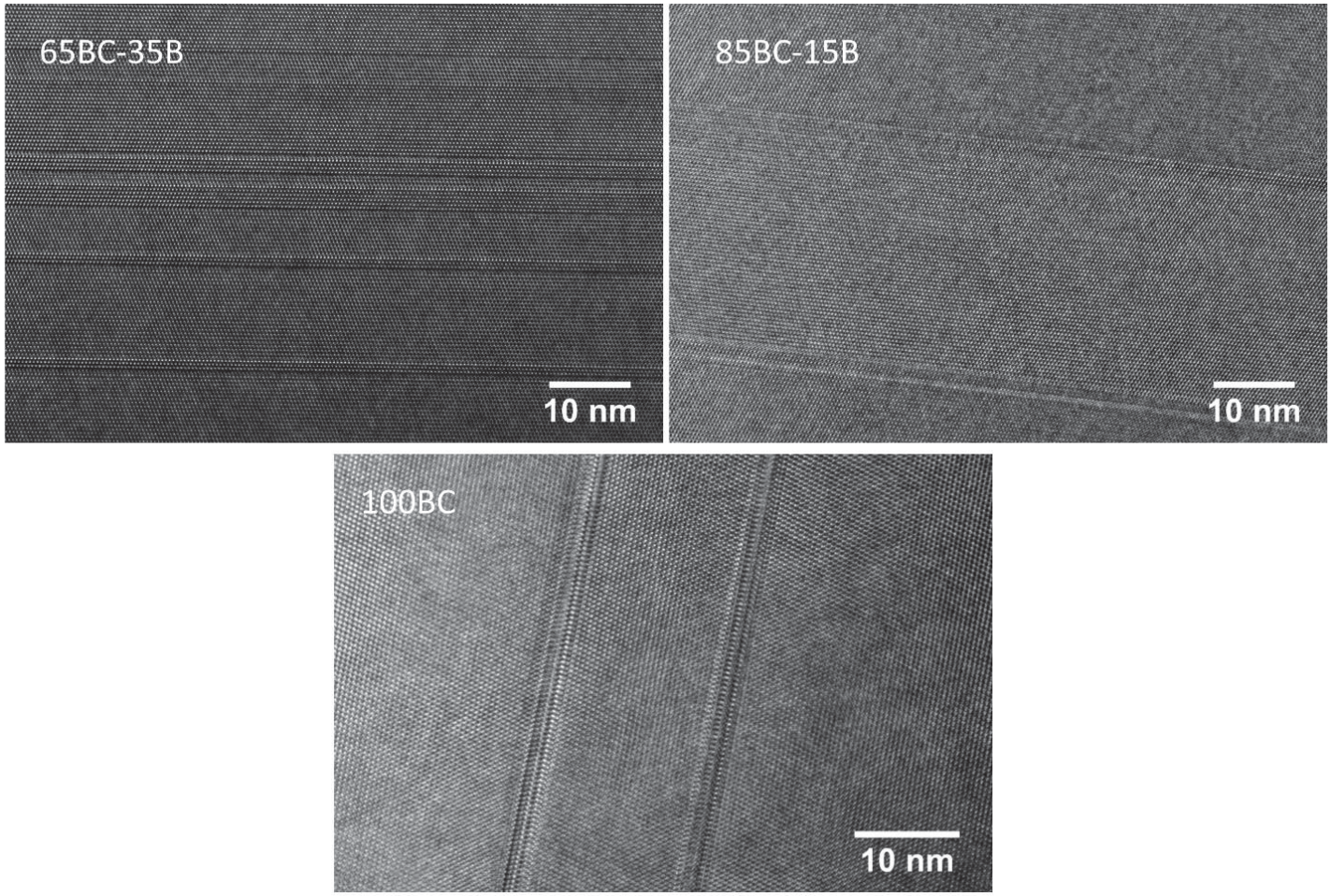

Figure 47. High resolution TEM images of the twin structure present in samples 65BC-35B, 85BC-15B and 100BC.

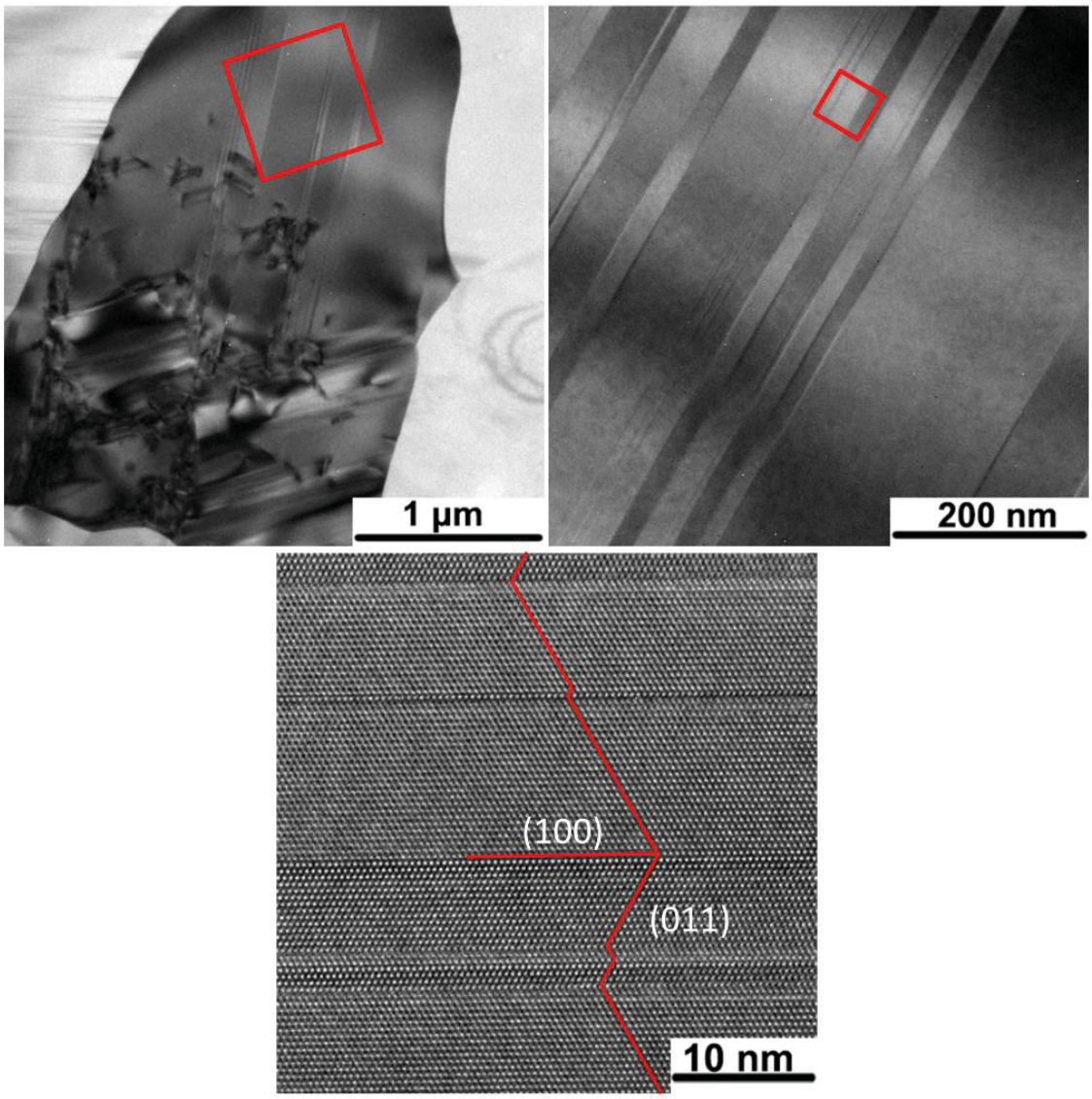

Figure 48. Twin orientation analysis for sample 65BC-35B. Sample 65BC-35B was chosen due to the significant change in chemistry making it the most likely sample to have a differing twin orientation.

4.2.6 X-ray Diffraction

X-ray diffraction analysis was carried out on each cross-sectional face of the cut boron-rich samples as described in section 3.2.4.3. Figure 49 shows the XRD patterns obtained from these analyses. The first major observation is that the boron-rich boron carbide shows no observable free boron or free carbon impurity phases. Figure 50 highlights the area in which the free carbon peak would appear (~26° 2θ), however, the only sample that exhibits a slight feature at this location is 100BC. As stated in the section 4.1.3, the starting powder did contain a small amount of free carbon which explains the appearance of this peak. Free boron would most likely show up as a broad amorphous peak at low 2θ. However, there is no such peak seen in any of the patterns. Some of the other samples exhibit a peak at approximately 29° 2θ which is an artifact of the putty that is used to mount the samples for XRD analysis. The absence of secondary phases in dense samples means that any degrading effects due to potential secondary phase inclusions can be discounted.

A shift in the boron carbide peaks to lower 2θ values as the boron additions are increased is seen in Figure 51. This is due to changes in the boron carbide unit cell lattice parameters. This is to be expected, as carbon is substituted with boron the unit cell volume increases due to the boron atom having a larger atomic radii. While the exact location of the boron substitution in these samples is not known, it becomes clear from the x-ray diffraction patterns that boron/carbon substitutions are occurring.

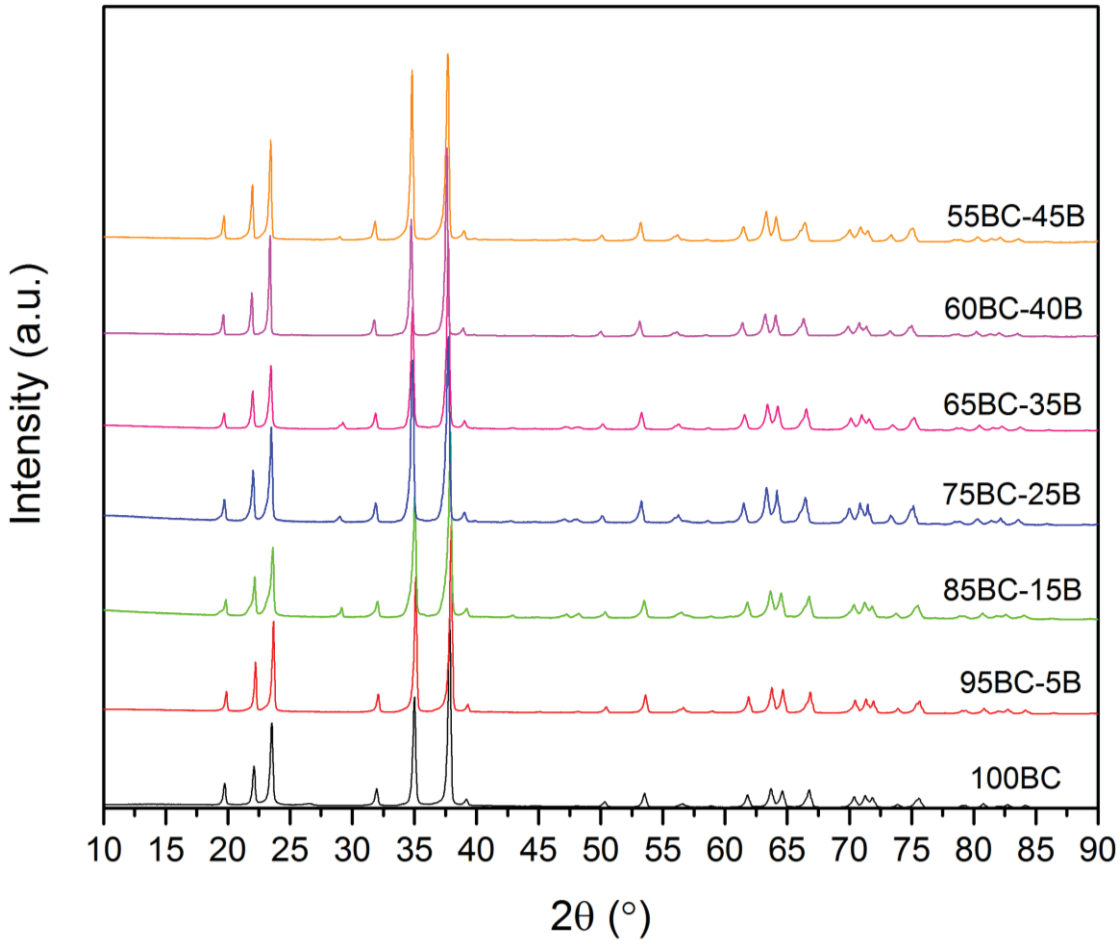

Figure 49. X-ray diffraction patterns of the cross-sectional faces of each sample. With the exception of sample 100BC (small carbon peak) the samples are phase pure.

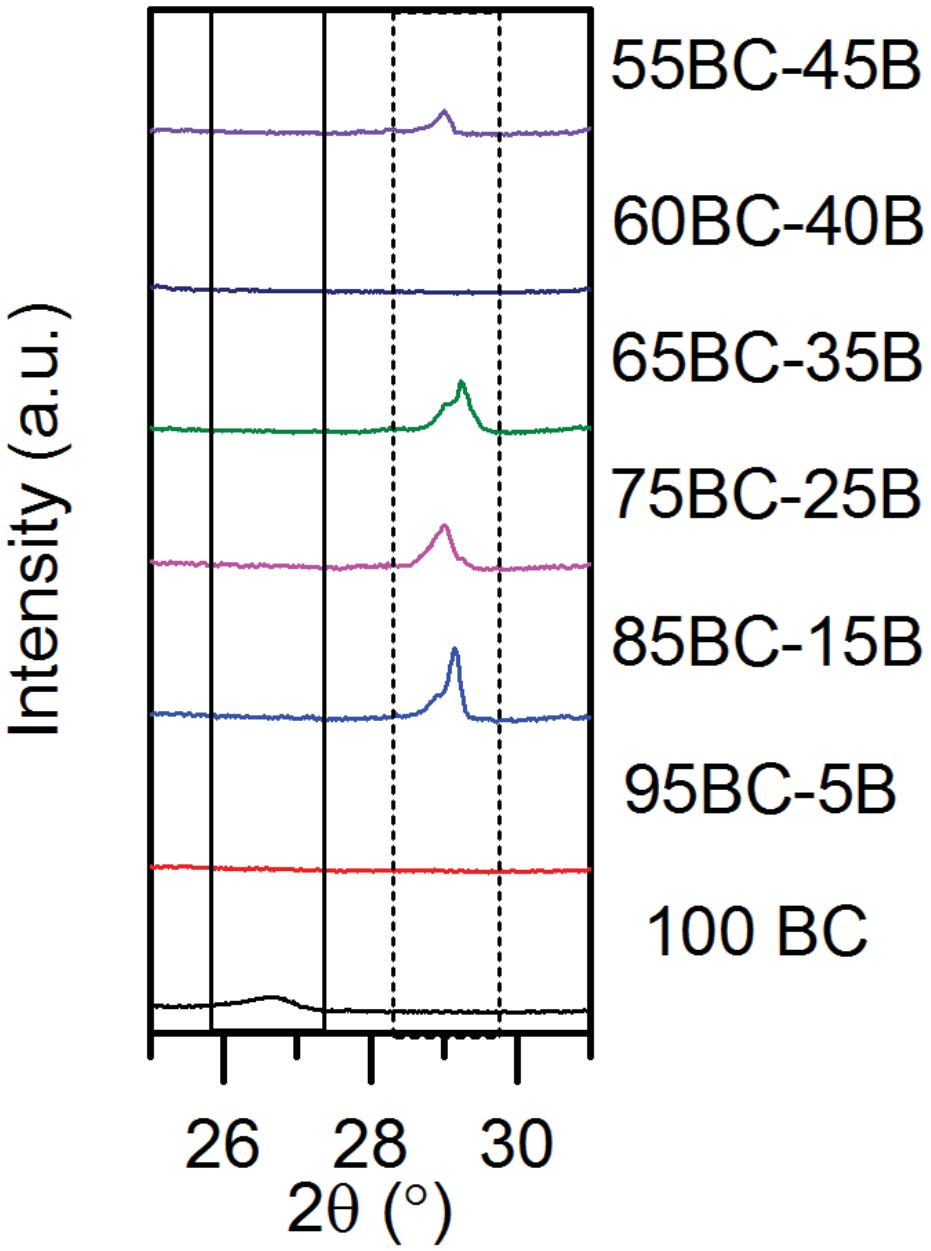

Figure 50. An expanded view of the region of the XRD pattern where free carbon would be present (solid rectangle). Only sample 100BC shows a slight peak. The dashed rectangle highlights region where a peak due to the mounting putty appears.

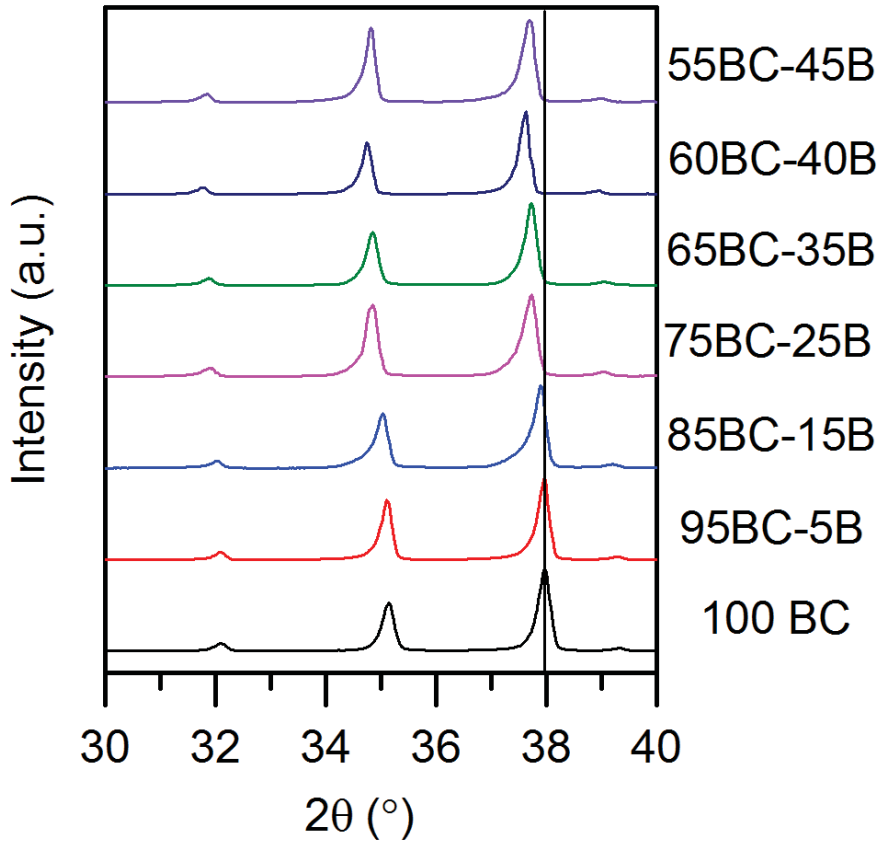

Figure 51. An expanded x-ray diffraction pattern showing shifts in the boron carbide peaks.

Using Rietveld refinement, it was possible to determine the *a* and *c* lattice parameters for the boron carbide unit cell. The results of the Rietveld refinement are shown in Table 11. As the boron content is increased, the unit cell expands resulting in an increase in the lattice parameters. The lattice parameters calculated using Rietveld refinement follow the expected trend and correspond well with the exhibited peak shifts shown in Figure 51. However, as the samples become highly boron-rich (samples 60BC-40B and 55BC-45B) the results deviate from the expected trend. The implication of these results will be explained further in the following section.

Carbon content was determined using a well-known carbon content vs. lattice parameter curve established by Aselage *et al.* in the early 1990's (Figure 4).[20] The data were fitted using linear regression and the following fit equation was used:

$$[C] = \frac{(a) - 5.679}{-0.0041} \tag{31}$$

where [C] is the carbon content in atomic percent and a is the lattice parameter determined from Rietveld refinement. The resulting carbon content values are shown in Table 11. The carbon content shows a clear decrease as the amount of added boron increases. Once again it is seen that samples 60BC-40B and 55BC-45B show variations from the overall trend. Comparing these results to the expected carbon content values in Table 7, the XRD results show an overall deviation from the expected values. This deviation is likely an artifact of the data that was used for the fit as there is an inherent error involved in fitting to the literature data. Therefore, without a creating an internal calibration curve, this method is not as accurate as other measures when determining the change in the boron carbide chemistry. However, observing that the peak shifts verifies that the boron is substituting into the boron carbide lattice and not forming a secondary boron phase in a non-destructive manner.

Table 11. Carbon content as determined from a fit of lattice parameters to Aselage data.

		Cut			
Sample		**L**	**L Mid**	**R Mid**	**R**
55BC-45B	***a***	5.63237	5.62900	5.63119	5.62883
	C% from *a* (at.%)	11.04	11.93	11.35	11.97
60BC-40B	***a***	5.63385	5.63319	5.63303	5.63599
	C% from *a* (at.%)	10.65	10.83	10.87	10.09
65BC-35B	***a***	5.63107	5.63136	5.63237	N/A
	C% from *a* (at.%)	11.69	11.62	11.37	N/A
75BC-25B	***a***	5.61953	5.61925	5.61961	5.62056
	C% from *a* (at.%)	14.50	14.57	14.49	14.25
85BC-15B	***a***	5.61043	5.61063	5.61098	5.61128
	C% from *a* (at.%)	16.72	16.68	16.59	16.52
95BC-5B	***a***	5.60315	5.60453	5.60474	5.60279
	C% from *a* (at.%)	18.73	18.37	18.31	18.82

4.2.7 Carbon Analysis

The carbon content measured from the x-ray diffraction patterns in the previous section indicate that there is a chemical change in the boron carbide with amorphous boron additions. However, the exact values that were calculated from the fit to the Aselage data are not accurate enough to truly quantify the boron to carbon ratio. Therefore, carbon analysis was done using a LECO C/S 230 chemical analyzer. The resulting carbon content is reported in Table 12. While the trend is the same as that seen in the x-ray diffraction results, the magnitude of the values are significantly different. The values for the highly boron-rich samples (55BC-45B and 60BC-40B) exhibit a different result altogether. The two samples have nearly the same chemistry and both are higher than was expected from the theoretical calculations. This, along with the previously reported observations, points to a potential anomaly happening during the sintering process. Aside from the two high boron-rich samples, the values obtained from the chemical analysis agree fairly well with the expected carbon content. Table 13 summarizes the results for the carbon analysis from x-ray diffraction and LECO analysis along with the theoretical calculations. The boron to carbon ratio calculations assumed the fact that the boron carbide was phase pure (shown through microstructural characterization and x-ray diffraction analysis) with negligible amounts of oxygen present. The LECO carbon values were consistently low for the samples with the added amorphous boron. This can be explained by the fact that sintering took place in a graphite die with a graphite foil lining. There is a potential for reactions between the amorphous boron and the graphite which would lower the boron to carbon ratio, leading to a discrepancy with the theoretical values. The discrepancies between the XRD results (column 4 and 5) and the LECO results (column 6 and 7) are due to the error

in the fitting data. There are a variety of data sets that could have been used for this fit, all giving a differing result. The main goal for the XRD analysis was to determine the chemistry qualitatively before further, more involved characterization was carried out. The carbon content values from the LECO C/S analysis are highly accurate and the values used throughout the rest of this work. Standard error is reported with the carbon content values.

Table 12. Carbon content as determined by the combustion method using a LECO C/S 230 with standard errors.

Sample	Carbon Content (at. %)
55BC-45B	12.7 ± 0.1
60BC-40B	12.7 ± 0.3
65BC-35B	13.7 ± 0.3
75BC-35B	15.4 ± 0.1
85BC-15B	17.4 ± 0.4
95BC-5B	18.6 ± 0.1

Table 13. Summary of carbon content determination.

Samples	Expected C (at. %)	Expected B/C	Actual Carbon (at. %) (XRD)	Actual B/C (XRD)	Actual Carbon (at. %) (LECO)	Actual B/C (LECO)
55BC-45B	10.8	8.3	11.4	7.8	12.7	6.9
60BC-40B	11.8	7.5	10.9	8.2	12.7	6.9
65BC-35B	12.8	6.8	11.4	7.8	13.7	6.3
75BC-25B	14.9	5.7	14.5	5.9	15.4	5.5
85BC-15B	16.9	4.9	16.6	5.0	17.4	4.7
95BC-5B	18.8	4.3	18.3	4.5	18.6	4.3
100BC	19.9	4.0	---	---	19.9	4.0

4.2.8 Raman Microscopy

The chemical homogeneity of the boron-rich samples was examined using Raman microspectroscopy. Unlike x-ray diffraction, the laser used for Raman microspectroscopy can be focused to a very small spot size allowing for chemical characterization on the micron scale. Two different analyses were performed. The first analysis was a point scan on the polished surface of each specimen. These scans established the expected Raman spectra along with peak locations. The spectra can be seen in Figure 52. Figure 52 shows the six peak locations that were examined. These peaks are significant in qualitatively determining the change in the chemistry of the boron carbide, as well as provide insight into what changes are occurring at the atomic level. To determine the actual peak location, the spectra were fit with a series of curves to ensure the best fit. Each sample spectra was fit with 23 unique curves with the exception of sample 55BC-45BC which took an additional three curves to gain a proper fit (Figure 53). Further, the peaks at ~480 cm^{-1} (Peak 3) and 530 cm^{-1} (Peak 4) were measured as it has been shown that the difference between the Raman shift of the peaks is highly correlated with changes in chemistry (Figure 54). The results are shown in Table 14 and visually in Figure 55. There is a very clear change in the peak locations as more boron is added. Measuring the difference in the peak positions once again shows a nearly linear decrease as the boron additions increase. While this difference is not a quantitative measure of the chemistry changes within the samples, it is a quick and easy qualitative measure of the chemistry that can be used to determine homogeneity on a much smaller scale than XRD. This result also provides insight into the changes that are occurring within the boron carbide lattice. The Raman band at 530 cm^{-1} has been linked to the liberation mode of the icosahedron whereas the

band at 480 cm^{-1} has been linked to the stretching mode of the CBC chains.[16, 18] The fact that the shifts are occurring in opposite directions would seem to confirm the differing nature of the bands.

Examination of the Raman band at ~1080 cm^{-1} (Peak 5) shows further effects of the chemistry change in boron carbide. The 1080 cm^{-1} peak has been well identified as the breathing mode of the 12 atom icosahedra[17]. The downshift in the peaks is evident in Figure 56. It is important to note that the downshift diminishes from sample 65BC-35B to 55B-45B. At these chemistries, it has been shown that the C in the $B_{11}C$ icosahedra is substituted by B. Therefore, the accepted atomic configuration at 13 at.% C would be B_{12}(CBC). A further decrease in the carbon content would involve a substitution in the inter-icosahedral chain. At 13 at.% C, it would be expected that the 1080 cm^{-1} peak would stop shifting due to the changing substitutional sites. This has been observed in the data, confirming the nature of the substitution.

The last set of Raman bands that were analyzed are shown in Figure 57. The bands at 270 cm^{-1} (Peak 1) and 320 cm^{-1} (Peak 2) have not been as unambiguously assigned as some of the other boron carbide Raman bands. However, Tallant and Aselage[16] reported the appearance of these bands and further examination by Werheit[19] attributed these bands to the chain rotations. Figure 57 shows no real change in these bands with chemistry, implying the source of these peaks is not affected by the change in chemistry down to ~12.5 at.% C (potential changes at lower carbon contents may be possible). Lastly, the band at 370 cm^{-1} (Peak 6) appears in only three samples: 65BC-35B, 60BC-40B and 55BC-45B. The appearance of this band has been noted in previous work but no clear assignment has been made.[78] However, the appearance of these bands at carbon contents below 13 at.%

would point to a new substitution mechanism that has not been previously seen. This peak formation is likely due to the formation of B-B bonds within the inter-icosahedral chain.

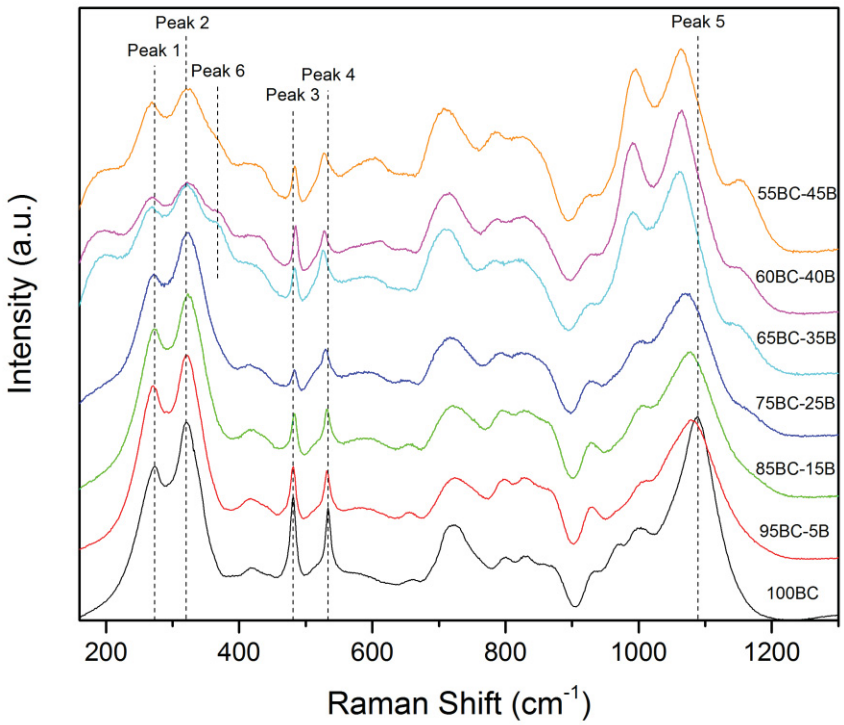

Figure 52. Raman spectra of boron-rich boron carbide samples. Peak locations noted are dependent upon chemistry changes and have been examined further.

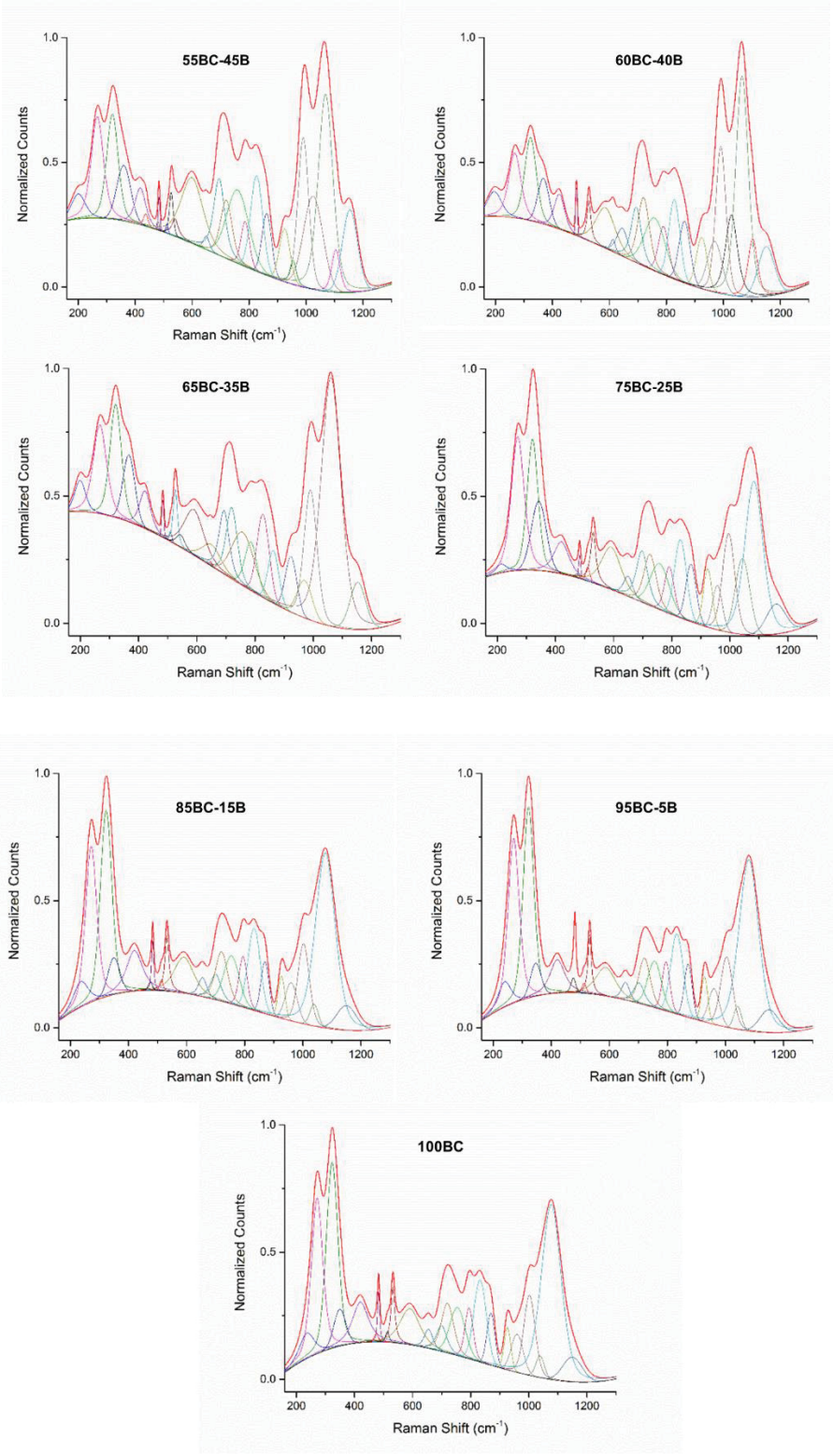

Figure 53. Curve fits for each Raman point spectra. 23 unique curves were fit to each spectra with the exception of sample 55BC-45B which took 26 unique curves.

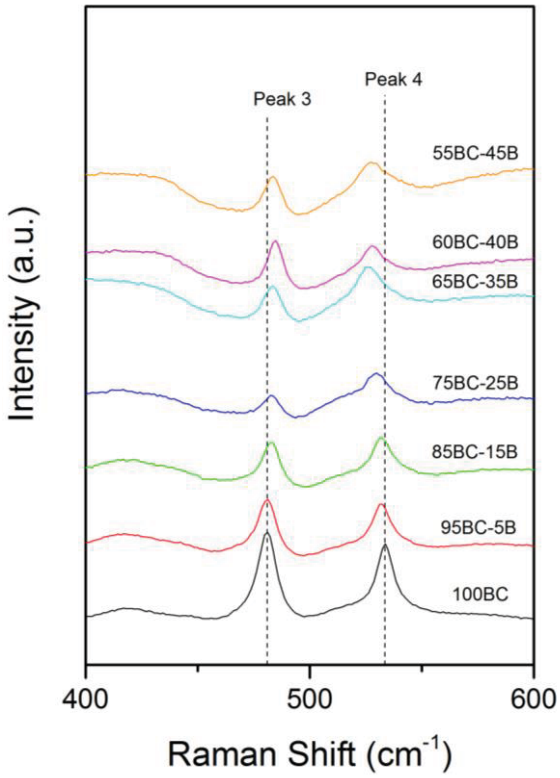

Figure 54. Raman spectra zoomed in to show shifts in 480 cm^{-1} and 530 cm^{-1} peaks.

Table 14. Measured peak locations for the Raman bands at 480 cm^{-1} and 530 cm^{-1}.

Sample	Peak 3 Location (cm^{-1})	Peak 4 Location (cm^{-1})	Difference
55BC-45B	483.4	527.7	44.3
60BC-40B	484.6	527.6	43.0
65BC-35B	483.2	526.2	43.0
75BC-25B	482.7	530.0	47.3
85BC-15B	482.7	532.0	49.3
95BC-5B	480.9	531.9	51.0
100 BC	480.9	533.6	52.7

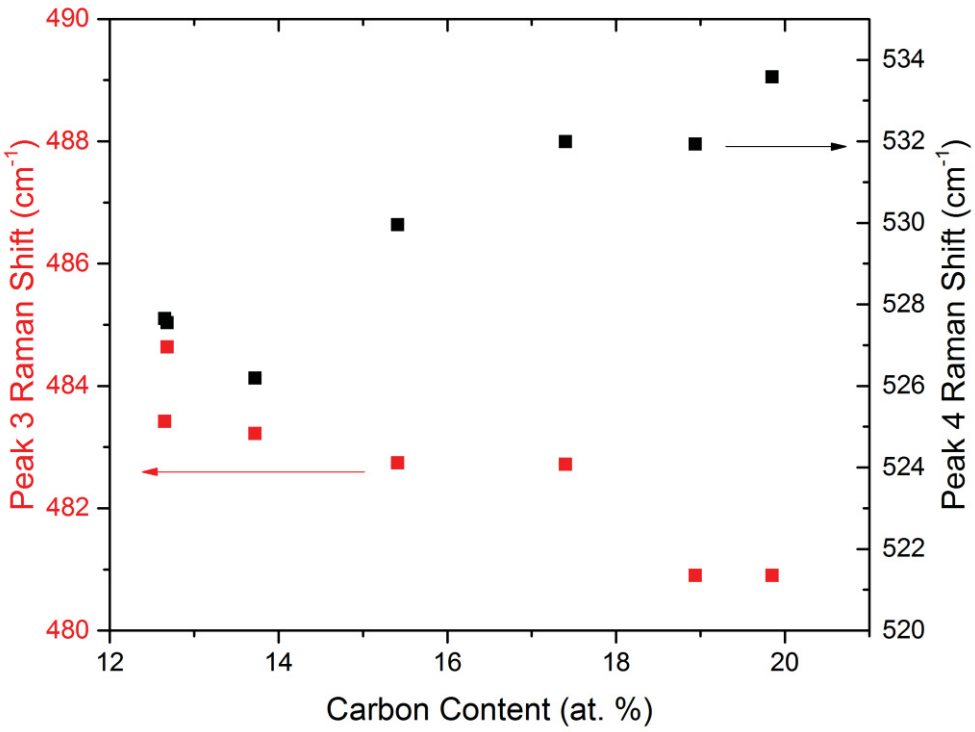

Figure 55. The plot of 480 cm^{-1} and 530 cm^{-1} peak shifts showing nearly linear nature of the shift.

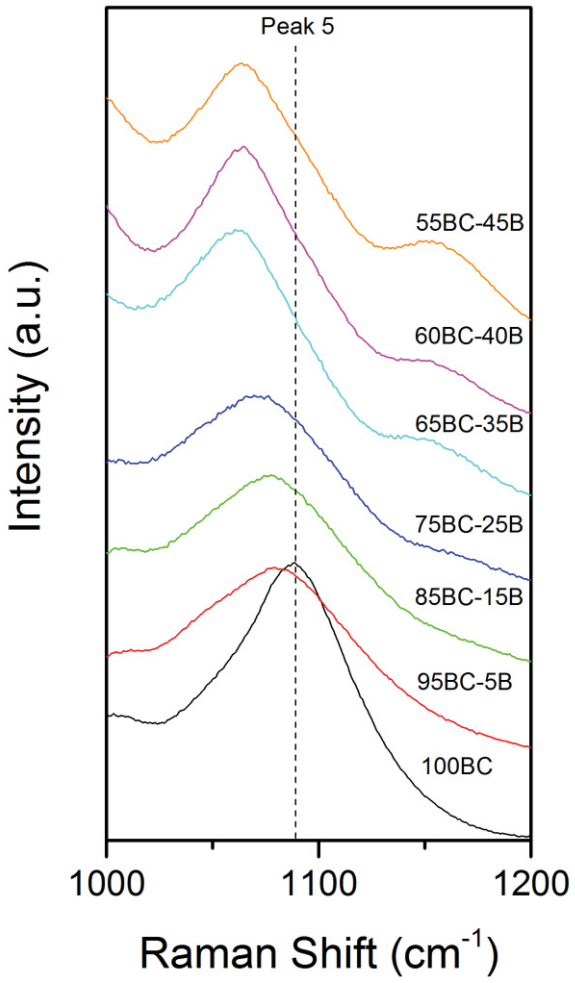

Figure 56. Raman spectra zoomed in to show the shift in 1080 cm^{-1} peak.

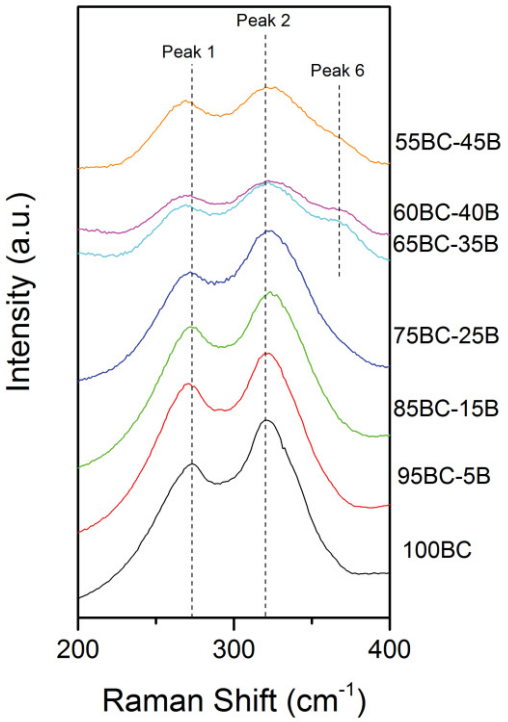

Figure 57. Raman spectra zoomed in to show the independent nature of the 270 cm^{-1} and 320 cm^{-1} with chemistry. The spectra also show the appearance of the 370 cm^{-1} peaks at low carbon contents.

For the second analysis, line scans were performed across the etched surface of each sample. Etched samples were used so that the grain structures could be seen in the optical images. By performing a line scan, it is possible to determine the homogeneity of the sample from one grain to another. If the samples are homogeneous, the measured values of each point measurement across the line scan should not deviate significantly from the results reported in Table 14. Three random locations were chosen for each sample and a line scan was performed. Point measurements were made every 1 µm for samples 100BC through 65BC-35B and every 2 µm for samples 60BC-40B and 55BC-45B (due to the grain

size change). Figures 58 through 63 show the resulting difference in the Raman shift for the three line scans.

Samples 95BC-5B, 85BC-15B and 75BC-25B show very little deviation from the results obtained from the point scans in Table 14. This suggests that there is very little, if any, change in the chemistry from grain to grain. Sample 65BC-35B shows slightly higher deviation indicating that the sample may be losing some of the homogeneity that was seen in the lower boron addition samples. However, with a standard deviation of ~0.50 cm^{-1} the sample is still considered to be homogenous. The last two highly boron-rich samples show much more variation in the line scans. This indicates that the samples are not homogeneous from grain to grain. There were issues with porosity skewing the results, therefore care was taken to avoid large pores and any data points that hit a large pore were removed from the analysis (<10% of data was affected).

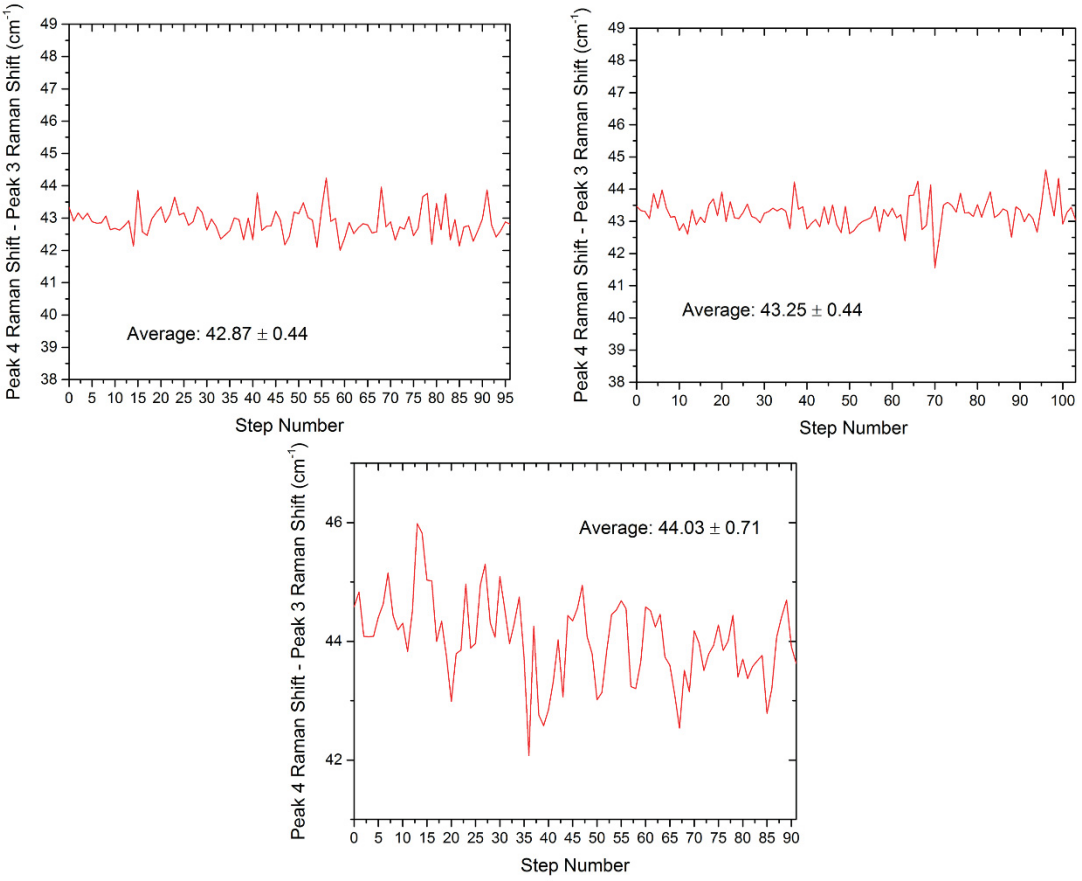

Figure 58. Sample 55BC-45B peak separation (Peak 4-Peak 3) as determined from three random line scans.

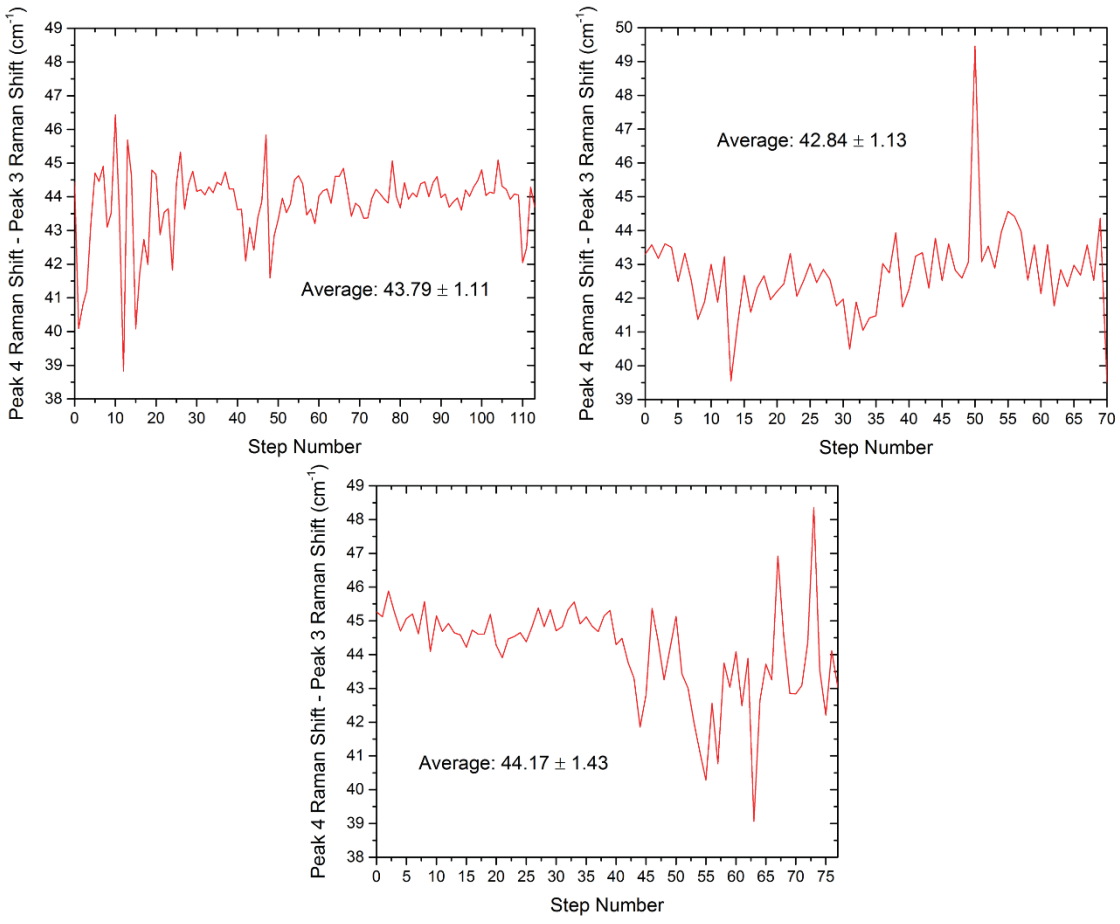

Figure 59. Sample 60BC-40B peak separation (Peak 4-Peak 3) as determined from three random line scans.

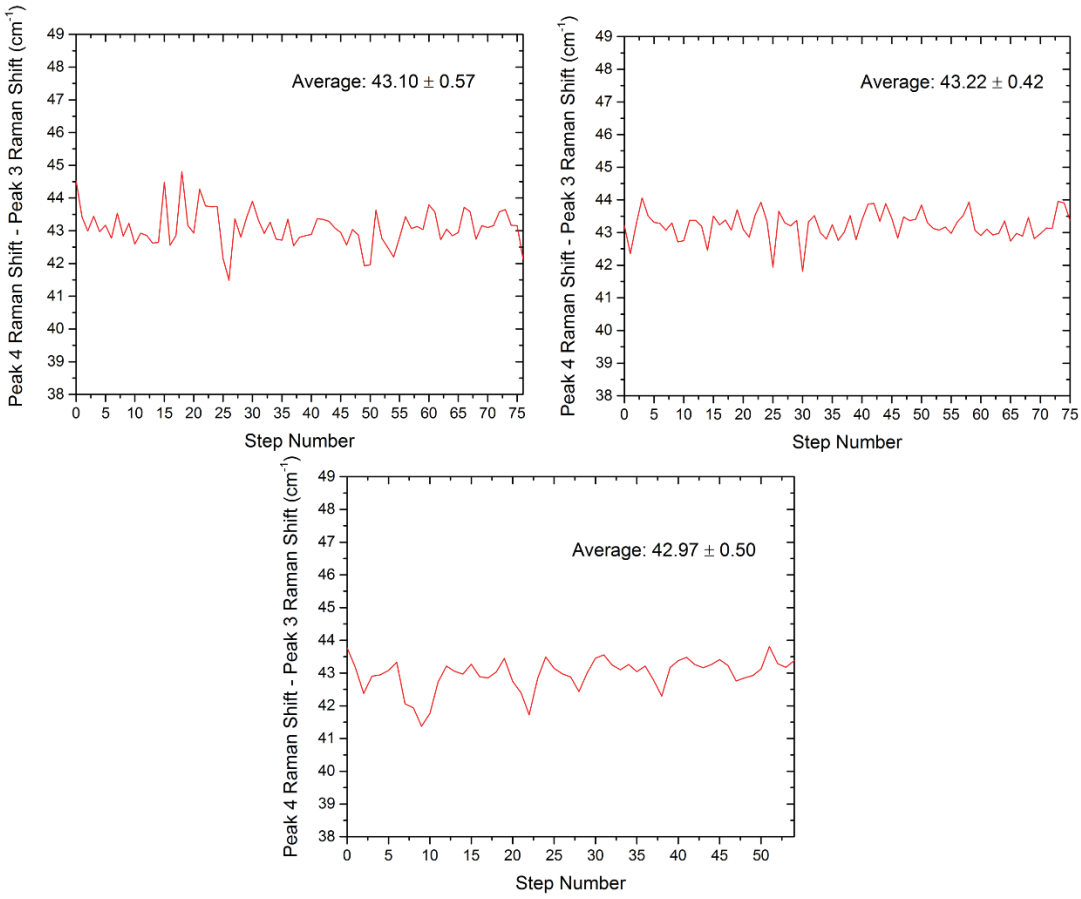

Figure 60. Sample 65BC-35B peak separation (Peak 4-Peak 3) as determined from three random line scans.

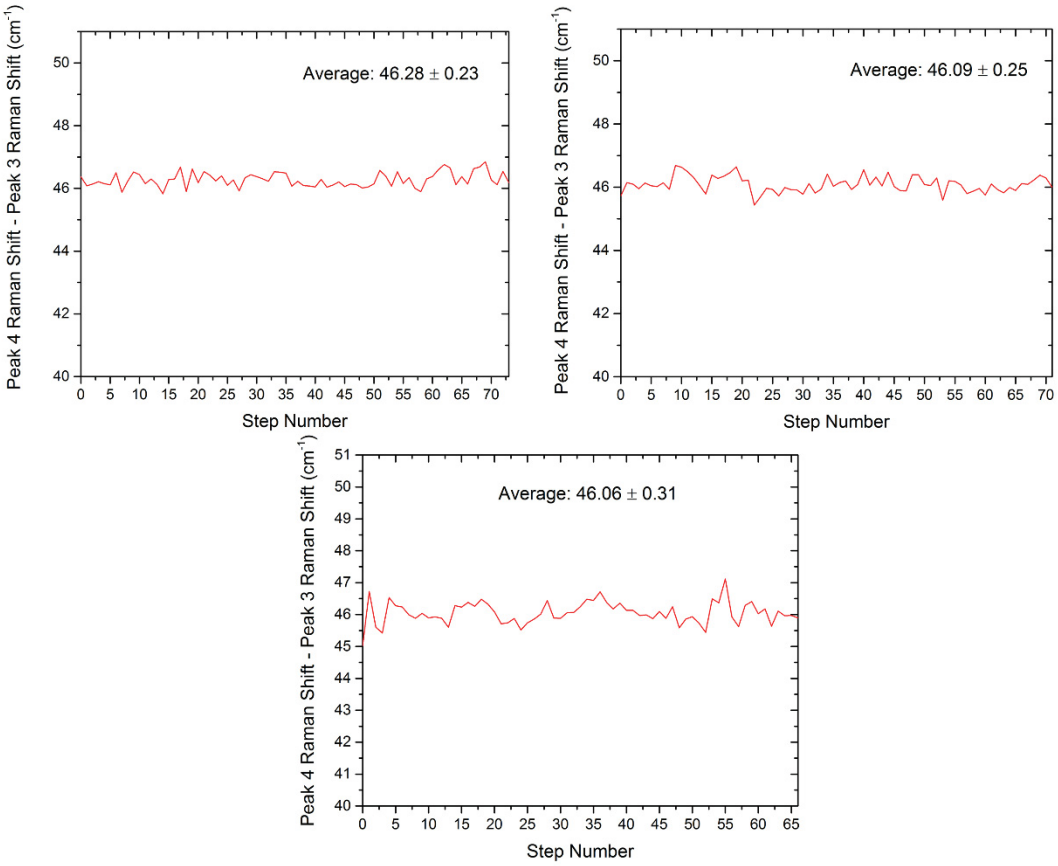

Figure 61. Sample 75BC-25B peak separation (Peak 4-Peak 3) as determined from three random line scans.

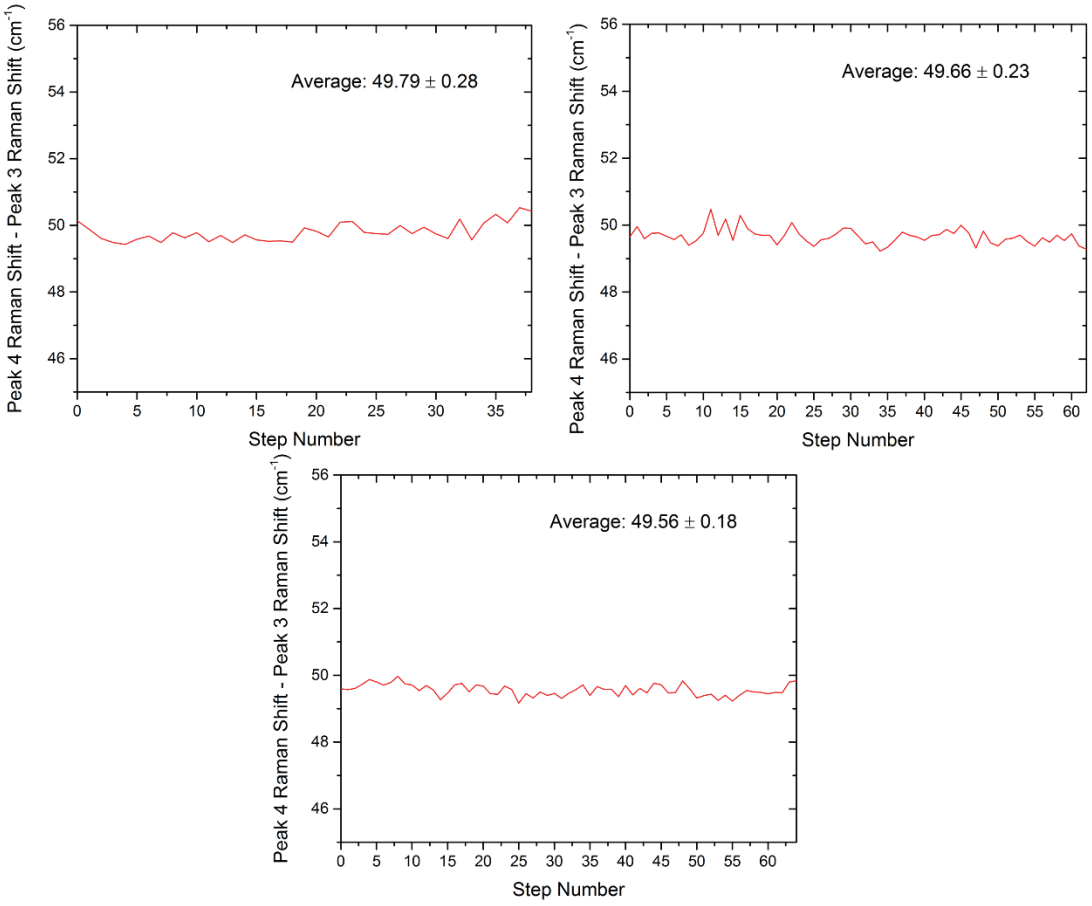

Figure 62. Sample 85BC-15B peak separation (Peak 4-Peak 3) as determined from three random line scans.

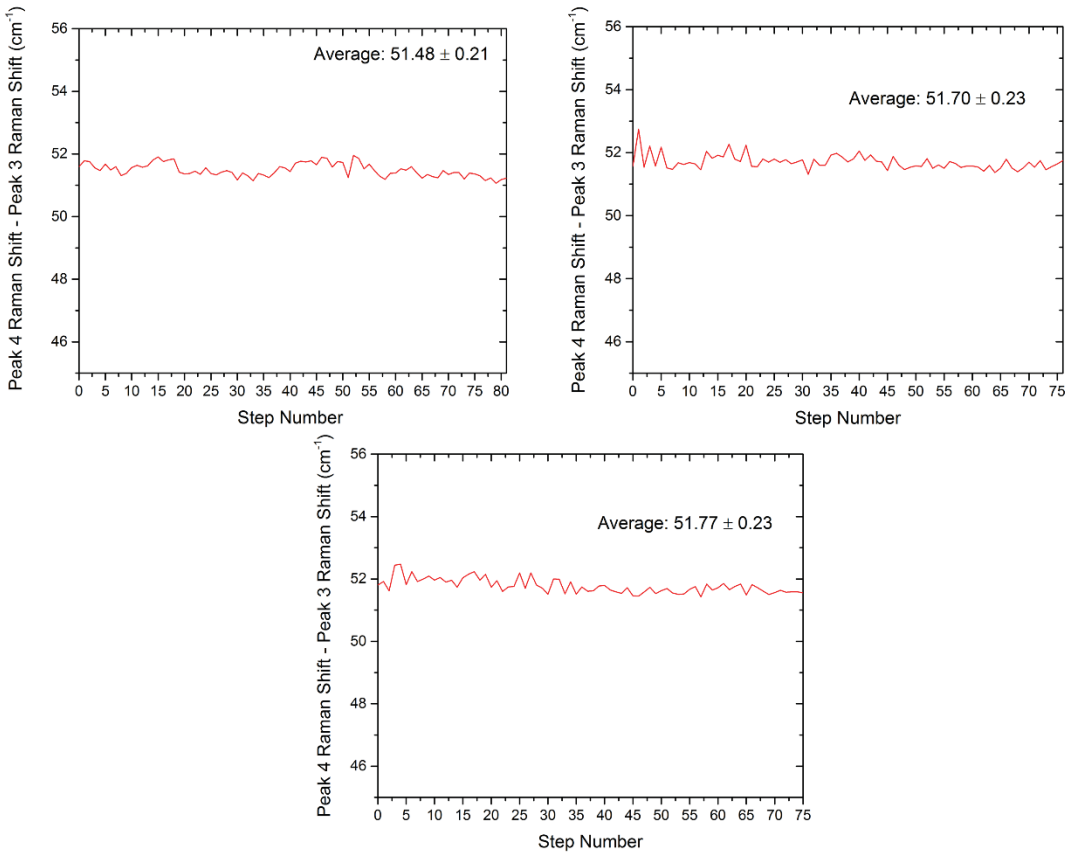

Figure 63. Sample 95BC-5B peak separation (Peak 4-Peak 3) as determined from three random line scans.

4.2.9 Reaction Rate Experiment

The chemical and microstructural characterization results for samples 60BC-40B and 55BC-45B reported in the previous sections have shown abnormal deviations from the expected trends. These deviations are assumed to be due to a loss of amorphous boron during the spark plasma sintering process. It has been observed in this study that amorphous boron has a tendency to melt during spark plasma sintering at a temperature of ~1900°C. This is due to the method of temperature measurement for spark plasma sintering. The optical pyrometer measures temperatures from the outside of the graphite die, resulting in measured temperature that are potentially much lower than the temperature within the die. This error in temperature measurement can lead to temperatures in excess of the melting point of amorphous boron. However, this problem is not encountered in the samples with smaller boron additions (<40 wt.%). Two potential causes have been suggested. First, with the addition of >40 wt.% amorphous boron, the amorphous boron may form a connected network throughout the compact which could become a path for the current. This may in turn cause locally high temperatures that melts the amorphous boron. At lower amorphous boron additions this would not be seen because an interconnected network is not formed eliminating these locally high temperatures. It has also been hypothesized that in low boron addition samples (< 35 wt.%) the reaction rate is fast enough for the reaction to go to completion before the melting point of amorphous boron is reached. However, as the amount of amorphous boron is increased (≥ 40 wt.%) the reaction rate is no longer fast enough to carry the reaction to completion allowing for the amorphous boron to melt and flow out of the graphite die.

To get a better understanding of the reaction rate a set of samples with 40 wt.% amorphous boron additions were sintered at temperatures ranging from 1400°C up to 1900°C with 100°C intervals and a final sample was sintered at 1900°C with a 5-minute hold. These samples were processed using Starck Grade HD20 boron carbide powders due to insufficient amounts of RCR powders. The Starck Grade HD20 powder was determined to be a suitable substitute for this experiment due to its similar particle size (~1 μm) and relatively low amounts of impurity. The x-ray diffraction data from these samples are shown in Figure 64. The solid box in Figure 64 indicates the region in which an amorphous boron peak would show up. The amorphous peak is evident at sintering temperatures up to 1700°C after which the peak becomes less prominent and finally disappears in the final samples (Figure 65). To determine the amount of amorphous materials in each sample, Rietveld refinement was once again used. This time, an amorphous peak was added to the refinement process. Table 15 shows the percent amorphous material in each of the patterns as determined from Rietveld refinement. Once again at 1700°C the percent amorphous material begins to drop significantly until there is no amorphous material. This indicates that the reaction begins to take off at temperatures in excess of 1700°C. However, at 1900°C there is still ~ 0.6 wt. % amorphous material present in the sample. Based on the previous observation that boron begins to melt at ~1900°C it is possible that a liquid boron phase replaced the amorphous material. To further examine this claim, the peak shift discussed previously was once again analyzed (Figure 66). It would be expected that there is a systematic peak shift in the boron carbide peaks from 1700°C to 1900°C with a 5-minute hold. However, the XRD patterns show that there are no significant peak shift

observed. This indicates that while the amorphous peak is eliminated there is no further reaction taking place, meaning that any boron remaining has melted out.

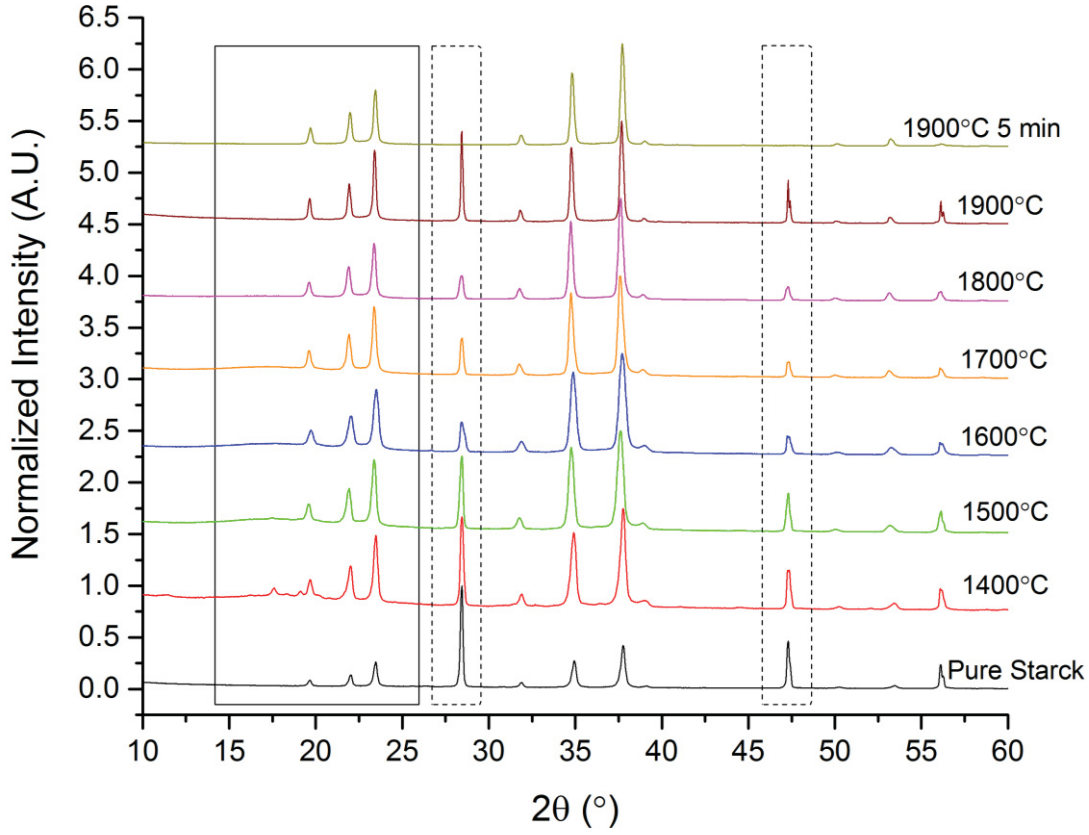

Figure 64. X-ray diffraction patterns of samples sintered at different temperatures. The solid rectangle indicated the region of the amorphous boron hump. The dashed rectangles indicate silicon reference peaks.

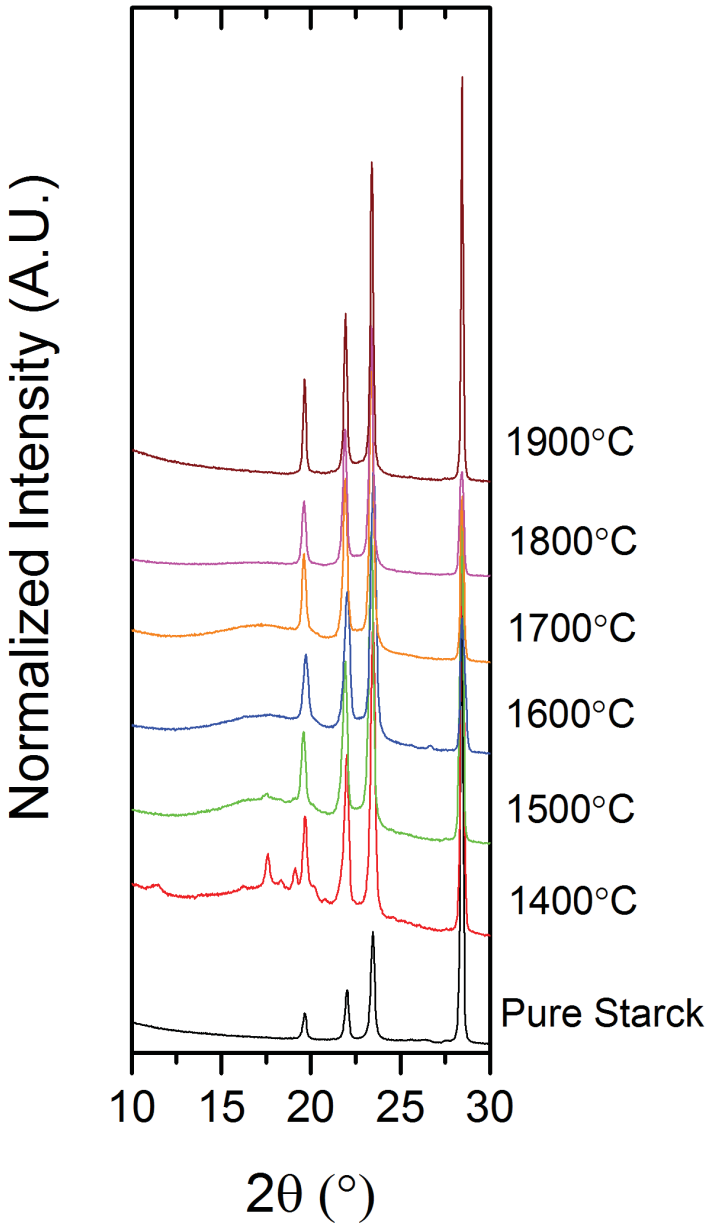

Figure 65. X-ray diffraction pattern zoomed in to show amorphous peak due to presence of amorphous boron.

Table 15. The percent amorphous material of each sample as determined by Rietveld refinement.

Sample	Amorphous Material (wt. %)
1900 – 5min	0.0
1900	0.6
1800	2.1
1700	4.2
1600	4.5
1500	4.5

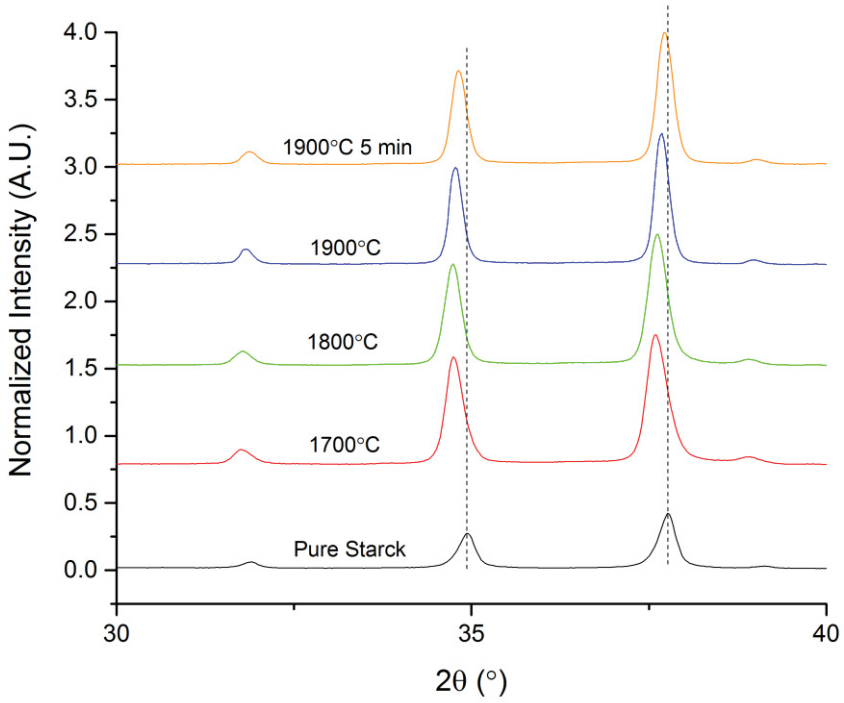

Figure 66. X-ray diffraction pattern zoomed in to show peak shift of the boron carbide peaks.

4.3 Objective 3 Results

4.3.1 Non-Destructive Ultrasound Analysis for Elastic Moduli Measurement

The non-destructive nature of the ultrasound measurements of the elastic properties is important for this work as the sample size was limited to what could be processed in the SPS unit. Samples 95BC-5B through 65BC-35B were measured using the method outlined in section 3.3.4. Sample 100BC was not measured because of surface damage created during grinding, making it impossible to obtain ultrasound results. Samples 60BC-40B and 55BC-45B were not measured due to the high degree of porosity making it difficult to obtain reliable results. The resulting longitudinal and transverse wave speeds are shown in Table 16. The Poisson's ratio, Young's modulus, shear modulus and bulk modulus were calculated using equations 27 through 30 in section 3.3.4. The results are reported in Table 17 and Figures 67 through 70. Due to the size of the transducers, only a single measurement was able to be made on each sample. Therefore, the error in the results reported is estimated to be ±2 % due to the error in measure and small instrument error. Each property measured using the ultrasound technique shows a statistical dependence on chemistry.

For each measured elastic moduli, a linear fit was performed and the 95% confidence interval was determined. The fit equation for the Poisson's ratio was,

$$\nu = (0.302 \pm 0.016) + (-0.007 \pm 0.001)[C] \quad (32)$$

This fit indicates that the Poisson's ratio is statistically dependent on the carbon content as the zero slope is not within the 95% confidence interval, (0.006, 0.008). The same

dependence is apparent with the Young's ,shear, and bulk moduli. The fit equation for the Young's modulus was,

$$E = (343 \pm 11) + (5.9 \pm 0.7)[C] \quad (33)$$

The shear modulus fit equation was,

$$G = (127 \pm 6) + (3.5 \pm 0.3)[C] \quad (34)$$

The fit equation for the bulk modulus was,

$$K = (269 \pm 9) + (-1.9 \pm 0.6)[C] \quad (35)$$

Looking back to section 2.7.2 and the modified Lundberg model proposed by LaSalvia[69], it was shown that an increasing the material's Poisson's ratio of the material of interest was one way to produce a more ductile material. The Poisson's ratio measured in this work shows a significant increase with decreasing carbon content, signifying a material that may exhibit more plasticity much like silicon carbide. While this change in the Poisson's ratio may be significant in the bounds of the LaSalvia model shown in Figure 24, it should be noted that other materials properties were included as constants in the calculation which may not be true for these materials. It has also been suggested through modeling that altering the Young's modulus of boron carbide may change the size and shape of the boron carbide fragments after shock loading, leading to increased performance of the material. Nonetheless, these results show that there is a clear and significant effect on the elastic properties of boron carbide due to changes in chemistry.

Table 16. Longitudinal and transverse wave speeds measured from ultrasound NDE.

Sample	Longitudinal Wave Speed (m/s)	Transverse Wave Speed (m/s)
65BC-35B	13846	8411
75BC-25B	13925	8506
85BC-15B	13938	8628
95BC-5B	14030	8819
100BC	---	---

Table 17. Poisson's ratio and elastic moduli calculated from the waves speeds.

Sample	Poisson's Ratio	E (GPa)	G (GPa)	K (GPa)
65BC-35B	0.208 ± 0.004	424 ± 8	175 ± 4	242 ± 5
75BC-25B	0.202 ± 0.004	434 ± 9	181 ± 4	243 ± 5
85BC-15B	0.189 ± 0.004	442 ± 9	186 ± 4	237 ± 5
95BC-5B	0.173 ± 0.003	456 ± 9	194 ± 4	233 ± 5
100BC	---	---	---	---

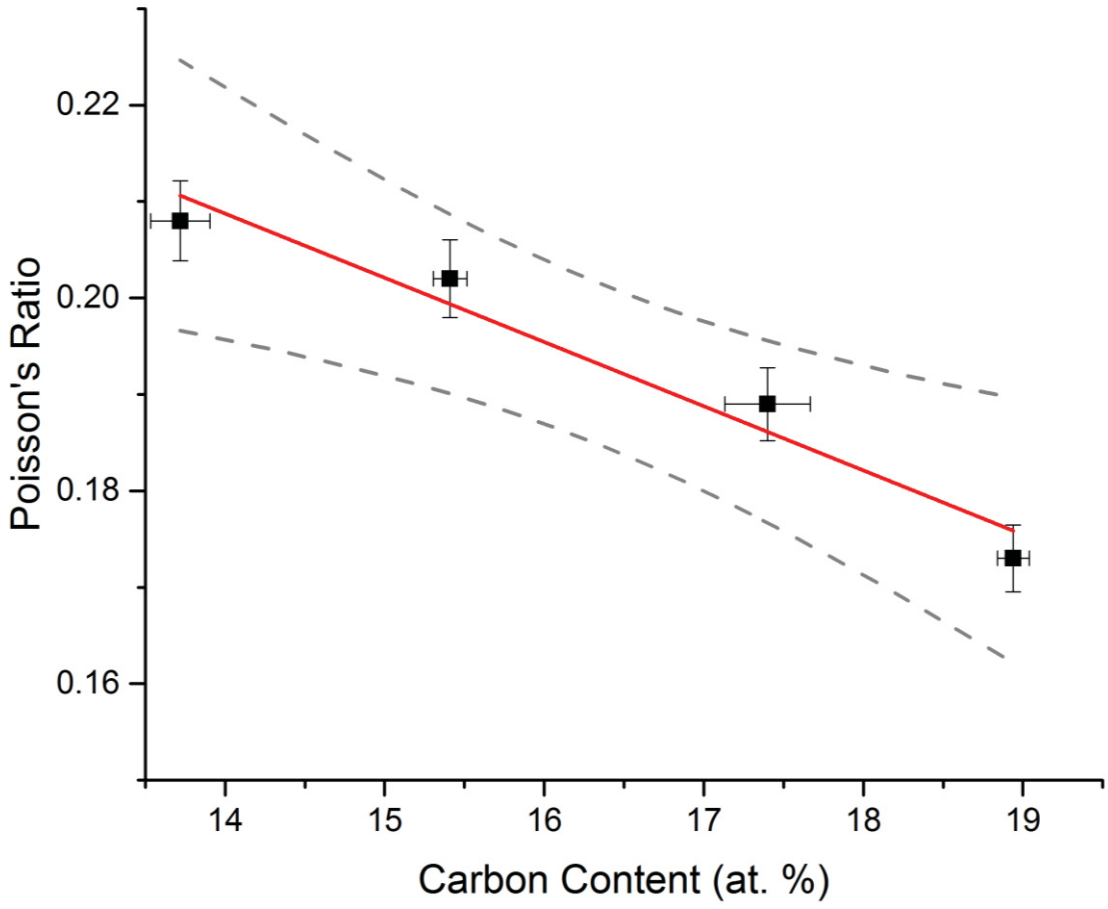

Figure 67. Effect of the carbon content on the Poisson's ratio.

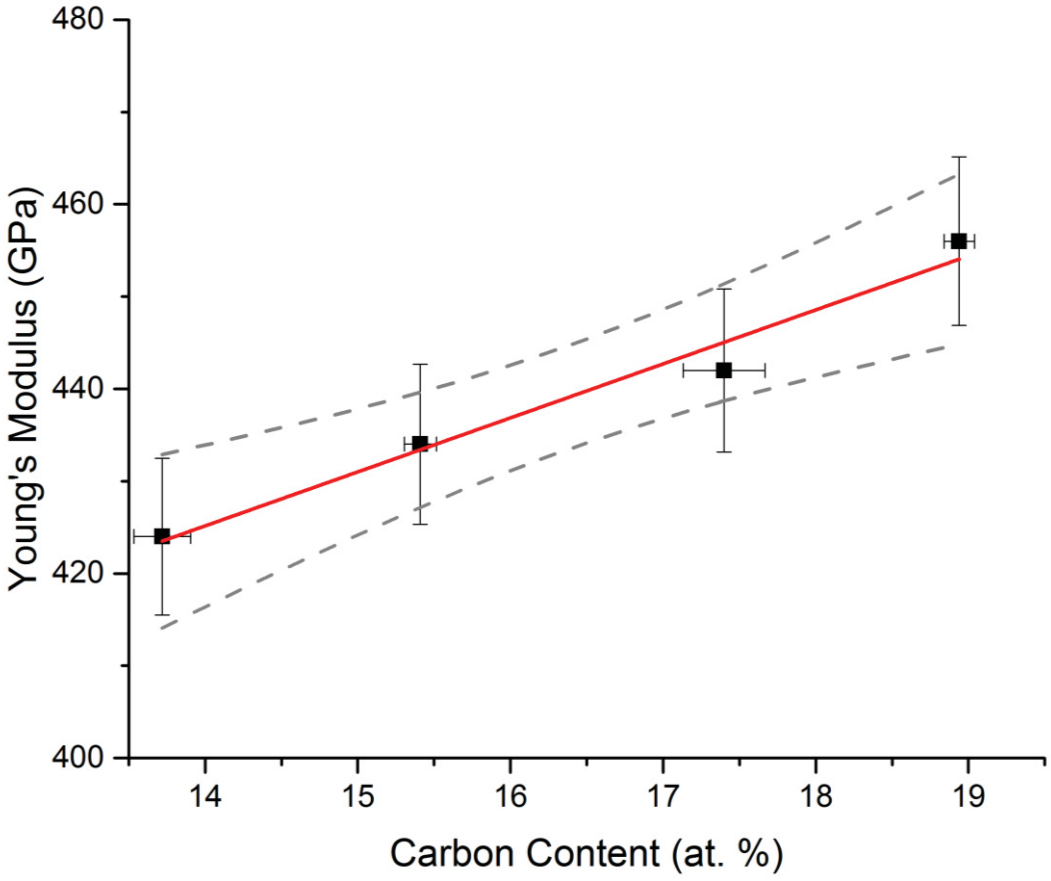

Figure 68. Effect of the carbon content on the Young's Modulus.

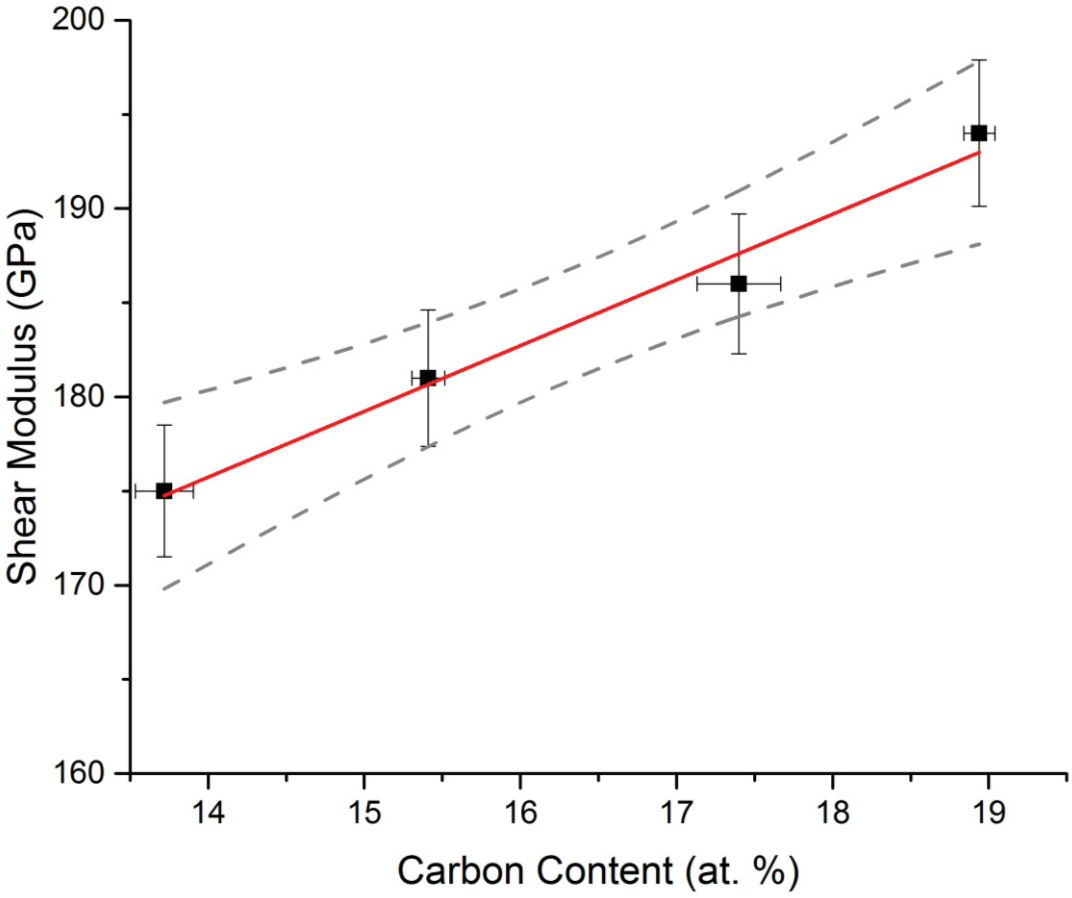

Figure 69. Effect of the carbon content on the shear modulus.

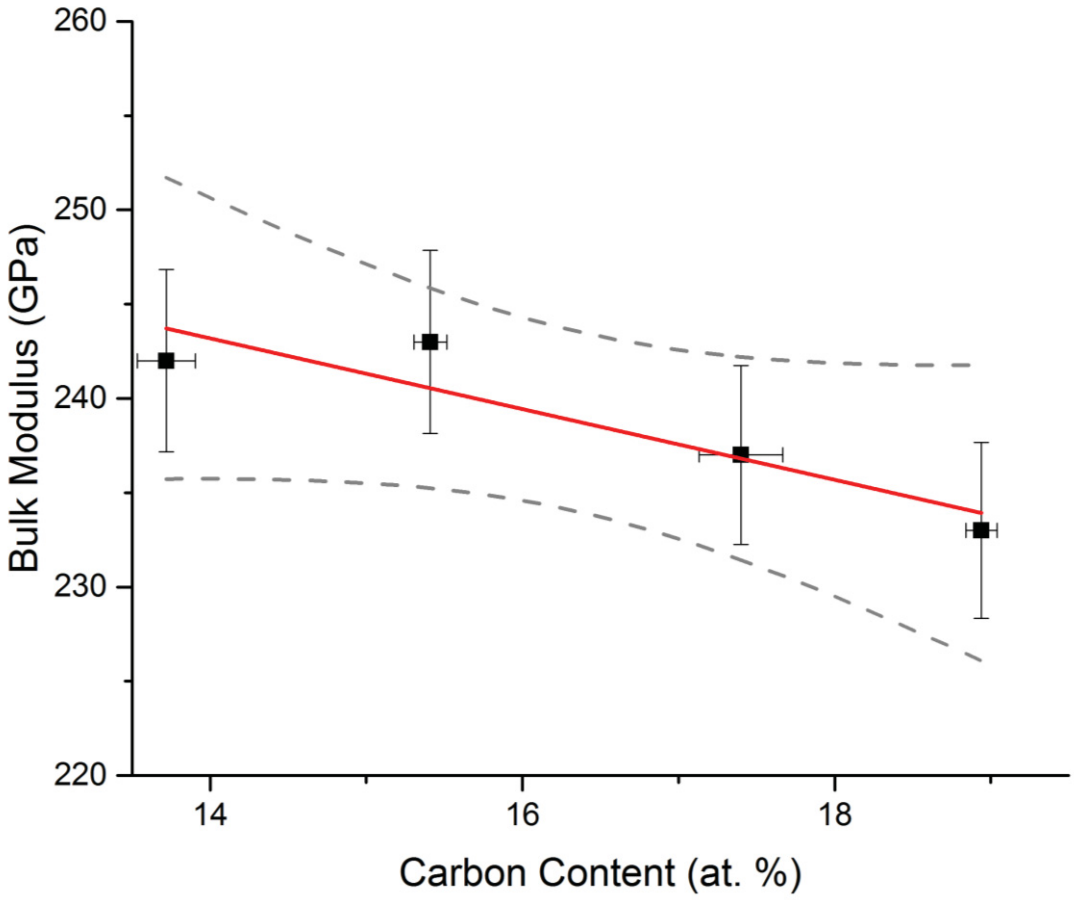

Figure 70. Effect of the carbon content on the bulk modulus.

4.3.2 Knoop Microhardness

Knoop indents were made at 4 different loads (100, 200, 500, 1000 g) with 12 indents for each load. Indents which hit porosity or inclusions were not used in the hardness calculations. Table 18 displays the hardness values for samples 100BC through 65BC-35B. Samples 60BC-40B and 55BC-45B were not analyzed due to the high degree of porosity making it impossible to achieve an acceptable amount of indents for accurate calculations. The first important observation from this data is that the 100 g Knoop hardness values are much higher than the reported values for polycrystalline boron carbide and are more in line with values reported for boron carbide single crystals.[79] The second

observation made from this data is that the indentation size effect is clearly present in this data (Figure 71), as would be expected for boron carbide.

Table 18. Knoop hardness results.

Sample	Load	Knoop Hardness (GPa)	Standard Error
65BC-35B	100	37.3	0.4
	200	29.7	0.2
	500	24.9	0.1
	1000	22.8	0.1
75BC-25B	100	37.6	0.4
	200	30.1	0.5
	500	26.1	0.3
	1000	25.2	0.3
85BC-15B	100	37.2	0.3
	200	30.4	0.3
	500	25.8	0.3
	1000	23.9	0.3
95BC-5B	100	34.5	0.3
	200	30.8	0.4
	500	25.4	0.2
	1000	23.7	0.3
100BC	100	35.4	0.8
	200	30.5	0.4
	500	26.4	0.3
	1000	23.7	0.3

To understand the effect the chemistry changes have on the microhardness of the samples, the 100 g load hardness was plotted versus the carbon concentration (Figure 72). Examination of Figure 72 shows a slight increase in the hardness as the carbon content is changed from ~20 at.% to ~18 at.% then the hardness plateaus around 37 GPa. Using a linear fit along with the 95% confidence interval it was determined that the Knoop hardness has a statistical dependence on the carbon content. The fit equation for the Knoop hardness was,

$$HK = (43.9 \pm 3.2) + (-0.44 \pm 0.18)[C] \quad (36)$$

The zero slope does not fall within the 95% confidence interval therefore statistical dependence is confirmed. However, sample 100 was shown to have 2.8% porosity whereas the other samples all had less than 1.5 % porosity. As stated previously, indents that were clearly hitting pores were eliminated from analysis however, the indent could still interact with a subsurface pore or pores that are nearby but not in contact. Both of these cases could ultimately affect the measured hardness and decrease the average measured hardness. Sample 95BC-5B has a smaller amount porosity present, however, the increase in grain size that is seen in Table 10 in Section 4.2.4 has likely caused a decrease in the hardness of the material. Taking into account both of the porosity and grain size effects, the dependence would likely disappear.

The overall trend seen in the hardness versus carbon content curve is contrary to the results that Niihara has reported for CVD boron carbide, in which he reports a clear peak in the hardness at ~20 at.% carbon followed by a drop off when carbon content is increased or decreased.[8] It should be noted that Niihara's reported hardness values are Vickers hardness of a very high purity CVD thin film. Nonetheless, the overall trend would be expected for other indentation methods. While Niihara's data differs from the results of this work, other reports that utilized Knoop hardness of bulk samples also lacked a trend in the hardness versus carbon content data.[11, 12] Therefore, for bulk, polycrystalline samples elimination of the effects of porosity, grain boundaries, and any other detrimental microstructural features becomes important for the accurate understanding of the effects of chemistry. These features are nearly impossible to avoid using a Knoop indenter as the aspect ratio of the indenter leads to one axis of the indentation to be much larger than the grain size of the specimen being analyzed. Because of this, further hardness analysis is

needed to determine the true effect of chemistry for the samples in this work (i.e. nano-indentation).

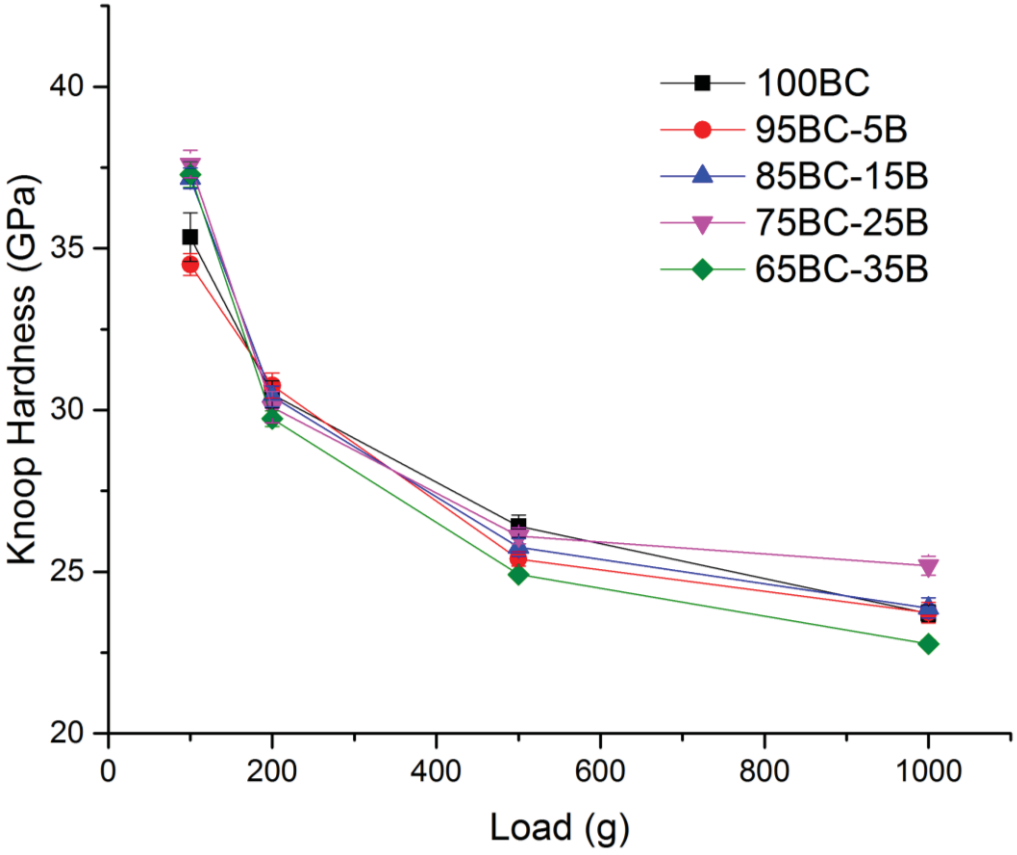

Figure 71. Load-hardness curve showing the presence of indentation size effect.

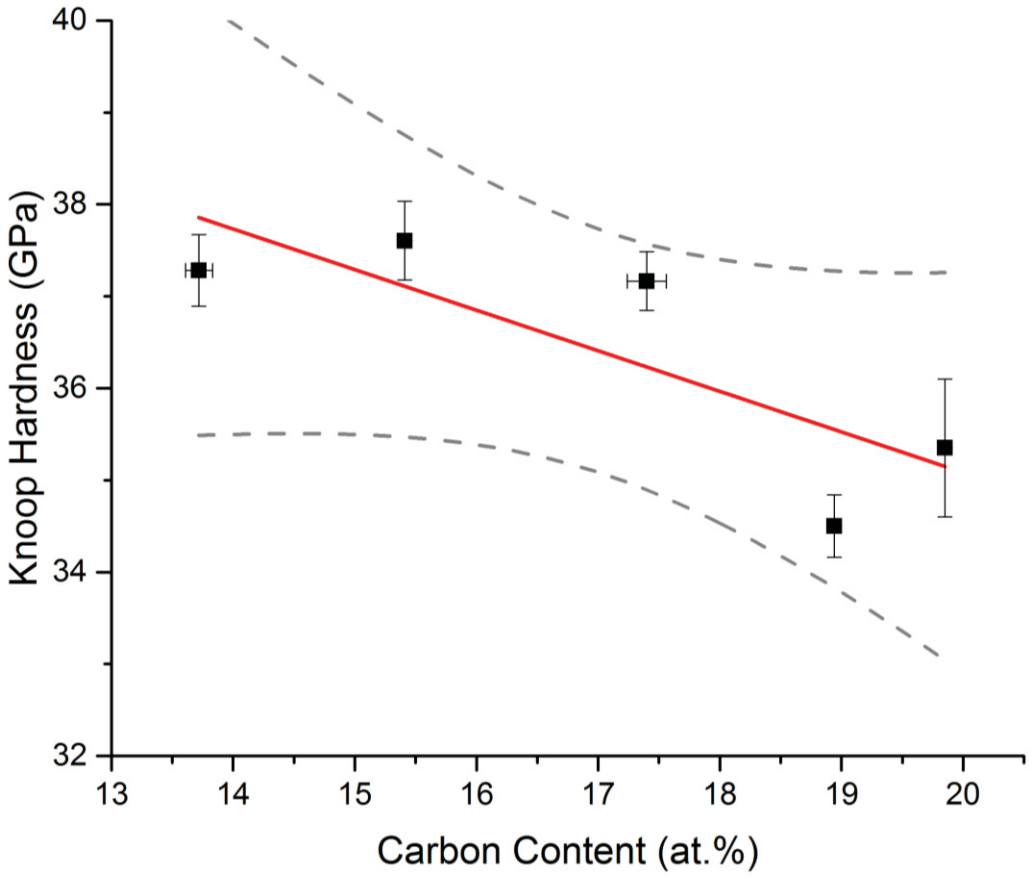

Figure 72. Hardness vs. carbon content.

4.3.3 Instrumented Nano-Indentation

4.3.3.1 Diamond Area Function Optimization

Instrumented nano-indentation is highly dependent upon knowing the area of the diamond indenter that is being used. Therefore, it is important to determine the diamond area function of the indenter which allows for the determination of an accurate indent area. Fused silica was used to establish the diamond area function. Five separate indent arrays were made in the fused silica with 30 indents in each. The load varied from 10 mN (1 g) to 150 mN (15 g) with 5 mN (0.5 g) increases per indent. MicroMaterials NanoTest Vantage software was used to determine the max depth, contact depth, max load and

contact compliance. These values were then used to calculate the diamond area function using polynomial fits with varying degrees until the calculated results were in agreement with the expected results.

Oliver and Pharr's method for determining the area function was done using the following equation:

$$A(h_c) = C_1 h_c^2 + C_2 h_c^1 + C_3 h_c^{\frac{1}{2}} + C_4 h_c^{\frac{1}{4}} + \cdots + C_9 h_c^{\frac{1}{128}} \quad (37)$$

Where the C_1 is a number close to 24.5 and the other fitting constants take into account tip bluntness and other variations from the non-ideal indenter geometry. Using this equation the diamond area function for the fused silica was calculated four different ways,

$$A_1(h_c) = C_1(h_c + x)^2 \quad (38)$$

$$A_2(h_c) = C_1 h_c^2 + C_2 h_c^1 \quad (39)$$

$$A_3(h_c) = C_1 h_c^2 + C_2 h_c^1 + C_3 h_c^{\frac{1}{2}} \quad (40)$$

$$A_4(h_c) = C_1 h_c^2 + C_2 h_c^1 + C_3 h_c^{\frac{1}{2}} + C_4 h_c^{\frac{1}{4}} \quad (41)$$

A_1 uses only the first term in the fit along with a term, x, which is used to describe the tip bluntness. A_2, A_3 and A_4 are variations of the original Oliver and Pharr equation. Figures 73 through 76 show the fits and fit statistics obtained from these equations.

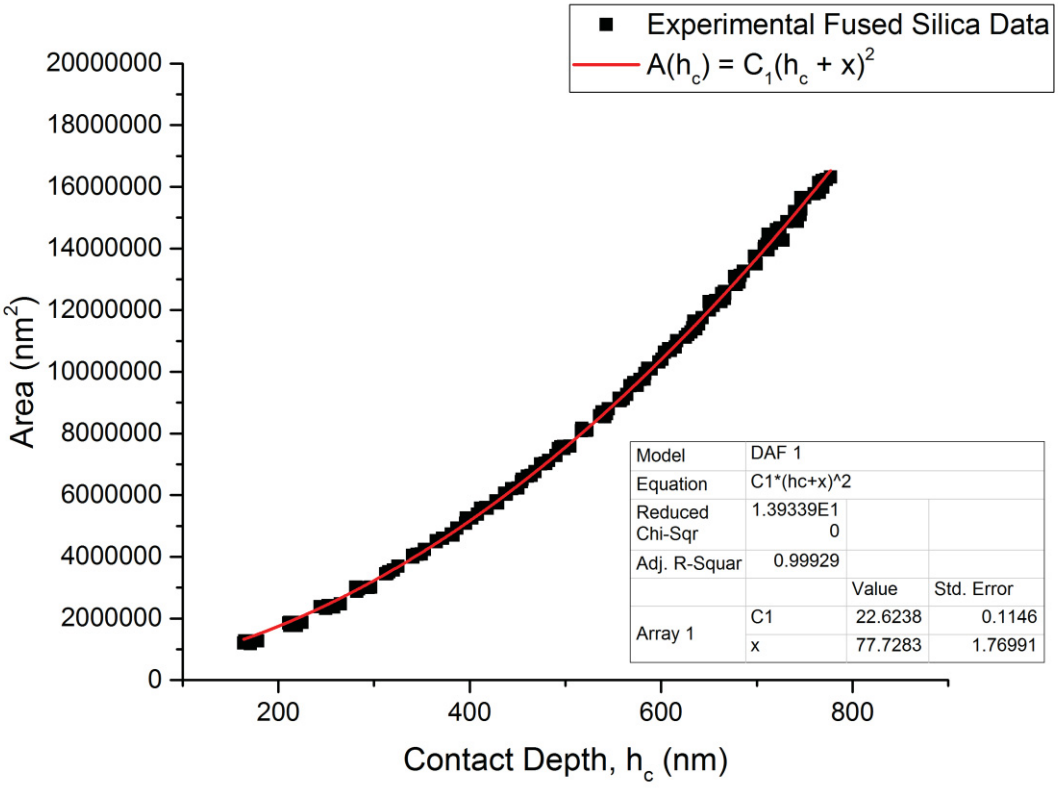

Figure 73. Fit A_1. Only one term was used (C_1) along with x which was used to describe the tip bluntness.

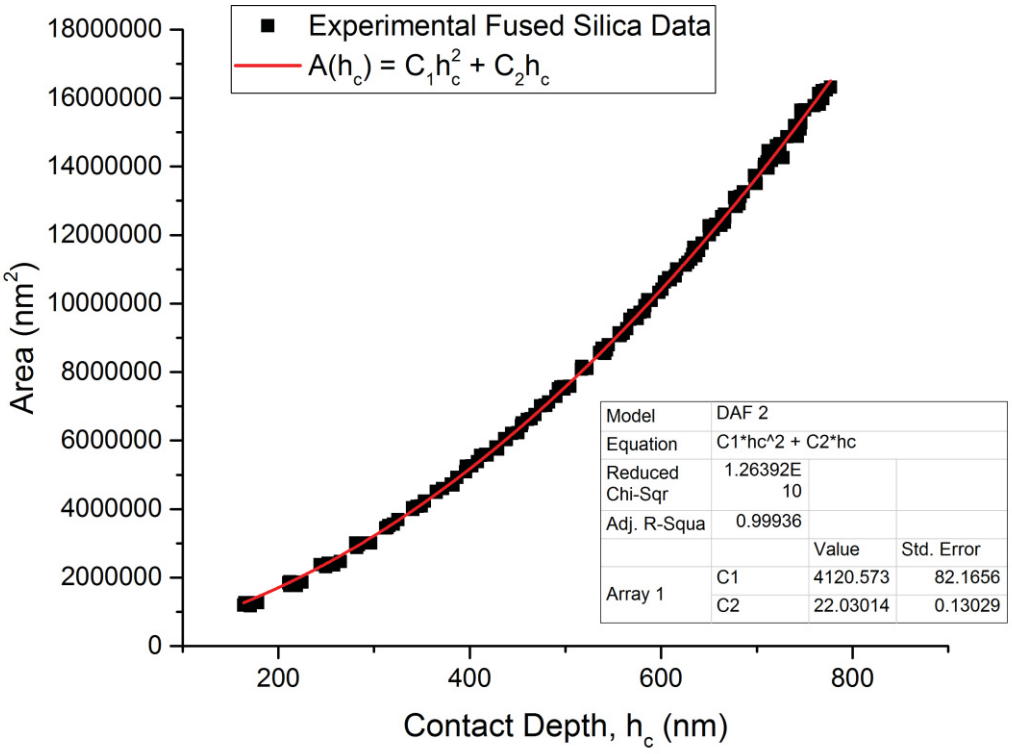

Figure 74. Fit A_2. Two terms (C_1 and C_2) were used for the fit.

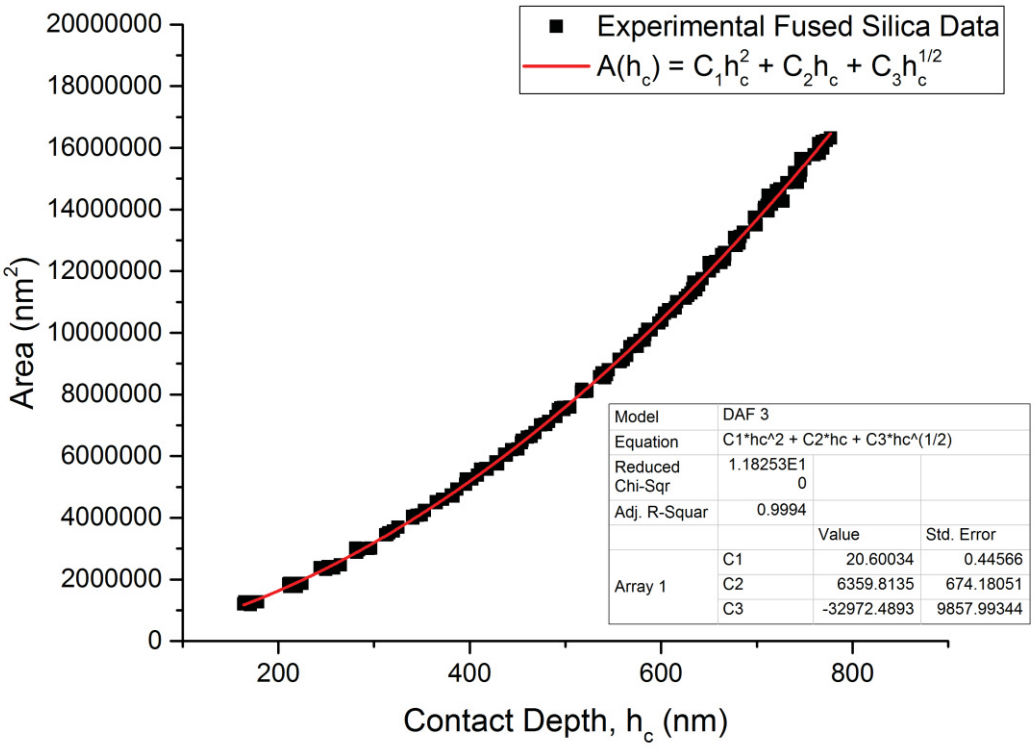

Figure 75. Fit A_3. Three terms (C_1, C_2 and C_3) were used for the fit.

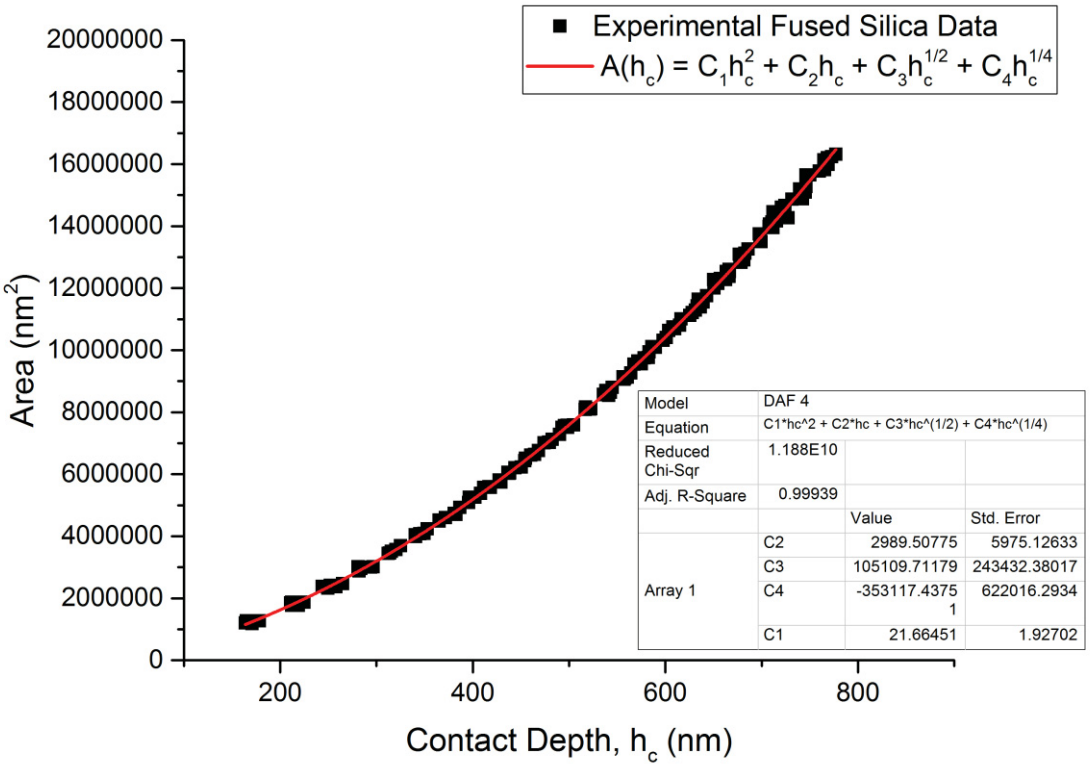

Figure 76. Fit A_4. Four terms (C_1, C_2, C_3, and C_4) were used for the fit.

The r-squared values for the fits show that each equation gives a very accurate fit with no significant variations between the four. However, fit A_4 begins to exhibit large standard errors, eliminating it as possible DAF. Further analysis was needed to determine the best fit out of the remaining equations. To determine the best fit, the fit equations were used to calculate the area, hardness and reduced modulus of the fused silica data. The calculations should result in values of ~8.8 GPa for hardness and 72 GPa for reduced modulus. The calculated values for a single array of indents for each fit are reported in Table 19. While each of the fits gives accurate values, DAF 2 exhibits the smallest standard deviation of all the fits. DAF 2 is also in the same form as the equation used in the NanoTest Vantage software. Therefore, the equation,

$$A_2(h_c) = 22.03014h_c^2 + 4120.5739h_c \quad (42)$$

was used for all further calculation of hardness and reduced modulus.

Table 19. Hardness and reduced modulus results for all four DAF fits. DAF A_2 was determined to be the best fit.

Indent	DAF A_1 Hardness (GPa)	DAF A_1 Reduced Modulus (GPa)	DAF A_2 Hardness (GPa)	DAF A_2 Reduced Modulus (GPa)	DAF A_3 Hardness (GPa)	DAF A_3 Reduced Modulus (GPa)	DAF A_4 Hardness (GPa)	DAF A_4 Reduced Modulus (GPa)
1	7.43	70.18	7.73	71.59	8.32	74.28	8.45	74.85
2	7.69	71.52	7.83	72.16	8.12	73.50	8.13	73.56
3	8.37	72.57	8.45	72.95	8.65	73.80	8.64	73.77
4	8.33	73.22	8.37	73.39	8.47	73.84	8.45	73.77
5	8.44	71.89	8.46	71.95	8.51	72.18	8.49	72.11
6	8.56	72.71	8.56	72.71	8.58	72.81	8.57	72.75
7	8.69	72.58	8.68	72.54	8.69	72.56	8.68	72.51
8	8.59	72.06	8.58	71.99	8.57	71.95	8.56	71.92
9	8.76	72.34	8.74	72.26	8.72	72.19	8.71	72.17
10	8.91	72.11	8.89	72.03	8.86	71.93	8.86	71.92
11	9.09	72.54	9.07	72.45	9.04	72.34	9.04	72.34
12	9.10	72.61	9.08	72.52	9.05	72.41	9.05	72.41
13	9.22	72.74	9.20	72.66	9.17	72.54	9.17	72.55
14	8.90	71.77	8.89	71.69	8.86	71.58	8.86	71.60
15	8.88	71.43	8.87	71.36	8.84	71.26	8.84	71.28
16	9.03	72.19	9.01	72.13	8.99	72.03	8.99	72.05
17	9.11	72.40	9.10	72.34	9.07	72.25	9.08	72.27
18	9.19	72.48	9.18	72.43	9.16	72.35	9.16	72.37
19	9.12	72.35	9.11	72.32	9.10	72.25	9.10	72.27
20	9.04	71.82	9.03	71.79	9.02	71.74	9.02	71.76
21	9.27	72.53	9.26	72.50	9.25	72.46	9.26	72.48
22	9.20	72.79	9.20	72.78	9.19	72.75	9.19	72.76
23	9.23	71.99	9.23	71.99	9.23	71.97	9.23	71.98
24	9.36	72.58	9.36	72.58	9.36	72.57	9.36	72.58
25	9.18	71.79	9.18	71.80	9.18	71.82	9.19	71.83
26	9.28	72.19	9.29	72.21	9.30	72.23	9.30	72.24
27	9.29	72.29	9.29	72.31	9.30	72.35	9.30	72.36
28	9.06	71.37	9.07	71.41	9.09	71.48	9.08	71.47
29	9.26	72.27	9.27	72.31	9.29	72.39	9.28	72.38
30	9.20	71.99	9.22	72.04	9.24	72.13	9.23	72.12
Avg.	***8.89***	***72.18***	***8.91***	***72.24***	***8.94***	***72.40***	***8.94***	***72.41***
Std. Error	***0.09***	***0.10***	***0.08***	***0.08***	***0.06***	***0.13***	***0.06***	***0.14***

4.3.3.2 Berkovich Hardness and Reduced Modulus

Using the diamond area function that was calculated in the previous section, it was possible to determine the Berkovich hardness and reduced modulus of the boron-rich boron carbide samples at varying loads. One major benefit that instrumented nanoindentation has over the Knoop microhardness discussed previously is the instruments low load capability allowing for much smaller indents to be made and analyzed. The smaller indents make it much easier to determine the effects of chemistry on the hardness and modulus in a highly accurate manner.

20 indents were made at five different loads ranging from 100 mN (10 g) to 500 mN (51g) in 100 mN increments. Indents were examined using the optical microscope included in the NanoTest Vantage instrument. Any indents that exhibited anomalous size or shape were excluded from the analysis. Further, any load versus depth curves that contained large deviations from the expected curve (i.e. pop ins) were also excluded from analysis. The load versus depth curves for representative indents at each load for samples 100BC through 65BC-35B are shown in Figures 77 through 81 respectively. The curves show the expected load/unload behavior with no creep at max load.

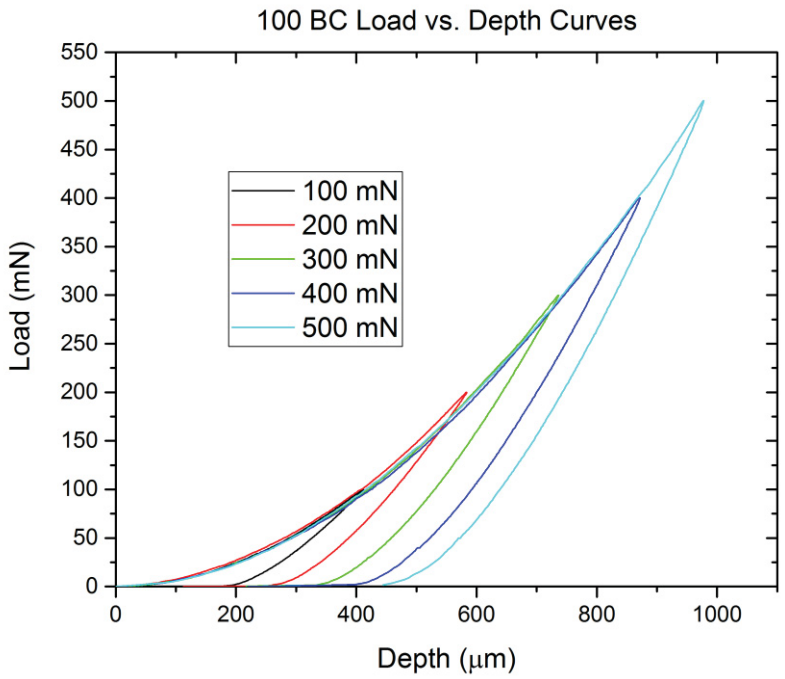

Figure 77. Load-Depth curves for sample 100BC.

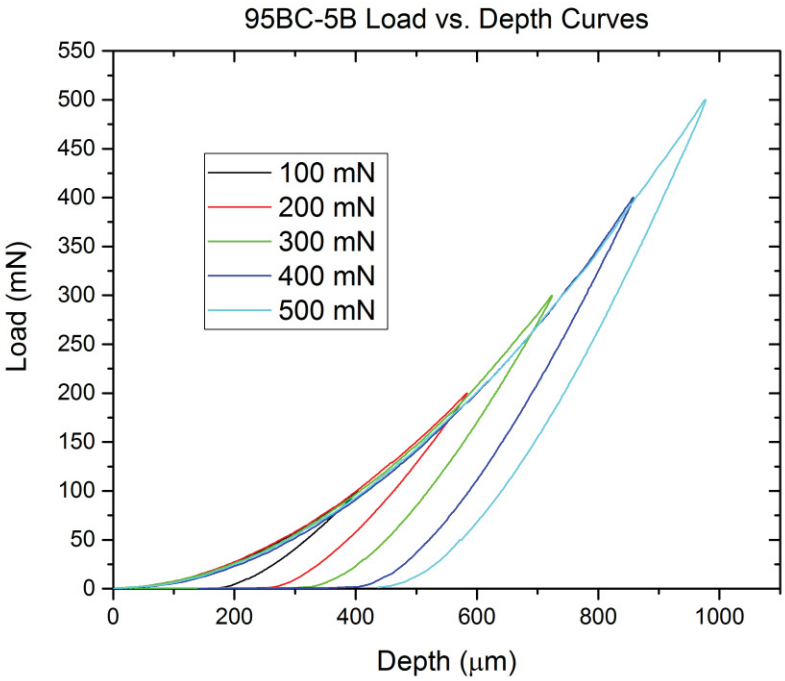

Figure 78. Load-Depth curves for sample 95BC-5B.

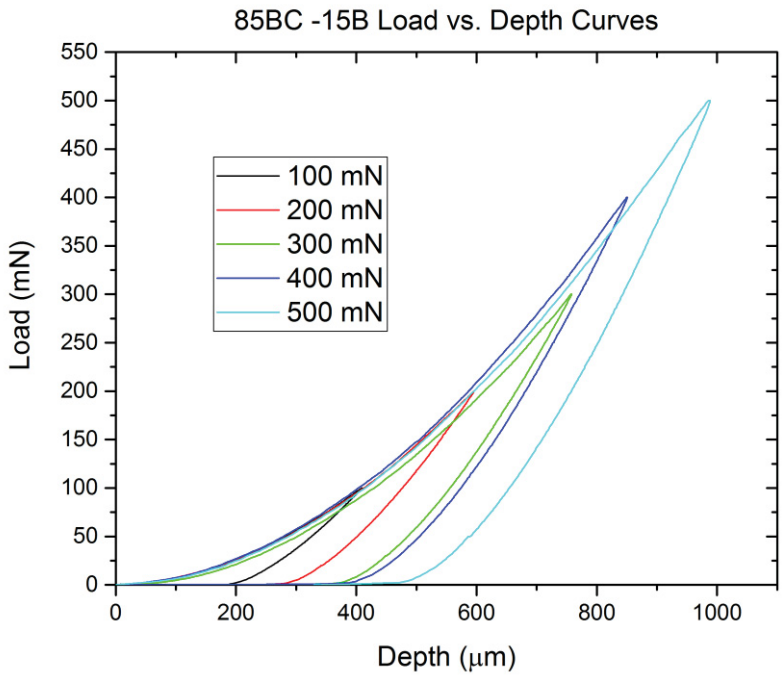

Figure 79. Load-Depth curves for sample 85BC-15B.

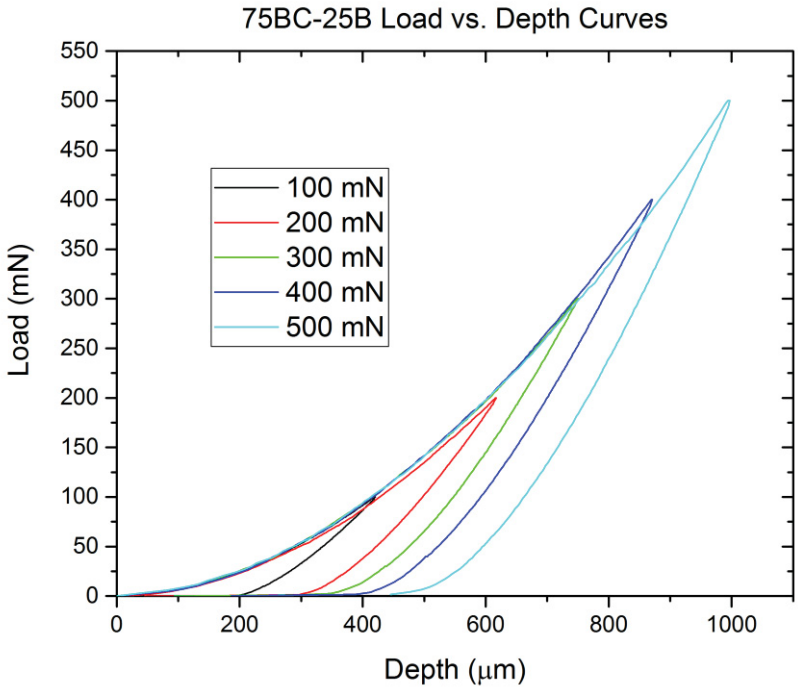

Figure 80. Load-Depth curves for sample 75BC-25B.

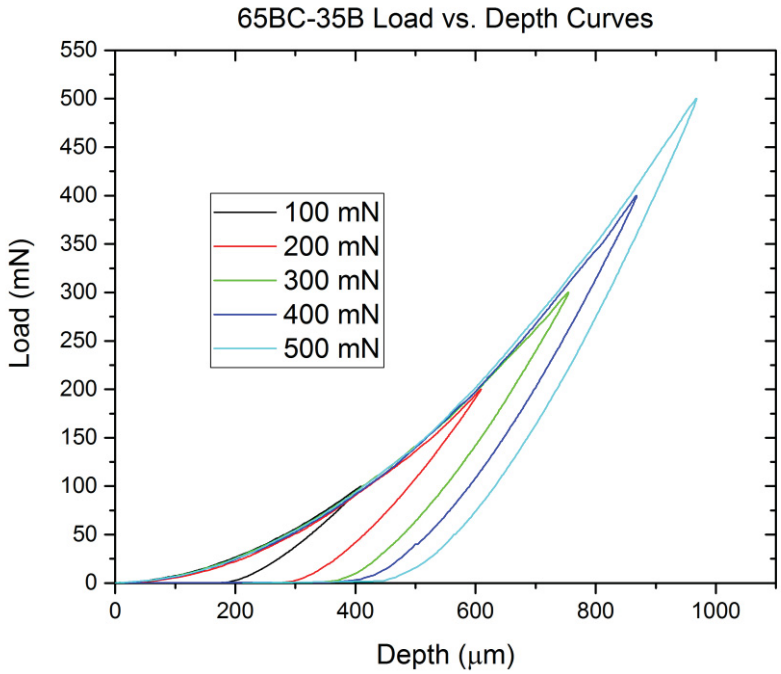

Figure 81. Load-Depth curves for sample 65BC-35B.

Using the diamond area function determined in the previous section, the Berkovich hardness and reduced modulus were determined for each of the 20 indents made at each load. The average of the 20 indents was taken and the resulting values are reported in Table 20. It is expected that the reduced modulus should be nearly constant with load, however, the indentation size effect may still be present in the hardness data at these low loads. Plotting the values of both the hardness (Figure 82) and reduced modulus (Figure 83), it is seen that they are both nearly constant with load (with the exception of a slight decrease in the 100 mN load data). As a check, the 500 mN indents were imaged (Figure 84) using SEM and measured by hand to determine the difference between the actual hardness and the hardness determined from the Oliver and Pharr method. The results are shown in Table 21. While there are differences in the measured values, the overall error is fairly low (with

the exception of sample 100BC). These calculations further verify that the diamond area function that is being used is correct.

Table 20. Berkovich hardness and reduced modulus calculated from the A_2 DAF.

100mN (10 g)	H (GPa)	Std. Error	Reduced Modulus (GPa)	Std. Error
65BC-35B	30.1	0.3	311.3	1.3
75BC-25B	31.3	0.3	320.6	1.1
85BC-15B	31.0	0.3	320.8	1.2
95BC-5B	32.7	0.3	326.1	1.1
100BC	32.2	0.3	324.6	1.0
200mN (20 g)	**H (GPa)**	**Std. Error**	**Reduced Modulus (GPa)**	**Std. Error**
65BC-35B	32.2	0.4	324.1	2.1
75BC-25B	33.2	0.2	330.5	1.0
85BC-15B	32.8	0.4	331.9	1.3
95BC-5B	34.7	0.2	337.4	0.9
100BC	34.4	0.2	337.9	1.0
300mN (30 g)	**H (GPa)**	**Std. Error**	**Reduced Modulus (GPa)**	**Std. Error**
65BC-35B	32.5	0.3	324.6	1.6
75BC-25B	34.7	0.4	336.3	2.0
85BC-15B	34.0	0.3	336.6	1.2
95BC-5B	35.4	0.2	341.0	0.7
100BC	34.7	0.2	338.3	1.1
400mN (41 g)	**H (GPa)**	**Std. Error**	**Reduced Modulus (GPa)**	**Std. Error**
65BC-35B	33.1	0.2	328.7	1.3
75BC-25B	34.8	0.2	339.5	1.0
85BC-15B	34.6	0.2	338.8	1.3
95BC-5B	35.0	0.4	339.6	1.7
100BC	35.2	0.3	341.9	1.1
500mN (51g)	**H (GPa)**	**Std. Error**	**Reduced Modulus (GPa)**	**Std. Error**
65BC-35B	33.0	0.3	326.7	1.8
75BC-25B	34.9	0.3	339.0	1.5
85BC-15B	34.4	0.2	336.8	1.5
95BC-5B	35.0	0.3	338.7	1.5
100BC	35.3	0.3	337.9	1.6

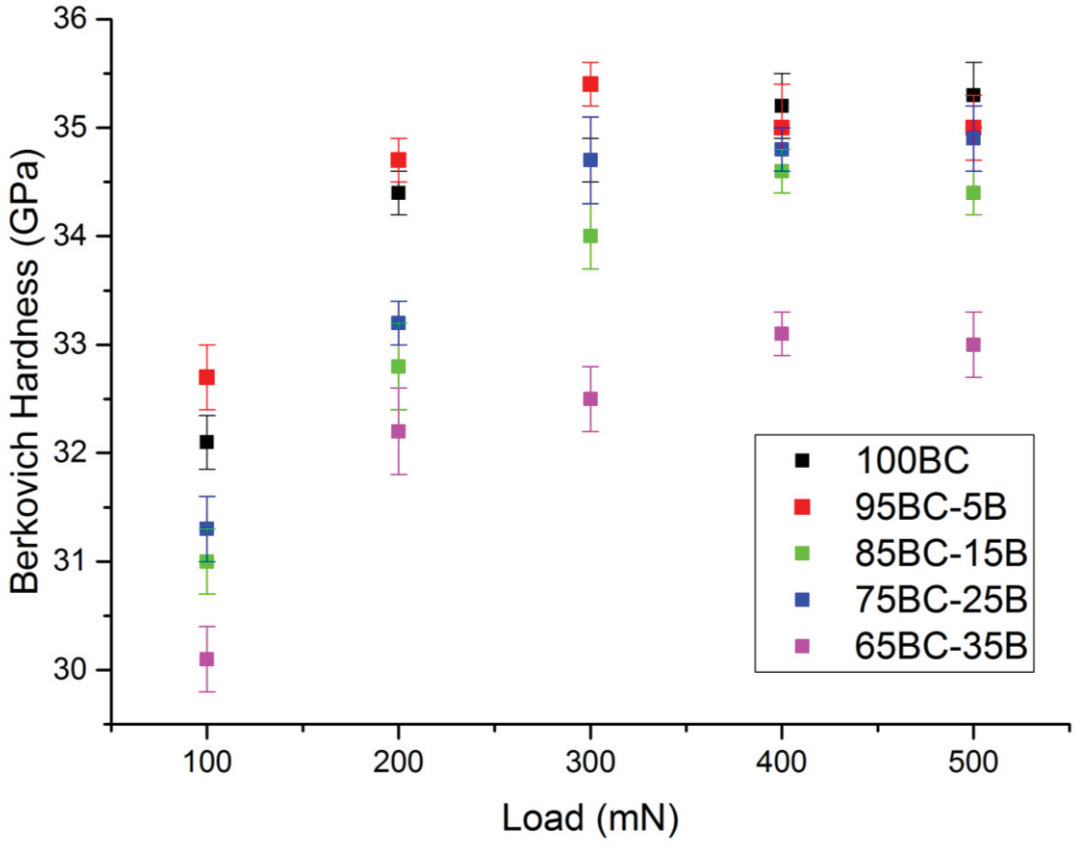

Figure 82. Load-hardness curve for Berkovich nanoindentation.

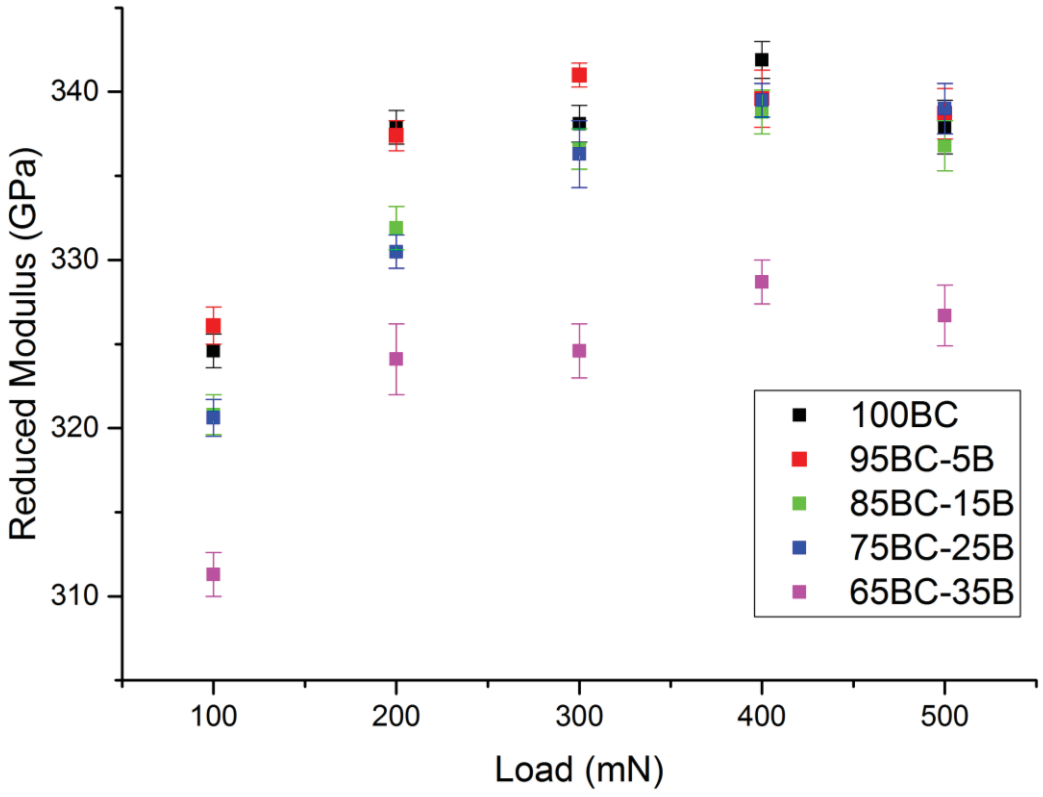

Figure 83. Load-reduced modulus curve for Berkovich nanoindentation.

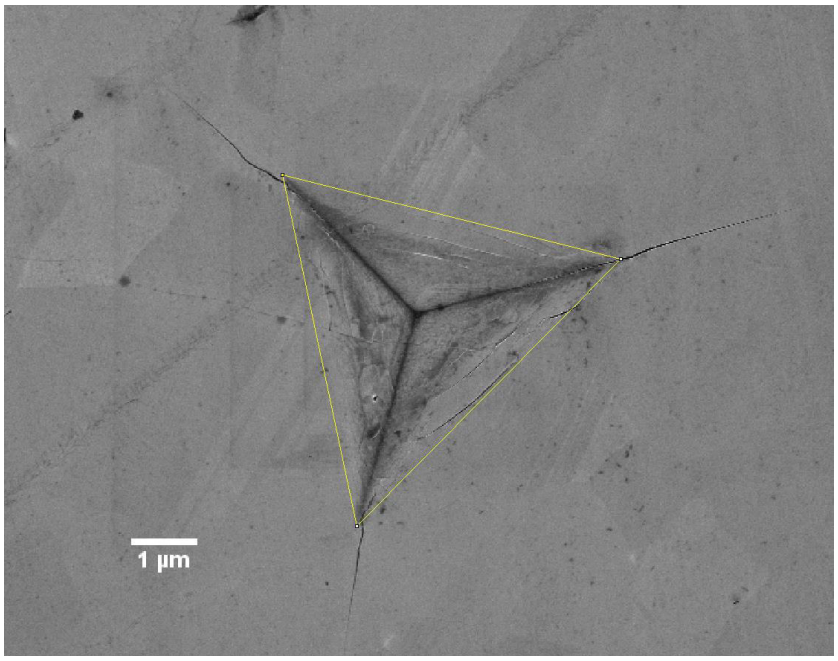

Figure 84. 100 mN indent imaged using SEM. Yellow triangle shows the area that was measured to determine the hardness.

Table 21. The measured hardness (from SEM) and the average difference when compared with the Oliver and Pharr method of determining hardness (Table 20).

Sample	Measured Hardness (GPa)	Std. Dev.	Average Difference from O-P Results
65BC-35B	34.1	1.2	3.0
75BC-25B	35.9	1.3	2.8
85BC-15B	34.1	1.0	3.9
95BC-5B	37.8	1.2	6.6
100BC	40.4	3.2	12.7

Taking the same data from above and plotting the 100 mN hardness versus the carbon content, a clear trend appears (Figure 85). The trend is opposite as to what was

seen with the Knoop hardness values reported previously. The maximum hardness is actually achieved in sample 95BC-5B with sample 100 BC only slightly lower. Moving to lower carbon contents, the hardness begins to drop off from ~32.5 GPa to ~30.3 GPa. Once again, linear regression was used along with the 95% confidence interval to determine whether a dependence was found. The fit equation for the 100 mN hardness was,

$$HB_{100} = (25.2 \pm 1.9) + (0.37 \pm 0.11)[C] \quad (43)$$

This equation shows statistical dependence on the carbon content as the zero slope is not contained within the 95% confidence interval. This trend is very similar to the trend that was reported by Niihara. Unlike the Knoop hardness data which was determined to show little correlation with chemistry, the trend in the Berkovich nanoindentation is likely due to the changes in chemistry. This is due to the fact that the edge length of a 100 mN Berkovich indent is slightly smaller than that of the average grain size exhibited in all of the samples. This implies that the indents should avoid most of the porosity, inclusions, grain boundaries and other mechanisms that may affect the measurement. The 500 mN results were also plotted against the carbon content to determine if there was a similar trend in the data (Figure 86). The fit equation for the 500 mN hardness was,

$$HB_{500} = (29.3 \pm 2.0) + (0.30 \pm 0.12)[C] \quad (44)$$

Once again, the equation shows statistical dependence. While the 500 mN indents are larger than the 100 mN indents, they are still very small and will likely only encounter grain boundaries.

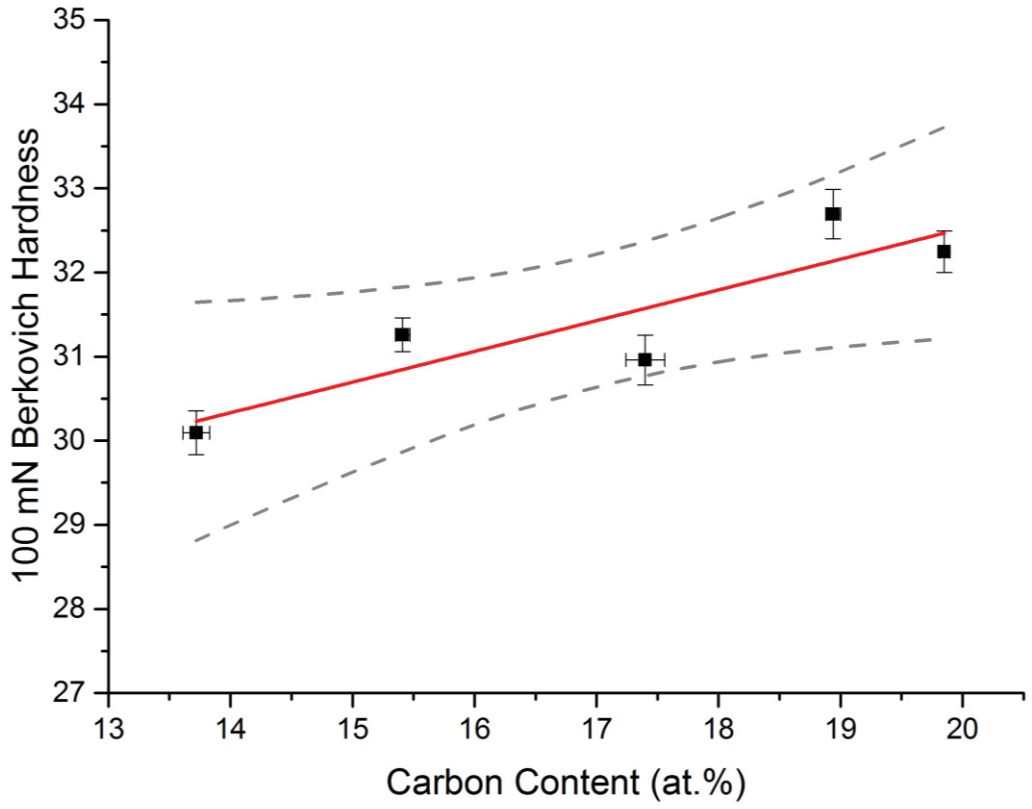

Figure 85. Effect of the change in the carbon content on the 100 mN Berkovich hardness.

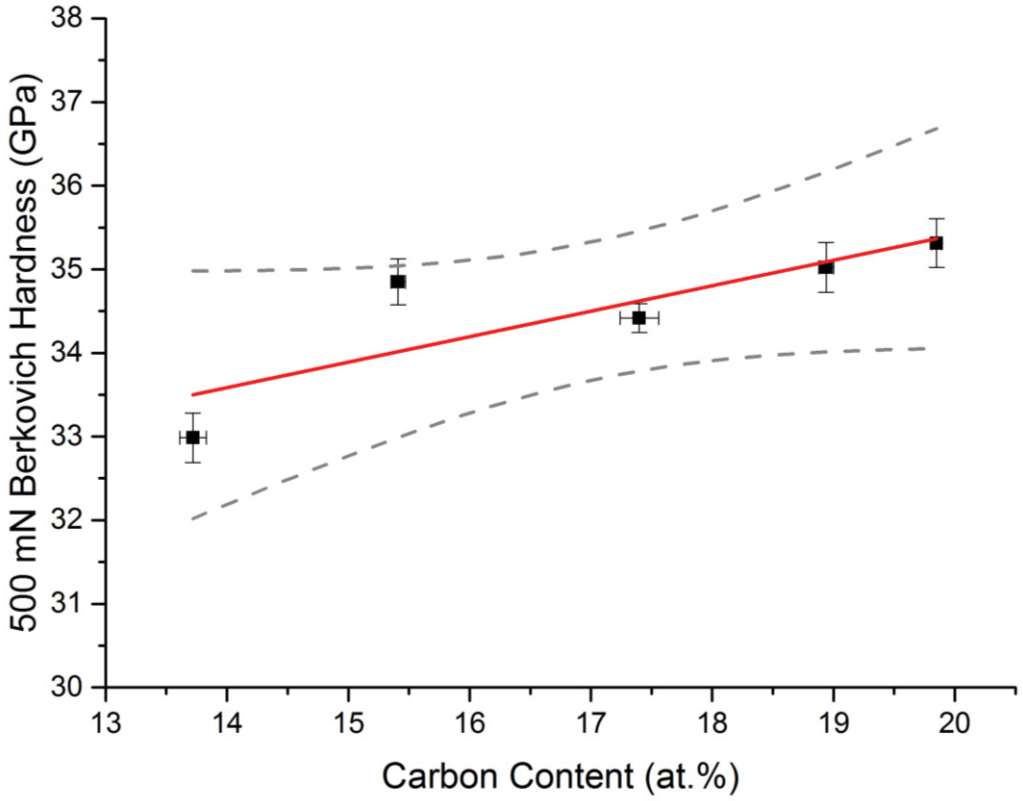

Figure 86. Effect of the change in the carbon content on the 500 mN Berkovich hardness.

To further verify this trend, a series of 50 indents were done on the etched samples. Each indent was imaged and the indents that were found to fall squarely in a grain were measured. Figure 87 is an example of an indent that would be included in the measurement. The results are shown in Table 22. It is important to note that the number of indents included in the calculations varied from sample to sample, the number of total indents measured is recorded in column 4 of Table 22. Once again, a decrease in hardness with decreasing carbon content is seen. The fact that nearly all possible mechanisms have been eliminated in these calculations leads to the conclusion that the decrease is in fact due to the changing chemistry. Sample 100BC was not included in this analysis as the slightly

smaller grain size made it difficult to make a statistically significant amount of indents within the grains.

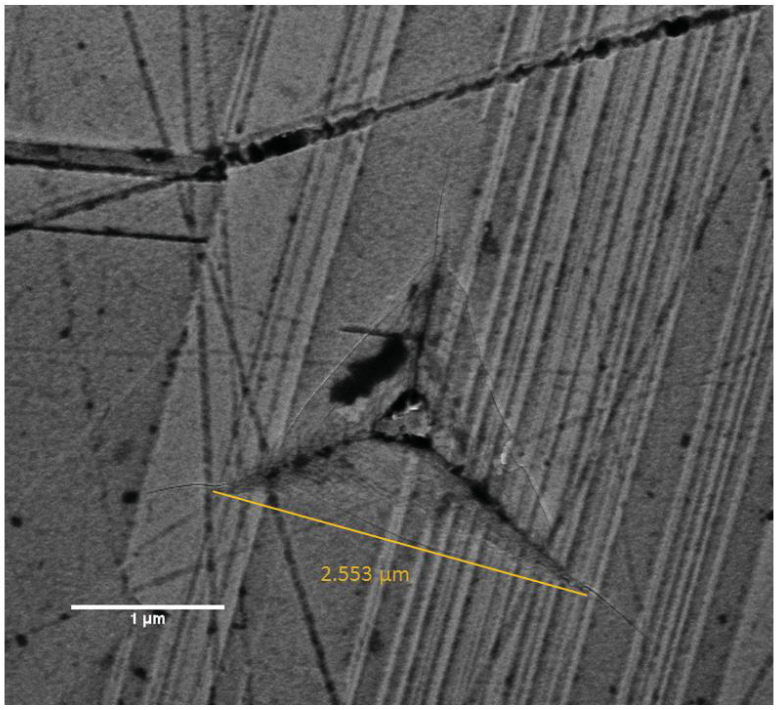

Figure 87. Indent on etched sample (95BC-5B). Indent falls completely within the grain, eliminating effects of grain boundaries, porosity, inclusions, etc..

Table 22. Single grain Berkovich hardness.

Sample	Berkovich Hardness (GPa)	Std. Error	# of Indents
65BC-35B	39.5	1.0	10
75BC-25B	38.0	0.7	9
85BC-15B	42.1	0.6	9
95BC-5B	41.5	0.7	19

The reduced modulus can be converted to the Young's modulus by using equation 25 in Section 3.3.2. This equation takes into account the reduced modulus and Poisson's ratio of the diamond indenter, which are known, and the Poisson's ratio of the material

which was measured using ultrasound NDE and reported in Table 23. While the data trend does not change with the conversion from reduced modulus to Young's modulus, the conversion was used to compare the ultrasound results with the indentation results. Once again, sample 100BC is excluded due to the fact that the Poisson's ratio was not able to be measured. The results are shown in Table 23. The % difference between the measurements from ultrasound and the results from nanoindentation are very small.

Table 23. Comparison of Young's modulus measured by ultrasound NDE and nano-indentation.

Sample	E (GPa)	500 mN Elastic Modulus	% Difference
65BC-35B	424	437	3
75BC-25B	434	462	6
85BC-15B	442	460	4
95BC-5B	456	466	2
100BC	---	---	---

4.3.3.3 Fracture Toughness

Fracture toughness was determined by measuring the crack lengths emanating from the 500 mN (51 g) Berkovich indents as described in section 3.3.2. Once again, a decrease in the fracture toughness with decreasing carbon content is observed (Table 24 and Figure 88). The values calculated show good correlation with the typical fracture toughness values reported in the literature. As with the other mechanical properties measured, fracture toughness shows a statistical dependence on chemistry. The linear fit equation was,

$$K_{IC} = (2.0 \pm 0.1) + (0.040 \pm 0.004)[C] \quad (45)$$

Figure 84 is an example of an indent that was measured for fracture toughness. The cracks emanating from the indent are very straight indicating that there was no deflection along the way. Therefore, the fracture is trans-granular as expected for boron carbide. The straight cracks are exhibited in each sample, confirming that the changing chemistry does not affect the fracture mode for boron carbide.

Table 24. Indentation fracture toughness measured using 500 mN indents.

Sample	Fracture Toughness ($MPa.m^{1/2}$)	Std. Error
65BC-35B	2.57	0.02
75BC-25B	2.6	0.02
85BC-15B	2.7	0.03
95BC-5B	2.8	0.02
100BC	2.8	0.04

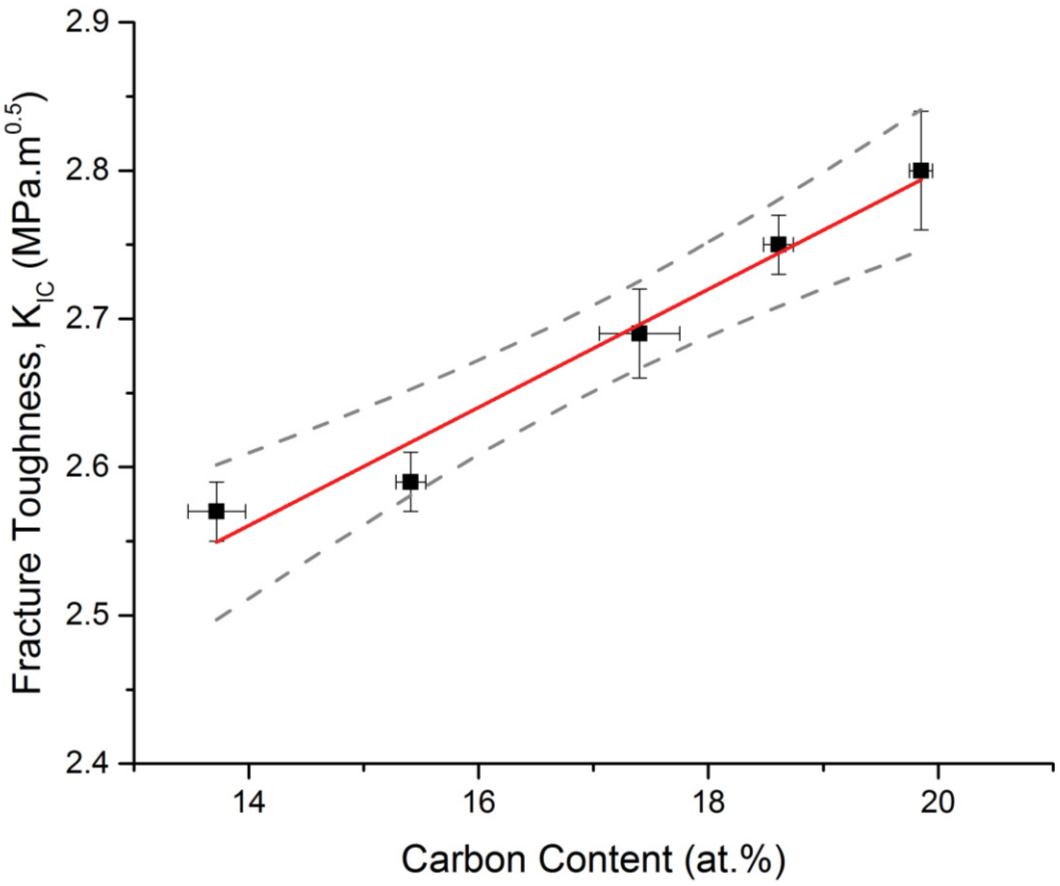

Figure 88. Effect of the changing carbon content on the indentation fracture toughness.

4.3.4 Raman Microspectroscopy Analysis of Knoop Indents

Boron carbide has been shown to exhibit amorphous regions within both micro and nano indents. This is typically referred to as pressure-induced amorphization, and it is believed that this amorphization may potentially be a cause of the anomalous behavior exhibited in boron carbide. Modeling work by An *et al*. has shown that the elimination of the B-C inter-icosahedral bond eliminates the problem of amorphization seen in their models. As the boron carbide becomes more boron-rich, in theory, more and more of these B-C inter-icosahedral bonds should be replaced with B-B bonds. At approx. 13.3 at. % the majority of the bonds should be B-B. Therefore, by examining the Knoop indents for the

presence of amorphization it should become clear if the changes in chemistry do indeed affect the degree of amorphization.

Raman microspectroscopy was used to analyze the well known Raman bands for amorphous material at ~1300 cm^{-1}, 1500 cm^{-1} and 1800 cm^{-1}. Point scans were used to determine the presence of amorphous bands in every indent of the samples. Figure 89 shows the resulting Raman spectra. For samples 100BC through 75BC-25B, the amorphous Raman bands are very clear, with counts much higher than the boron carbide Raman band at 1080 cm^{-1}. Sample 65BC-35B, on the other hand, shows a significantly lower intensity Raman band. Each spectra shown in Figure 89 is a representative spectra for each sample. To ensure that the spectra for 65BC-35B were not an anomaly, the spectra for each indent is shown in Figure 90. Once again, the amorphous Raman bands are much lower in intensity with some of the indents showing little to no amorphous signature.

To further examine the amorphization present in the indented samples, Raman area maps were performed on individual indents. Using the area maps, it was possible to plot the normalized intensity (number of normalized counts at the peak of the 1800 cm^{-1} band minus the background) of the 1800 cm^{-1} Raman band (most de-convoluted amorphous Raman band), which could be used to determine the extent of the amorphization under the indent became evident. The intensity was once again determined by fitting the 1800 cm^{-1} peaks as described in section 4.2.8. The resulting maps are shown in Figure 91. The dashed black lines show the location of the indent. While each indent shows some degree of amorphous character, there is a clear decrease in the extent of the amorphization as the carbon content is decreased. Once again, this is predicted by the model developed by An *et al.* as the carbon content is decreased, more and more B-C bonds are substituted with B-

B bonds which lead to the disappearance of the amorphization. Samples 60BC-40B and 55BC-45B were not able to be examined due to the large degree of porosity making it difficult to obtain reliable results. It would be expected, however, that the level of amorphization would continue to decrease. While this work shows that it is possible to decrease the amorphization in boron carbide by altering the chemistry, it is not likely that the amorphization can be completely eliminated due to the fact that at any given chemistry boron carbide can contain many different atomic configurations.

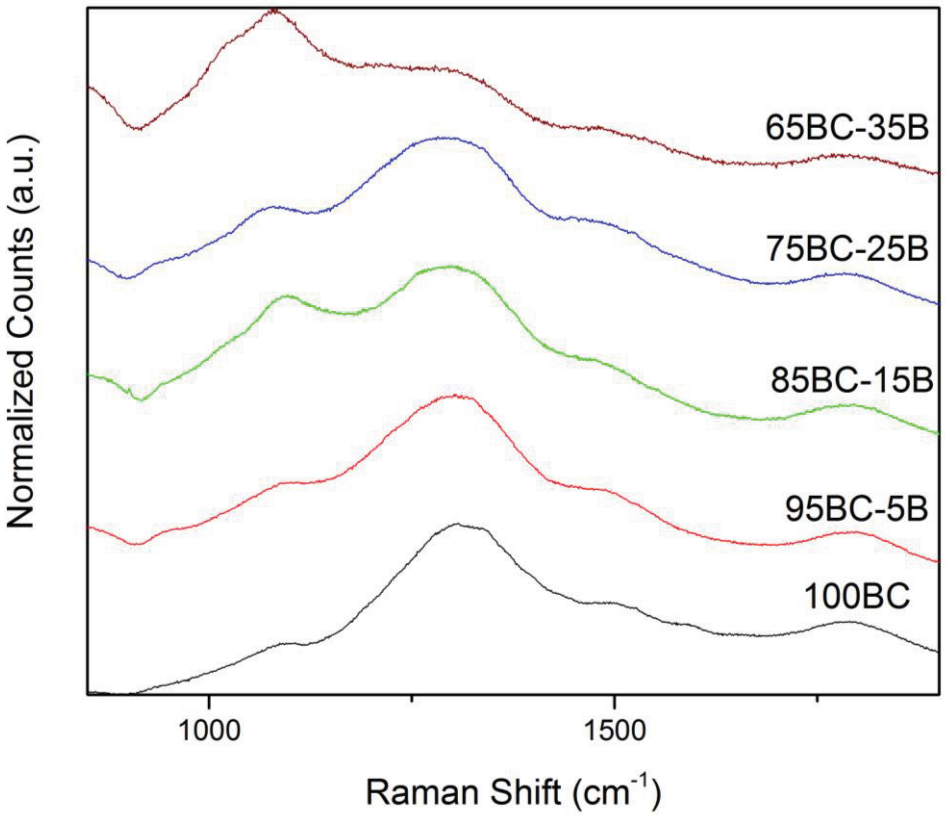

Figure 89. Raman spectra of amorphous bands present within 1 kg Knoop indents.

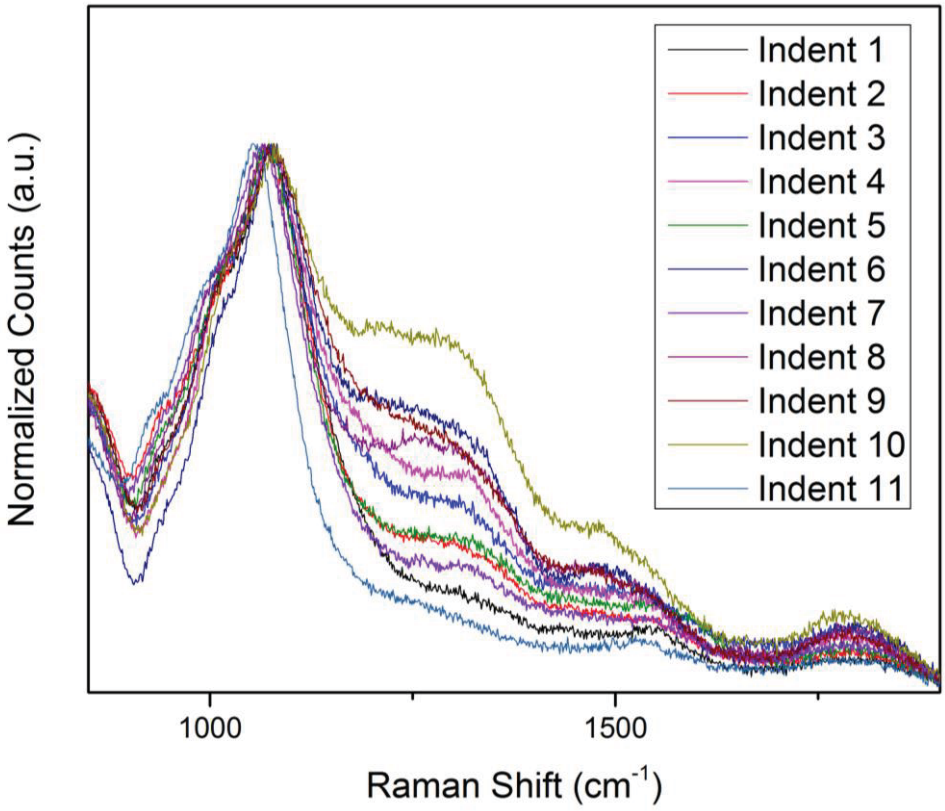

Figure 90. All 11 spectra collected from indents on sample 65BC-35B. Amorphous signature is significantly lower than the other, less boron-rich samples.

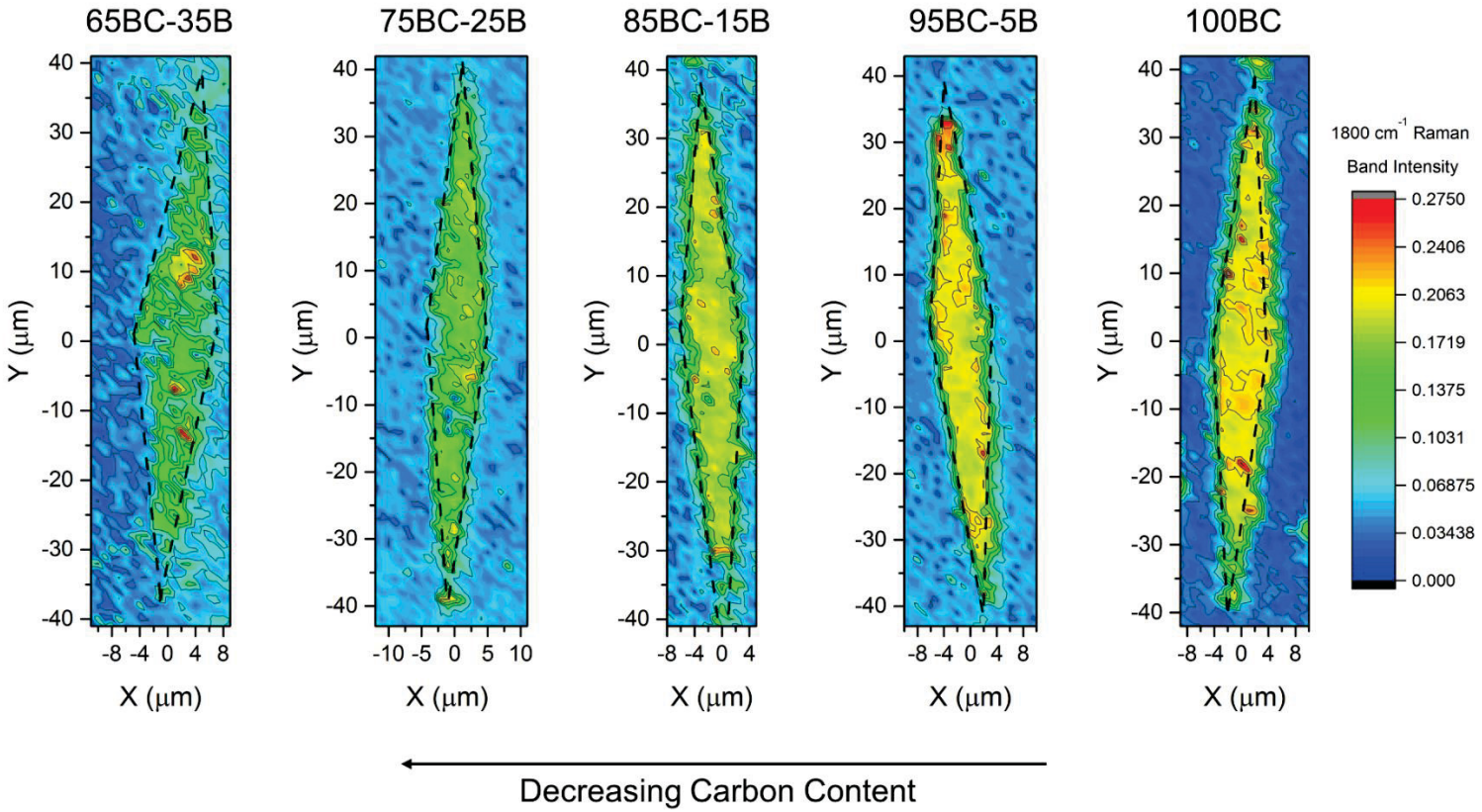

Figure 91. . Raman area maps of the intensity of the 1800 cm^{-1} Raman band. Intensity and extent of the amorphous band at 1800 cm^{-1} drops significantly with decreasing carbon content.

5. Conclusions

Through extensive characterization of boron carbide powders and densified boron-rich boron carbides, the following conclusions can be made:

1. **POWDER-** High purity boron carbide powder was successfully synthesized using the rapid carbothermal reduction method. X-ray diffraction analysis revealed the presence of only a small of amount of free carbon (~0.2 wt. %) and no other impurity phases. The chemical analysis further revealed these powders had B:C ratios near the expected B_4C stoichiometry as the temperatures employed were not sufficient enough to synthesize boron-rich powders. Powder morphology and grain size were consistent from batch to batch and variations in powder chemistry were negligible.
2. **DENSIFICATION-** Through the use of spark plasma sintering and amorphous boron additions, near fully dense boron carbide with varying stoichiometries were produced. A few conclusions were made as follows;
    a. Amorphous boron additions aided in sintering due to the reactions with the small amounts of free carbon present in the starting powder. Porosity measurements show a decrease in the porosity as the carbon content decreased to ~13 at.%. Furthermore, the x-ray diffraction patterns show the disappearance of the small carbon peak with boron additions.
    b. Samples below 13 at.% carbon were difficult to produce using spark plasma sintering. Preliminary work has indicated a potential cause to be the high heating rates that are employed and the inaccuracy in measuring the internal die temperatures. The amorphous boron/boron carbide reaction cannot proceed to completion due to the high heating rates ultimately leading to the amorphous

boron melting out of the graphite dies. This loss in amorphous boron causes the dense sample chemistry to vary significantly from the theoretical calculations.

c. Sample chemistries showed small and consistent deviation from the theoretical values due to the loss of boron to reactions with the SPS dies. Samples 60BC-40B and 55BC-45B exhibited larger deviations due to the loss of boron to melting likely due to inaccuracies in temperature measurements in the SPS.

d. Microstructural analysis shows homogeneous samples across a large segment of the solubility range (>13 at.%) C of the B-C phase diagram were produced. Samples exhibited similar grain structures and size.

e. Sintered samples were phase pure and showed no small scale inclusions or grain boundary phases. X-ray diffraction patterns exhibited no secondary phases. HRTEM analysis showed very clean grain boundaries and triple junctions, which is significantly different from characteristics of commercial materials.

f. Raman microspectroscopy validated the chemistry changes determined using x-ray diffraction and carbon determination. Samples exhibited a high degree of chemical homogeneity as determined by the 480 cm^{-1} and 530 cm^{-1} Raman bands. The icosahedra breathing mode (1080 cm^{-1}) shifted to lower wavenumber as expected with the substitution of boron for carbon within the icosahedra. The appearance of a new Raman band at 370 cm^{-1} at low carbon content (< 14 at. %) indicates a further change in the chain structure.

3. **MECHANICAL PROPERTIES-** The measured static mechanical properties show statistical dependence on the chemistry of the boron carbide phase.

a. Ultrasound non-destructive evaluation measurements exhibited a decrease in the longitudinal and transverse wave speeds through boron carbide with decreasing carbon content. This decrease in the wave speeds is responsible for the decrease in the elastic moduli with decreasing carbon content seen in the reported data.

b. Knoop microhardness exhibited a trend as the hardness was shown to slightly increase with decreasing carbon. However, porosity and grain growth in sample 100BC and 95BC-5B, respectively, caused the hardness values to drop. Taking into account the effects of porosity and grain growth would likely cause the Knoop hardness to be independent of the carbon content.

c. An effect on hardness with the changing chemistry is reported for low load nano-indentation. 100 mN Berkovich indents placed in single grains of boron-rich boron carbide have exhibited a clear decrease in hardness with decreasing carbon content. The nano-indentation data over the load range of 100 mN to 500 mN exhibits no indentation size effect.

d. Fracture toughness determined by measuring the crack lengths of the 500 mN indents reveal a similar trend to that of the hardness. Overall fracture toughness results were in the range of reported fracture toughness values. The cracking emanating from the tips of the indent showed no change from the trans-granular fracture typically exhibited in boron carbide.

4. **AMORPHIZATION-** The extent and intensity of the amorphous region as decreases appreciably with the decrease in carbon content.

a. Raman point scans on 1 kg Knoop indents showed the presence of amorphization in all samples (60BC-40B and 55BC-45B were not tested due to porosity). Sample 65BC-35B, however, exhibited much lower intensity Raman bands.
b. Raman area maps on 1 kg Knoop indents showed an appreciable change in the extent of the amorphization. Amorphous bands were present within the indents of each sample, however, as the carbon content decreased so too did the presence of the Raman bands. Further, the bands were typically much lower in intensity than those of the samples with high carbon content.

6. Future Work

1. Conduct further characterization of the amorphous zone under 1 kg Knoop indents. While it was shown in Objective 3 that the amount of amorphization exhibited in 1 kg Knoop indents decreased with decreasing carbon content, further confirmation is needed. Techniques such as FIB lift out and polishing along with electron microscopy techniques will be needed to examine the damaged zone under the Knoop indents for amorphous regions. Further Raman analysis of this damaged region will allow for a better understanding of the extent of amorphization.
2. Conduct experiments to gain a better understanding of the SPS temperature. It has been seen in this work that amorphous boron melts at a measured SPS temperature of 1900°C. This suggests that the method of temperature measurement does not give an accurate measure of the temperature within the SPS die. Therefore, determination of the temperature differences is need to ensure that material melting points and eutectics are not being surpassed. Determination of the SPS temperature will be done using a customized crucible set-up with a material of known melting point. SPS temperatures will be varied and the material will be examined for artifacts of melting. This measurement will determine the temperature difference between measured temperature and the temperature within the die.
3. Transition sample processing from SPS to hot press and hot isostatic press (HIP). Two issues were encountered in this work; sample size limitations and melting of amorphous boron. By transitioning from the SPS system to a

technique such as hot pressing or HIP'ing should help to eliminate both of these issues. Sample size limitations are not encountered in the more conventional hot press and HIP techniques. Larger sample sizes will allow for more characterization to be carried out on each sample, as well as allow for a wider variety of characterization techniques to be used (fracture toughness, compressive strength and dynamic experiments). Along with the capability of larger samples sizes, the temperature is easier to control and measure as there is no current passing through the sample. However, achieving near theoretical densities in hot pressing is often times very difficult. Therefore, processing parameter optimization will have to be performed to ensure that sample quality is at or near the quality of samples reported in this work.

4. Perform dynamic experiments to determine how boron rich materials perform under high strain-rates and pressures. All results reported in this work are static properties of boron carbide. However, dynamic properties are also of great interest to the boron carbide community. Therefore, boron-rich samples will be analyzed using high strain-rate/high pressure experiments. These analyses will provide information on compressive strength, fracture characteristics, crack propagation and amorphization.
5. Optimize boron carbide synthesis parameters to allow for the synthesis of boron-rich boron carbide powders. As discussed previously, boron-rich boron carbide powders are difficult to synthesize due to the high temperatures and boric contents needed. Synthesis of boron-rich powders is the route that would be the most commercially feasible as the cost of amorphous boron makes the

processing route very costly. Therefore, optimization of the current synthesis parameters will be done in attempt to synthesize boron-rich boron carbide powders using a new RCR reactor installed at Rutgers. This work will include varying temperatures and amount of excess boron oxide as well as parameters such as feed rates, run time and residence time. The new reactor will allow not only give more control over the synthesis parameters but it will allow for increased production efficiency.

7. References

1. F. Thévenot, "Boron carbide—a comprehensive review," *Journal of the European Ceramic Society,* 6[4] 205-25 (1990).
2. M. Bouchacourt and F. Thevenot, "The Properties and Structure of the Boron Carbide Phase," *Journal of Less-Common Metals,* 82 9 (1981).
3. A. Suri, C. Subramanian, J. Sonber, and T. Murthy, "Synthesis and consolidation of boron carbide: a review," *International Materials Reviews,* 55[1] 4-40 (2010).
4. M. Chen, J. W. McCauley, and K. J. Hemker, "Shock-Induced Localized Amorphization in Boron Carbide," *Science,* 299[5612] 1563-66 (2003).
5. D. E. Grady and J. L. Wise, "Dynamic properties of ceramic materials," pp. 54. in., 1993.
6. W. Rafaniello and W. G. Moore, "Producing boron carbide." in. Google Patents, USA, 1989.
7. M. F. Toksoy, "Densification of Rapid Carbothermal Synthesized and Commercial Boron Carbide by Spark Plasma Sintering." in Materials Science and Engineering, Vol. Ph.D. Rutgers University, New Brunswick, 2014.
8. K. Niihara, A. Nakahira, and T. Hirai, "The Effect of Stoichiometry on Mechanical Properties of Boron Carbide," *Journal of the American Ceramic Society,* 67[1] C-13-C-14 (1984).
9. B. Champagne and R. Angers, "Mechanical Properties of Hot-Pressed B-B4C Materials," *Journal of the American Ceramic Society,* 62[3-4] 149-53 (1979).
10. J. H. Gieske, T. L. Aselage, and D. Emin, "Elastic Properties of Boron Carbides,″ pp. 4 Vol. 231. *American Institute of Physics*, (1990).
11. P. Larsson, N. Axen, and S. Hogmark, "Improvements of the microstructure and erosion resistance of boron carbide with additives," *Journal of materials science,* 35[14] 3433-40 (2000).
12. M. Chheda, J. Shih, C. Gump, and A. Weimer, "Synthesis and Processing of Boron-Rich Boron Carbide.", 2008.
13. N. Vast, J. M. Besson, S. Baroni, and A. Dal Corso, "Atomic structure and virbrational properties of icosahedral a-boron and B_4C boron carbide," *Computational Materials Science* 17 6 (2000).
14. V. Domnich, S. Reynaud, R. A. Haber, and M. Chhowalla, "Boron Carbide: Structure, Properties, and Stability under Stress," *Journal of the American Ceramic Society,* 94[11] 3605-28 (2011).
15. G. Fanchini, J. W. McCauley, and M. Chhowalla, "Behavior of disordered boron carbide under stress," *Physical Review Letters,* 97[3] (2006).
16. D. R. Tallant, T. L. Aselage, A. N. Campbell, and D. Emin, "Boron carbide structure by Raman spectroscopy," *Physical Review B,* 40[8] 5649-56 (1989).
17. K. Shirai and S. Emura, "Lattice Vibrations of Boron Carbide," *Journal of Solid State Chemistry,* 133 4 (1997).
18. N. Vast, J. M. Besson, S. Baroni, and A. Dal Corso, "Atomic structure and virbrational properties of icosahedral a-boron and B_4C boron carbide," *Computational Materials Science,* 17 6 (2000).

19. H. Werheit, H. W. Rotter, F. D. Meyer, H. Hillebrecht, S. O. Shalamberidze, T. G. Abzianidze, and G. G. Esadze, "FT-Raman Spectra of isotope-enriched boron carbide," *Journal of Solid State Chemistry,* 177 6 (2004).
20. T. L. Aselage and R. G. Tissot, "Lattice Constants of Boron Carbides," *Journal of the American Ceramic Society,* 75[8] 2207-12 (1992).
21. R. P. Elliot, "The Boron-Carbon System." in. Armour Research Foundation of Illinois Institute of Technology, Chicago, 1961.
22. M. Beauvy, "Stoichiometric limits of carbon-rich boron carbide phases," *Journal of the Less Common Metals,* 90[2] 169-75 (1983).
23. K. A. Schwetz and P. Karduk, "Investigation in the boron-carbon system with the aid of electron probe microanalysis," *Journal of Less-Common Metals,* 175 11 (1991).
24. L. B. Ekbom and C. O. Amundin, "MICROSTRUCTURAL EVALUATION OF SINTERED BORON CARBIDES WITH DIFFERENT COMPOSITIONS,″ pp. 237-43 in Science of Ceramics. Vol. 11.
25. M. Bouchacourt and F. Thevenot, "The Properties and Structure of the Boron Carbide Phase " *Journal of Less-Common Metals,* 82 9 (1981).
26. R. R. Ridgeway, "Boron carbide and method of making the same." in. Google Patents, 1933.
27. A. W. Weimer, W. G. Moore, R. P. Roach, J. E. Hitt, R. S. Dixit, and S. E. Pratsinis, "Kinetics of carbothermal reduction synthesis of boron carbide," *Journal of the American Ceramic Society,* 75[9] 2509-14 (1992).
28. A. W. Weimer, "Thermochemistry and Kinetics," pp. 79-113. in Carbide, nitride and boride materials synthesis and processing**.** Edited by A. W. Weimer. Springer, 1997.
29. W. S. WIlson and P. J. Guichelar, "Electric Arc Furnace Process," pp. 132-33. in Carbide, nitride and boride materials synthesis and processing**.** Edited by A. W. Weimer. Springer, 1997.
30. J. J. Scott, "Arc furnace process for the production of boron carbide." in. Google Patents, 1964.
31. S. Miller, F. Toksoy, W. Rafaniello, and R. Haber, "Submicron Boron Carbide Synthesis through Rapid Carbothermal Reduction," pp. 195-207. in Advances in Ceramic Armor VIII**.** John Wiley & Sons, Inc., 2012.
32. K. Yamada, "Boron Carbide Particles Formed from an Amorphous Boron/Graphite Powder Mixture Using a Shock-Wave Technique," *Journal of the American Ceramic Society,* 79[4] 1113-16 (1996).
33. S. T. Benton and R. David, "Method for preparing boron-carbide articles." in. Google Patents, 1975.
34. A. S. Ramos, S. P. Taguchi, E. C. T. Ramos, V. L. Arantes, and S. Riberio, "High energy ball milling of powder B-C mixture," *Materials Science and Engineering A,* 422A 5 (2006).
35. A. W. Weimer, R. P. Roach, C. N. Haney, W. G. Moore, and W. Rafaniello, "Rapid carbothermal reduction of boron oxide in a graphite transport reactor," *AIChE journal,* 37[5] 759-68 (1991).

36. A. Weimer, W. G. Moore, and R. P. Roach, "Method for producing uniform, fine boron-containing ceramic powders." in*,* Vol. US5194234 A. The Dow Chemical Company, United States, 1993.
37. L. Levin, N. Frage, and M. P. Dariel, "A novel approach for the preparation of B4C-based cermets " *International Journal of Refractory Metals and Hard Materials,* 18 5 (2000).
38. B. Y. Yin and L. S. Wang, "Studies on activated sintering of jet milled B4C powders," *Atom. Energy Sci. Tech.,* 37 4 (2003).
39. X. Li, D. Jiang, J. Zhang, Q. Lin, Z. Chen, and Z. Huang, "Densification behavior and related phenomena of spark plasma sintered boron carbide," 40[3] 4359–66 (2014).
40. S. L. Dole, S. Prochazka, and R. H. Doremus, "Microstructural Coarsening During Sintering of Boron Carbide," *Journal of the American Ceramic Society,* 72[6] 958-66 (1989).
41. M. Tokita, "Mechanism of spark plasma sintering,″ pp. 22 in Proceeding of NEDO International Symposium on Functionally Graded Materials. Vol. 21.
42. B. M. Moshtaghioun, F. L. Cumbrera-Hernandez, D. Gomez-Garcia, S. de Bernardi-Martin, A. Dominguez-Rodriguez, A. Monshi, and M. H. Abbasi, "Effect of spark plasma sintering parameters on microstructure and room-temperature hardness and toughness of fine-grained boron carbide (B4C)," *Journal of the European Ceramic Society,* 33[2] 361–69 (2013).
43. S. Hayun, S. Kalabukhov, V. Ezersky, M. P. Dariel, and N. Frage, "Microstructural characterization of spark plasma sintered boron carbide ceramics," *Ceramics International,* 36[2] 451-57 (2010).
44. A. Lipp, "Boron Carbide: Production, Properties, Application," pp. 47. in. Elektroschmelzwerk Kempten GmbH, Munich, 1966.
45. B. M. Moshtaghioun, F. L. Cumbrera, A. L. Ortiz, M. Castillo-Rodríguez, and D. Gómez-García, "Additive-free superhard B4C with ultrafine-grained dense microstructures," *Journal of the European Ceramic Society,* 34[3] 841-48 (2014).
46. H. Lee and R. F. Speyer, "Hardness and fracture toughness of pressureless-sintered boron carbide (B 4C)," *Journal of the American Ceramic Society,* 85[5] 1291-93 (2002).
47. S. Hayun, V. Paris, M. P. Dariel, N. Frage, and E. Zaretzky, "Static and dynamic mechanical properties of boron carbide processed by spark plasma sintering," *Journal of the European Ceramic Society,* 29[16] 3395-400 (2009).
48. S. R. Murthy, "Elastic properties of boron carbide," *J Mater Sci Lett,* 4[5] 603-05 (1985).
49. K. A. Schwetz, W. Grellner, and A. Lipp, "MECHANICAL PROPERTIES OF HIP TREATED SINTERED BORON CARBIDE,″ pp. 413-26 in Institute of Physics Conference Series.
50. G. De With, "High temperature fracture of boron carbide: experiments and simple theoretical models," *J Mater Sci,* 19[2] 457-66 (1984).
51. L. Farbaniec, J. D. Hogan, and K. T. Ramesh, "Micromechanisms associated with the dynamic compressive failure of hot-pressed boron carbide," *Scripta Materialia,* 106 5 (2015).

52. V. Skorokhod, "Processing, Microstructure, and Mechanical Properties of B4C — TiB2 Particulate Sintered Composites. Part II. Fracture and Mechanical Properties," *Powder Metallurgy and Metal Ceramics,* 39[9-10] 504-13 (2000).
53. C. H. Lee and C. H. Kim, "Pressureless sintering and related reaction phenomena of Al2O3-doped B4C," *J Mater Sci,* 27[23] 6335-40 (1992).
54. H. W. Kim, Y. H. Koh, and H. E. Kim, "Reaction sintering and mechanical properties of B4C with addition of ZrO2," *Journal of Materials Research,* 15[11] 2431-36 (2000).
55. R. W. Rice, "Evaluation and extension of physical property-porosity models based on minimum solid area," *Journal of Materials Science,* 31 17 (1996).
56. K. Sairam, J. K. Sonber, T. S. R. C. Murthy, C. Subramanian, R. K. Fotedar, P. Nanekar, and R. C. Hubli, "Influence of spark plasma sintering parameters on densification and mechanical properties of boron carbide," *International Journal of Refractory Metals and Hard Materials,* 42[0] 185-92 (2014).
57. G. W. Hollenberg and G. Walther, "The Elastic Modulus and Fracture of Boron Carbide,″ pp. 4 in The American Ceramic Society 81st Annual Meeting
58. B. M. Moshtaghioun, F. L. Cumbrera-Hernández, D. Gómez-García, S. de Bernardi-Martín, A. Domínguez-Rodríguez, A. Monshi, and M. H. Abbasi, "Effect of spark plasma sintering parameters on microstructure and room-temperature hardness and toughness of fine-grained boron carbide (B4C)," *Journal of the European Ceramic Society,* 33[2] 361-69 (2013).
59. R. W. Rice, C. C. Wu, and F. Boichelt, "Hardness–Grain-Size Relations in Ceramics," *Journal of the American Ceramic Society,* 77[10] 2539-53 (1994).
60. K. Madhav Reddy, J. J. Guo, Y. Shinoda, T. Fujita, A. Hirata, J. P. Singh, J. W. McCauley, and M. W. Chen, "Enhanced mechanical properties of nanocrystalline boron carbide by nanoporosity and interface phases," *Nature Communications,* 3 (2012).
61. B. M. Moshtaghioun, D. Gomez-Garcia, A. Dominguez-Rodriguez, and R. I. Todd, "Grain size dependence of hardness and fracture toughness in pure near fully-dense boron carbide ceramics," *Journal of the European Ceramic Society,* 36[7] 1829-34 (2016).
62. M. W. Chen, J. W. McCauley, J. C. LaSalvia, and K. J. Hemker, "Microstructural Characterization of Commercial Hot-Pressed Boron Carbide Ceramics," *Journal of the American Ceramics Society,* 88[7] 8 (2005).
63. K. Y. Xie, K. K. Kuwelkar, R. A. Haber, J. C. LaSalvia, and K. J. Hemker, "Microstructural Characterization of a Commercial Hot-Pressed Boron Carbide Armor Plate," *Journal of the American Ceramics Society* (2016).
64. D. P. Dandekar, "Shock Response of Boron Carbide," pp. 47. in. Army Research Labs, 2001.
65. V. Domnich, Y. Gogotsi, M. Trenary, and T. Tanaka, "Nanoindentation and Raman spectroscopy studies of boron carbide single crystals," *Applied Physics Letters,* 81[20] 3783-85 (2002).
66. J. E. Saal, S. Shang, and Z.-K. Liu, "The structural evolution of boron carbide via ab initio calculations," *Applied Physics Letters,* 91[23] 231915 (2007).

67. H. Horii and S. Nemat-Nasser, "Brittle Failure in Compression: Splitting, Faulting and Brittle-Ductile Transition," *Philosophical Transactions of the Royal Society of London,* 319[1549] 44 (1986).
68. P. Lundberg, R. Renström, and B. Lundberg, "Impact of metallic projectiles on ceramic targets: transition between interface defeat and penetration," *International Journal of Impact Engineering,* 24[3] 259-75 (2000).
69. J. C. LaSalvia, E. J. Horwath, E. J. Rapacki, C. J. Shih, and M. A. Meyers, "Microstructural and micromechanical aspects of ceramic/lomg-rod projectile interactions: dwell/penetration transitions," *Explomet 2000* (2000).
70. D. Taylor, J. W. McCauley, and T. W. Wright, "The effects of stiochiometry on the mechanical properties of icosohedral boron carbide under loading," *Journal of Physics: Condensed Matter,* 24 11pp (2012).
71. Q. An, W. A. Goddard III, and T. Cheng, "Atomistic Explanation of Shear-Induced Amorphous Band Formation in Boron Carbide," *Physical Review Letters,* 113 5 (2014).
72. M. Bouchacourt and F. Thevenot, "The correlation between the thermoelectric properties and stoichiometry in the boron carbide phase B4C-B10.5C," *Journal of Materials Science,* 20 11 (1985).
73. S. Roszeitis, B. Feng, H. P. Martin, and A. Michaelis, "Reactive sintering process and thermoelectric properties of boron rich boron carbides," *Journal of the European Ceramic Society,* 34[2] 327-36 (2014).
74. A. C. Fischer-Cripps, "Nanoindentation Testing," pp. 21-37. in Nanoindentation**.** Springer, 2011.
75. W. C. Oliver and G. M. Pharr, "An improved technique for determining hardness and elastic modulus using load and displacement sensing indentation experiments " *J. Mater. Res.,* 7[6] 20 (1992).
76. F. Ouchterlony, "Stress-intensity factors for the expansion loaded star crack," *Engg. Fract. Mech.,* 8 2 (1976).
77. J. S. Reed, "Principles of Ceramics Processing,″ pp. 655 2nd ed. Wiley, (1995).
78. R. Haber, V. Domnich, and D. Maiorano, "XRD and Raman spectroscopy analysis of boron carbides with variable stoichiometries." in. Rutgers Universtiy, 2010.
79. H. Werheit, A. Leithe-Jasper, T. Tanaka, H. W. Rotter, and K. A. Schwetz, "Some properties of single-crystal boron carbide," *Journal of Solid State Chemistry,* 177[2] 575-79 (2004).